NONCOLLECTIVE X-RAY THOMSON SCATTERING DIAGNOSTIC DEVELOPMENT BASED ON A TITANIUM HYBRID X-PINCH X-RAY SOURCE

A Dissertation

Presented to the Faculty of the Graduate School

of Cornell University

in Partial Fulfillment of the Requirements for the Degree of

Doctor of Philosophy

by

Cad Lewis Hoyt

May 2015

NONCOLLECTIVE X-RAY THOMSON SCATTERING DIAGNOSTIC DEVELOPMENT BASED ON A TITANIUM HYBRID X-PINCH X-RAY SOURCE

Cad Lewis Hoyt, Ph.D.

Cornell University 2015

X-ray Thomson scattering (XRTS) is the combination of elastic Raleigh scattering and inelastic Compton scattering observed from high density systems using energetic probe energies at the keV x-ray level. Thermal x-ray probes have historically been created by delivering $10^{14} - 10^{16}$ W/cm^2 to a mid-Z metal foil such as titanium using kilojoule-class lasers. An XRTS probe source must provide adequate photon numbers within a finite bandwidth in order to resolve the elastic and inelastic scattering features. This thesis argues that the 4.75 keV He_α spectral feature from a titanium hybrid x-pinch x-ray source driven in a pulsed power circuit can satisfy these photon and bandwidth requirements and function as an XRTS probe source. The arguments are supported through x-ray diode and image plate photometric analysis for the titanium He_α feature. As a proof of principle, scattering signals from cold, static materials have been collected using the hybrid x-pinch as the probe source.

Two different experimental scattering arrangements were developed to collect the weak scattered signals from room temperature targets. The hybrid x-pinch was driven in the main current path of the Cornell Beam Research Accelerator (COBRA) 1 MA pulsed power driver for both of these arrangements. The first setup, Focused XRTS (FXRTS), used a spherically-bent germanium x-ray optic to focus the probe photons collected from a titanium hybrid x-pinch

approximately 82 *cm* away, and focused them onto a 20 μm thick aluminum foil scattering target. The FXRTS setup allowed the entire scattering experiment to be spatially removed from the actual source location, thus lowering background signals on the detectors. For the second scattering setup, Direct XRTS (DXRTS), a new spectrometer was designed and built to function inside the main COBRA vacuum chamber. The scattering setup functioned in a more traditional sense by having the scattering target, 125 μm thick graphite, placed approximately 20 *mm* away from the x-pinch x-ray source. Protection of the optics and background noise shielding for the detectors were design challenges in the spectrometer.

For both experimental arrangements, the backscattered radiation was collected using high-efficiency highly annealed pyrolytic graphite (HAPG) optics and focused onto Fuji Biological Analysis Systems - Tritium type (BAS-TR) image plate detectors. The noncollective FXRTS results from aluminum show the importance of the ion-ion correlation factor within the total dynamic structure factor and its strong dependence on scattering angle. The FXRTS results were fit with theoretical scattering spectrums created using an XRTS subroutine included in the SPECT3D spectral code suite. Unfortunately, the noncollective DXRTS results from graphite were mixed with line and continuum radiation from other sources that made detailed analysis impossible.

BIOGRAPHICAL SKETCH

Cad Lewis Hoyt was born in Madisonville, TX on December 3, 1982, to Lewis and Cathy Hoyt. He has one younger sister, Ashley, and a nephew, Brendan, Ashley's son. As a young whippersnapper, Cad learned from his dad how to fuse seemingly random pieces of metal together into functional shapes using low-voltage high-current sources. The idea of melting metals with simple electrical circuits may have influenced Cad...

Cad graduated from Centerville High School in December of 2000, five months before his classmates, because he was tired of pointless "book learnin". He enlisted in the Marine Corps and arrived at the yellow footprints at Marine Corps Recruit Depot, San Diego, CA on January 22, 2001. The next four years, which included stress, food deprivation, sleep deprivation, combat patrols, nicotine addiction, fist fights, liberty briefs, safety briefs, pointless deaths, uniform inspections, sweating, bleeding, blisters, rifle qualifications, swim qualifications, weapons training, indoctrinations, inoculations, hazing, dirty jokes, ungodly amounts of alcohol, more pointless deaths, boredom, terror, laughter, boot polish, sea sickness, malaria pills...etc, all caused Cad to reconsider his previous appraisal of "book learnin".

After being Honorably Discharged from the Marine Corps at the rank of Sergeant, Cad enrolled at Sam Houston State University in Huntsville, TX and began studying physics and mathematics with a before unseen fervor. It was at this time that Cad met Caroline Marie Everett, a psychology major who claimed to need help understanding physics. Cad surmised that in all likelihood, she just wanted to spend more time with Cad.

After graduating *magna cum laude* in physics, Cad decided that going to graduate school might be fun, so he applied to various graduate programs.

Cad was somehow accepted to the Electrical and Computer Engineering department at Cornell University where he met Dave Hammer who worked in pulsed power and plasma physics. After touring the lab and seeing all the wonderful "toys" used in these fields, Cad eagerly accepted Dave's invitation to join the lab.

Caroline and Cad married during his graduate studies at Cornell. They plan on heading further south once all this nonsense is done.

For Caroline...thank you for loving me and putting up with all of my horseshit.

ACKNOWLEDGEMENTS

> "I am unfortunate in a want of mathematical knowledge and the power of entering with facility into abstract reasoning. I am obliged to feel my way by facts closely placed together."
>
> - Michael Faraday in a letter to André Marie Ampère, 1822

The military taught me that I can learn just as much from a "bad" teacher as a "good" one. I have met and learned from many people here at Cornell, both in the lab and out. So thank you all, whatever category you're in...

TABLE OF CONTENTS

LIST OF TABLES

LIST OF FIGURES

CHAPTER 1

INTRODUCTION

1.1 X-ray Thomson Scattering History and Development

The study of dense matter by x-ray Thomson scattering (XRTS) schemes was first suggested by Landen *et al.* regarding intertial confinement fusion (ICF) experiments [1]. It was argued that this diagnostic, like optical Thomson scattering schemes on low density plasmas, could provide measurements of temperature, density, and ionization state in high density systems, inaccessible to lower frequency probes, by spectrally resolving the elastic (Rayleigh) scattering from the inelastic scattering that would simultaneously be Compton and Doppler shifted. The primary method suggested to create the intense source of probe x-rays were kilojoule-class laser facilities, which would be capable of converting the laser energy into x-ray photons by laser-plasma interaction using high-Z foils such as vanadium.

Glenzer *et al.* [2] followed this theoretical work with the first experimental scattering results from solid density beryllium using the 30 kJ Omega laser facility [3]. In this work, the Be target was heated via absorption of laser-produced Rh L-shell emission. A secondary laser-plasma source was used to provide the 4.75 keV He_α line radiation from a Ti foil which served as the scattering probe. A schematic diagram of the experiment is shown in Fig. 1.1.

The use of soft x-ray free electron lasers (FELs) in XRTS experiments was initially explored by Riley *et al.* [4]. Proof-of-principle work using VUV FEL radiation to probe dense plasmas was presented by Höll *et al.* [5] using the

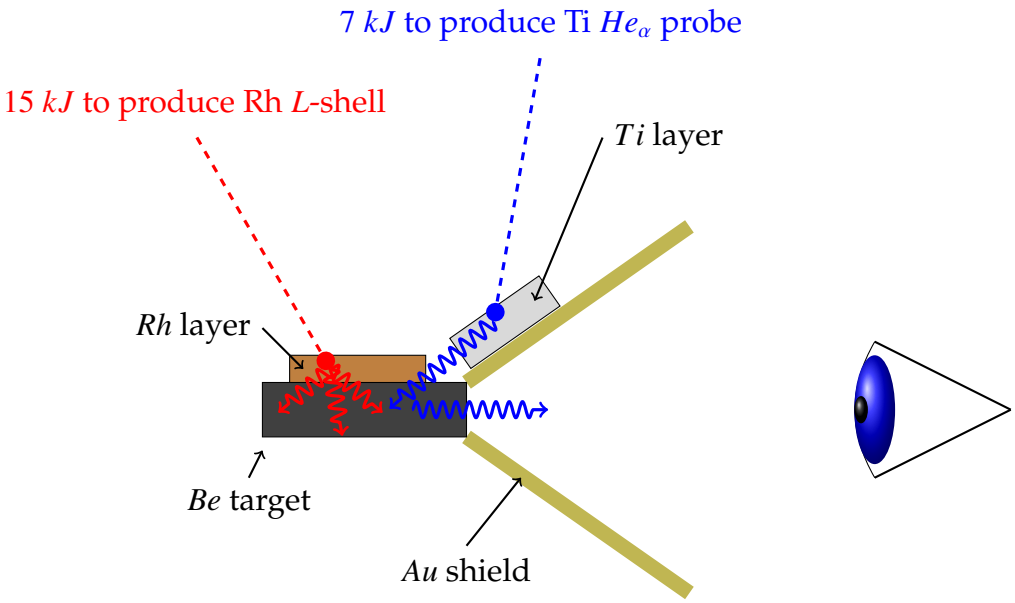

Figure 1.1: Schematic of the first successful XRTS experiment performed on the Omega laser facility. A thin rhodium layer was heated by 30 beams in order to produce *L*-shell radiation that would penetrate and heat the beryllium cylinder target. A titanium layer then provided the He_α probe photons created using 15 beams, 1 *ns* later. The gold foil shield restricted the view to only the scattered photons from the heated beryllium target.

FLASH facility in Hamburg [6]. Using the same facility, Faustlin *et al.* were able to observe femtosecond-scale electron dynamics in liquid hydrogen using XRTS techniques [7].

To date, the majority of experimental scattering results have come from facilities with access to kilojoule-class lasers, which are capable of producing x-ray sources with the required brightness [8]. Since the initial results of Glenzer, XRTS experiments have been performed primarily for equation of state (EOS) studies, as diagnostic access to solid density materials under extreme compression (shock compression) is limited and the experimental data can be used to resolve fundamental EOS questions relevant to ICF and the fields of materials science and planetary science [9, 10, 11].

In addition to the information on temperature, density and ionization state, XRTS experiments can also shed light on other intrinsic properties such as conductivity via plasmon dispersion and dampening [12]. These conductivity results can be used to develop new models and validate existing plasma physics models for studying ICF conditions.

1.2 XRTS Limiting Factors

The primary limiting factor for any XRTS experiment is the probe source intensity. The fraction of scattered photons from a scattering volume of thickness l and density n_e is given by

$$N_{frac} = n_e \, l \, \sigma_t \tag{1.1}$$

where σ_t is the Thomson scattering cross section ($\approx 0.66 \times 10^{-24}\ cm^2$). Approximating σ_t as $\sim 10^{-24}\ cm^2$ and assuming scattering from a solid density Al target ($n_e \sim 10^{24}\ cm^{-3}$) of thickness $\sim 10^{-3}\ cm$ yields a scattered fraction of 10^{-3} into $4\pi\ sr$ or about 10^{-4} scattered photons per steradian. Further assuming an optimistic finite collection solid angle of order $10^{-2}\ sr$ ultimately yields a fraction at the detector of 10^{-6}. Simply put, whatever intensity of photons that can be brought to bear onto the target will be reduced in intensity by a factor of 1 million at the detector. If background noise constrained the experiment such that no fewer than 10^6 photons could be detected, the required total fluence into the scattering target would have to be $\geq 10^{12}$ photons. For an x-ray source, this is no small feat as attested by the large laser facilities currently required to perform an XRTS experiment.

The second hurdle to overcome is bandwidth, usually written as $\Delta E/E$ or

$\Delta\lambda/\lambda$. The Compton shifted *inelastic* feature must be resolved from the unshifted *elastic* feature in the probe spectrum in order to retrieve any useful diagnostic information beyond the mere presence of the target. The magnitude of the Compton shift is a function of probe energy and scattering angle. The noncollective scattering regime, in which scattering from individual electrons is uncorrelated, is characterized by large probe energies and large backscattering angles, producing a relatively large Compton shift. Working in this regime, previous experiments have found success when $\Delta E/E \lessapprox 0.01$. Thermal sources produced by laser-foil interactions are capable of producing lines that meet this requirement [8].

The collective scattering regime usually deals with weaker probe energies and forward scattering ($< 90°$) setups. The shifts in energy are also due to energy transfer to and from plasmons (collective modes). This results in smaller energy shifts and therefore a smaller bandwidth required to resolve at $\Delta E/E \lessapprox 0.002$ [9].

1.3 The X-pinch: A pulsed power x-ray source

This thesis is based on using a well-established Laboratory of Plasma Physics (LPS) workhorse to function as the probe source in a noncollective XRTS experiment: the x-pinch. The dynamics and photometric characteristics of the hybrid x-pinch, a variant of the orginal 2-wire x-pinch, are explored in greater detail in Sec. 2.2. Here, we wish to show that the previously established XRTS source requirements can be met by the x-pinch using simple arguments based on previous research for the bandwidth requirement, and energy analysis performed

on electrical diagnostics for the intensity requirement. These goals will require some background on pulsed power and the associated diagnostics.

The bandwidth requirement for a noncollective XRTS source is easily met, as the x-pinch "hotspot" is a thermal source which does produce copious amounts of line radiation [13]. Temperatures and densities reported for laser-produced thermal plasma sources are comparable to the observed temperatures and densities found in x-pinch hotspots [14]. All scattering results collected and presented in this thesis are based on the thermally-produced Ti He_α spectral feature, shown in Fig. 1.2. This feature consists of a resonance line centered near 4750 eV, an intercombination line centered near 4727 eV, and trailing Li-like satellites resulting in a width of $\Delta E \approx 50\ eV$ for an overall bandwidth of $\Delta E/E \approx 0.01$. This line is attractive to use as there exists a large amount of laser-produced x-ray source XRTS experimental data which has established the line as a viable probe [15, 16, 17, 18].

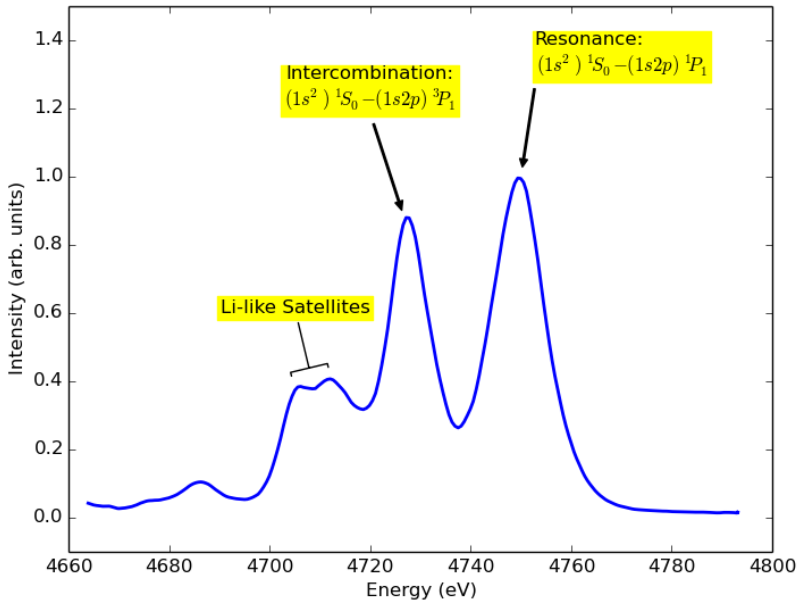

Figure 1.2: The Ti He_α spectrum from an x-pinch.

To ensure the intensity requirement is met, the number of photons produced within the bandwidth of interest must be measured. The next section details such a measurement.

1.4 Pulsed Power Driven X-ray Source Efficiency

The requirement for large kilojoule-class laser facilities in XRTS experiments is largely due to the relatively weak coupling efficiencies involved in the conversion of laser light to x-ray probe photons. Laser-produced plasma x-ray source characterization experiments by Matthews *et al.* on Ti disks using a range of laser intensities and incident wavelengths estimated $\sim 10^{12}$ 4.75 keV photons per Joule of incident laser energy, roughly corresponding to .08% conversion efficiency. Experiments performed on the 2 kJ Z-Beamlet laser at Sandia have shown a $\sim 0.1\%$ conversion efficiency from 527 nm light to 4.75 keV Ti He_α x-rays [19].

The conversion efficiency of stored electrical energy to x-ray output from imploding wire array loads driven by pulsed power machines such as the **CO**rnell **B**eam **R**esearch **A**ccelerator (COBRA) has been reported to be between $10-15\%$ [20], though these yields were measured with a bolometer which has a wide bandwidth response. In order to properly compare to laser-foil coupling studies, it is beneficial to estimate the conversion efficiency of the *coupled* electrical energy into x-ray output for a given bandwidth for a hybrid x-pinch load on COBRA. Before this analysis is presented, a brief introduction to pulsed power circuits and a description of the diagnostics used in the analysis is in order. For a more complete introduction to pulsed power the reader is referred to *J. C.*

Martin on Pulsed Power [21].

1.4.1 Pulsed Power

Pulsed power is the collective term applied to circuits which function around the act of storing energy over a long period (low power) then rapidly discharging over a relatively short period (high power). The research performed in the Laboratory of Plasma Studies (LPS) is based solely upon plasmas created using pulsed power techniques. Pulsed power machine complexity can range from the fairly simple, such as parallel capacitive discharge circuits, to quite complex orchestrations involving multi-stage Marx banks, intermediate storage capacitors (ISC), laser-triggered switches and pulse forming lines (PFL). COBRA is an example of the latter, capable of delivering $1 - 1.2\ MA$ in about $100\ ns$ in short pulse mode or in about $200\ ns$ in long pulse mode [22]. The X-Pinch (XP) machine is another pulsed power driver capable of delivering $450-500\ kA$ in a $50\ ns$ short pulse or a $100\ ns$ long pulse [23]. Computer-aided design (CAD) models of these two drivers are shown in Fig. 1.3.

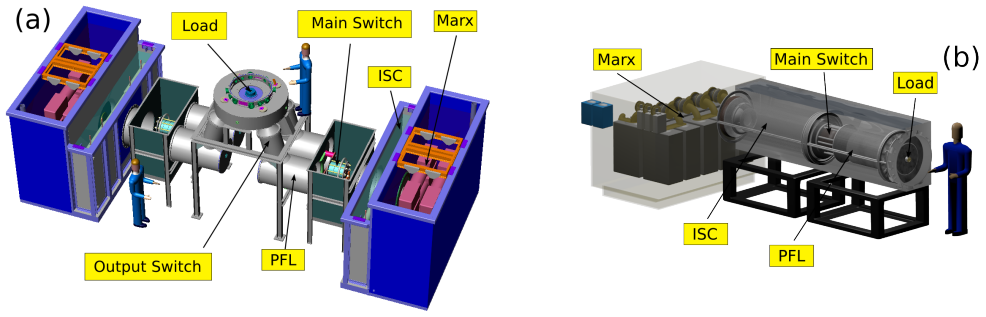

Figure 1.3: Pulsed power drivers used in LPS: COBRA (a) and XP (b).

The simplest example of a pulsed power circuit is the capacitive discharge circuit shown in Fig. 1.4. Switch S_1 is first closed to allow the voltage source V_0

to charge the capacitor C_1 through a resistance R_1. This would be the low power phase of the circuit operation typically occuring over several seconds. Once fully charged, S_1 is opened and S_2 is closed allowing C_1 to rapidly discharge into Z_{load}. This is the high power phase of circuit operation with discharge time scales ranging from 10^{-9} seconds to 10^{-6} seconds, depending on load impedance, the self-inductance of S_1, and the self-inductance and equivalent series resistance (ESR) of C_1. With these values known, the high power portion of the circuit can be accurately modeled as an RLC series circuit [24]. The maximum voltage this type of circuit can deliver is typically limited to $\lesssim 100\ kV$ due to the dielectric strength of the capacitor.

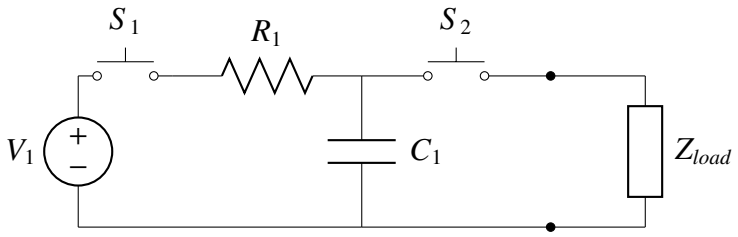

Figure 1.4: A simple capacitive discharge circuit.

The voltage limitations of a single capacitor discharge circuit can be overcome with the use of a Marx bank configuration. A Marx bank circuit consists of N capacitors charged in parallel to a voltage V_0 and then discharged in series, resulting in an output voltage of $\approx NV_0$. A simple 3-stage Marx bank circuit is depicted in Fig. 1.5. Initially, all the switches are open allowing the capacitors to charge in parallel to V_0. The first stage switch S_1 is typically triggered with a high voltage pulse from a separate generator. When S_1 is fully closed, a potential of $\approx 2V_0$ will appear across S_2, causing it to break down. This cascading process (referred to as "erection") will continue down the line to each of the N stages until all of the switches are closed, resulting in a final voltage of $\approx NV_0$ at the output.

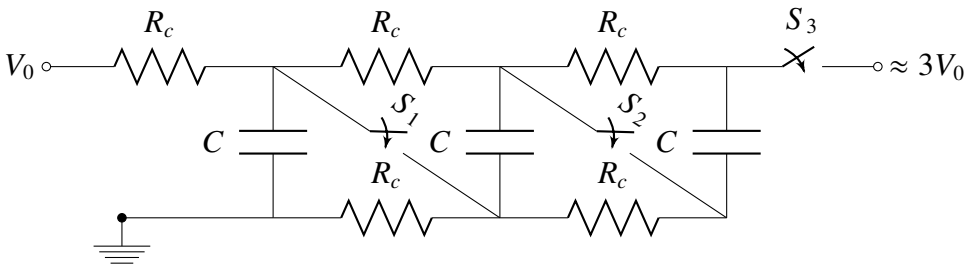

Figure 1.5: 3-stage Marx bank circuit.

A fully erect Marx bank is highly inductive (high impedance), leading to low current rise times (relatively low output power). In practice, most Marx banks are coupled to intermediate storage capacitors which feed into pulse forming lines, which can have much lower output impedances resulting in higher power delivered to a given load. A simplified equivalent circuit is shown in Fig. 1.6 which is a closer representation to the pulsed power drivers currently used in the research done by LPS.

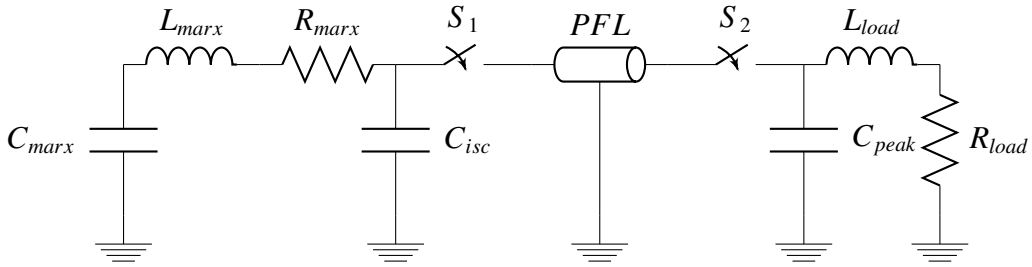

Figure 1.6: Equivalent circuit example of a Marx-based pulsed power driver.

The Marx banks on COBRA ($32 \times 1.3\ \mu F$ capacitors) are typically charged to 70 kV, resulting in approximately 100 kJ of stored energy. During a shot, much of this energy is lost through the switches and through the deionized water dielectric of the ISCs and the PFLs on the way to the load region. Consequently, only a fraction of this stored energy is actually delivered to a given load. This energy can be estimated with the load voltage V and load current I signals re-

covered using the voltage and current diagnostics on COBRA.

1.4.2 Current and Voltage Diagnostics

Large currents at high voltages are most easily measured through the use of inductive sensors, such as Rogowski coils and $\dot{B}$-probes (pronounced "B-dot") [25]. Inductive sensors function in accordance with Faraday's Law [26]:

$$\oint_c \mathbf{E} \cdot \mathbf{dl} = -\frac{d}{dt} \int_s \mathbf{B} \cdot \mathbf{da} \tag{1.2}$$

When magnetic field penetrates a closed conducting loop, a voltage is induced on the loop that is proportional to the time rate of change of flux penetrating the loop.

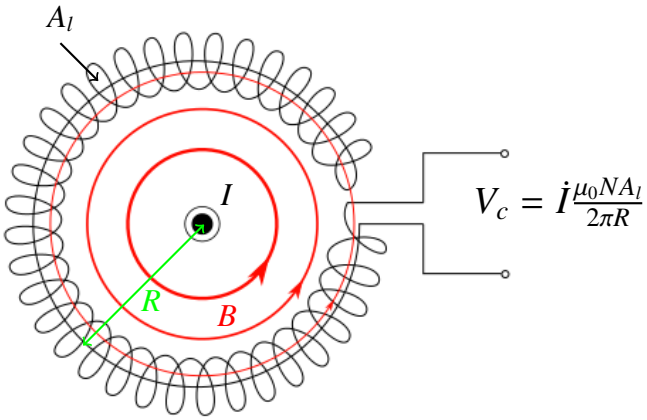

Figure 1.7: Rogowski coil.

A Rogowski coil (Fig. 1.7) is a series of N loops of area A_l wound around a torus of major radius R which completely encircles a current I. For a non-integrating Rogowski coil, the voltage induced in the coil V_c is proportional to $\dot{I}$

and must be integrated to obtain the load current:

$$I = \int \dot{I} dt = \frac{2\pi R}{\mu_0 N A} \int V_c dt \tag{1.3}$$

A non-integrating coil is currently employed on COBRA.

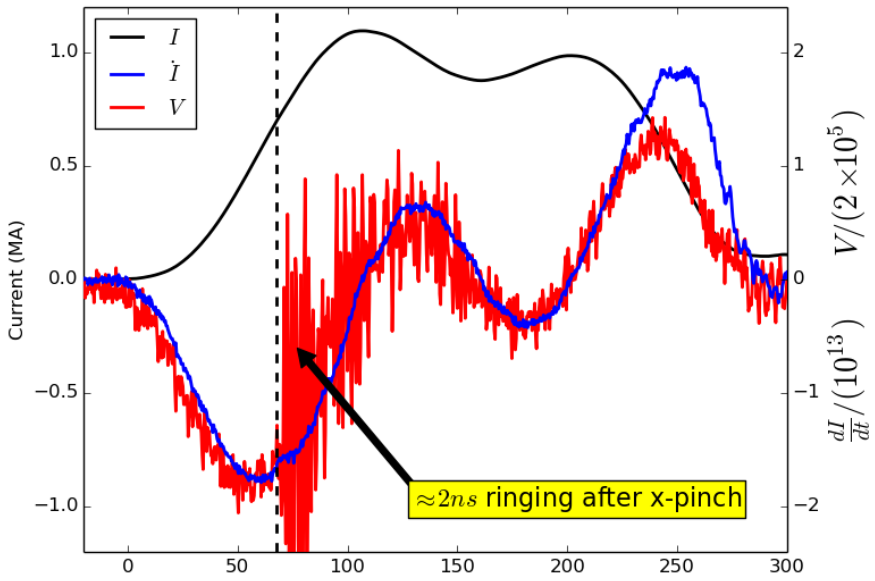

Figure 1.8: Current ($\dot{I}$ in blue, I in black) and voltage (red) signals from a COBRA shot with an x-pinch load. The vertical dashed black line represents the time of peak x-pinch emission.

Voltages at the load are determined with an inductive voltage monitor on COBRA. The inductive voltage monitor is simply a long, thin conducting wire of known inductance L_w that connects the base of the cathode with ground. A small fraction of the time-varying load current flows down this conductor which creates a time-varying magnetic field that is measured at a radial distance R with a $\dot{B}$-probe. The $\dot{B}$-probe is a simple conducting loop of area A that lies normal to the direction of the magnetic field being measured. In other words, an $N = 1$ non-integrating Rogowski coil. The inductive voltage established in the probe, V_p, is related to the actual load voltage (ignoring resistive loss in the conductor)

viz.

$$V = L_w \dot{I} = L_w \frac{2\pi R}{\mu_0 A} V_p \tag{1.4}$$

Examples of the current and voltage monitor signals are presented in Fig. 1.8. X-pinch loads on COBRA tend to induce a characteristic $\approx 2\,ns$ ringing down the voltage monitor line at pinch time due to the large and rapid voltage changes created by the collapse of the pinch. This limits the accuracy of any voltage based signal analysis for times after the first x-ray burst. Therefore the energy analysis will only be attempted for times leading up to the initial x-ray burst and multiple following bursts, if they exist, will not be included.

1.4.3 Photoconducting Diode X-ray Diagnostic

The x-ray emission from a COBRA experiment is typically monitored with diamond photoconducting diodes (PCD) [27]. Ionizing radiation from the x-pinch liberates electrons within the diamond insulator ($3mm \times 1mm \times 0.5mm$), which is biased at $\approx 300\ V$. The current that subsquently flows is proportional to the incident photon power and the applied bias voltage. The PCD voltage signals are recorded by a $1GHz$ Tektronix digital oscilloscope. Filters of various Z and thickness are often used to limit the incident bandwidth and the response of the PCD.

The PCDs currently in use did have experimentally determined responses, but unfortunately, those individual responses have been mixed and/or lost over time. However, all of the PCDs in question have responses of order $10^{-4}\ A/W$.

Therefore, it is sufficient for the x-pinch efficiency analysis to assume this PCD response. This response translates to about 200 W/V when measured across a 50 Ω impedance.

1.4.4 Coupled Electrical Energy Estimation Technique

The measured voltage term in Eqn. 1.4 is comprised of three source terms particular to the load:

$$V = IR + I\dot{L} + \dot{I}L. \tag{1.5}$$

The total inductance L is actually $L_{conv} + L_{load}$ where L_{conv} is due to the physical attachment location of the voltage probe which "sees" about 10 nH of convolute feed. L_{load} is estimated (for a hybrid x-pinch) to be about 11 nH giving a total value of 21 nH for L. Equation 1.5 can be further simplified to two terms by considering the load impedance as $Z = R + \dot{L}$:

$$V = IZ + \dot{I}L \tag{1.6}$$

The electrical power delivered to the load is determined by mutliplying Eqn. 1.6 with the load current:

$$P = I\,V = I^2Z + I\dot{I}L \tag{1.7}$$

The first term in Eqn. 1.7 represents the rate of energy deposition into the load. This is energy that couples to the load either through joule heating, or through the work done by the azimuthal magnetic field as it compresses the plasma, *i.e.* $I^2\ \dot{L}$. The kinetic energy gained by the imploding plasma eventually thermalizes through collision processes as the implosion proceeds [28] (see Sec. 2.1). The second term in Eqn. 1.7 is the rate of energy storage in the magnetic field

and does not directly contribute to the conversion of electrical energy to x-ray energy.

The energy that is directly coupled to the load, E', can be obtained by rearranging Eqn. 1.7 and then integrating up to the time of interest, which in this case would be the time of the x-ray burst from an x-pinch

$$E' = \int_0^t I^2 Z \, dt = \int_0^t (IV - I\dot{I}L) \, dt \tag{1.8}$$

The total electrical energy delivered to the load, E, can similarly be found by directly integrating Eqn. 1.7 up to the same time point.

1.4.5 X-ray Output Energy Estimation Technique

The filtered PCD signal can be used, along with some assumptions about the spectral characteristics of the Ti x-pinch burst, to make an estimate of x-ray energy output. The spectral characteristic assumptions are made with the aid of *FLYCHK*, a generalized population kinetics and spectral model code suite [29]. Experimentally determined plasma parameters for a Ti x-pinch ($T_e \approx 1.2\ keV$, $n_e \approx 10^{23}\ cm^{-3}$, see Ref. [30]) are used in the collisional-radiative (non-LTE) model to calculate a spectral output. The FLYCHK results are shown in Fig. 1.9.

The PCD used for this analysis was filtered with $50\mu m$ thick Ti. The transmission curve for this thickness of Ti is shown as the green trace in Fig. 1.9. The majority of the strongest emission occurs inside the Ti transmission window with the dominant feature being the Ti He_α line consisting of the resonance, intercombination and Li-like satellite lines (see Fig. 1.2). The addition of the filter ensures that the majority of the signal recorded by the PCD is due to the Ti probe

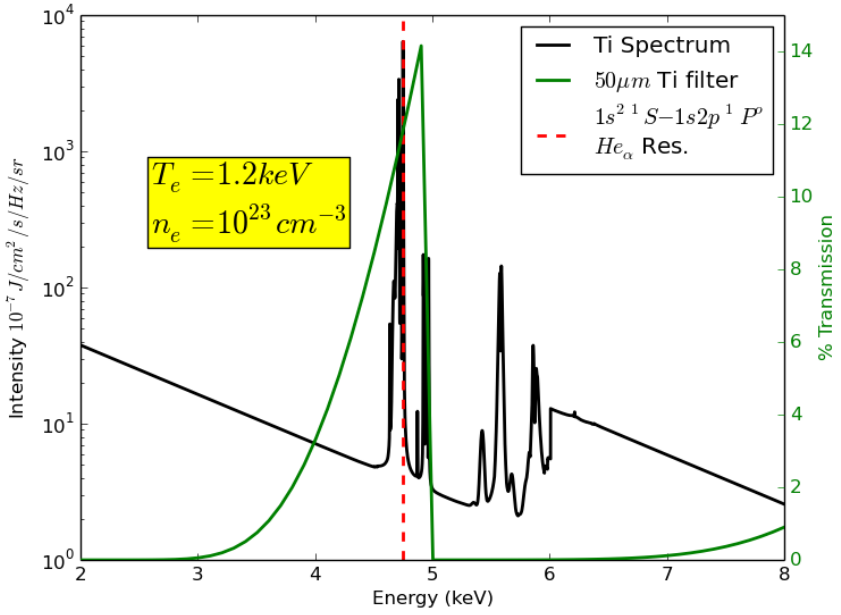

Figure 1.9: FLYCHK-produced plot of Ti emission spectra (black) with overlaid (green) $50\mu m$ Ti filter transmission. The location of the Ti He_α resonance transition at 4.75 keV is denoted with the dashed red line.

feature of interest, lending this energy estimation technique more accuracy. The thickness of the Ti filter used limits the overall transmission through to the PCD to about 10%.

With reasonable assurance that the PCD is primarily responding to the bandwidth of interest, the PCD response ($\eta_{pcd} \approx 200\ W/V$) can now be multiplied by the voltage signal (V_{pcd}) and then integrated over the FWHM of the x-pinch burst, taking into account the fractional solid angle that the PCD subtends (Ω) and filter attenuation (κ), to get an energy estimate. The x-pinch energy into 4π is given by

$$E_\gamma = \frac{\Omega}{\kappa}\int_{fwhm} \eta_{pcd} V_{pcd}\, dt \approx \frac{\Omega}{\kappa}\,\eta_{pcd}\, V_{pcd}^{max}\,\Delta\tau_x \tag{1.9}$$

where the peak pcd voltage V_{pcd}^{max} is used, and an average Ti x-pinch burst duration $\Delta\tau_x$ determined *a posteriori* (see Ref. [31]) is substituted for simplification.

Since E_γ has units of joules and the photons from the Ti He_α feature are order 10^3 eV in energy, a simple order-of-magnitude photon count can be made by multiplying by a factor of 10^{16}:

$$N \sim E_\gamma \times 10^{16} \tag{1.10}$$

1.4.6 Conversion Efficiency Analysis and Photometrics

With the required analysis tools established and in place, a conversion efficiency based on the ratio of the emitted x-ray energy to the coupled electrical energy can be calculated:

$$\eta = \frac{E_\gamma}{E'} \tag{1.11}$$

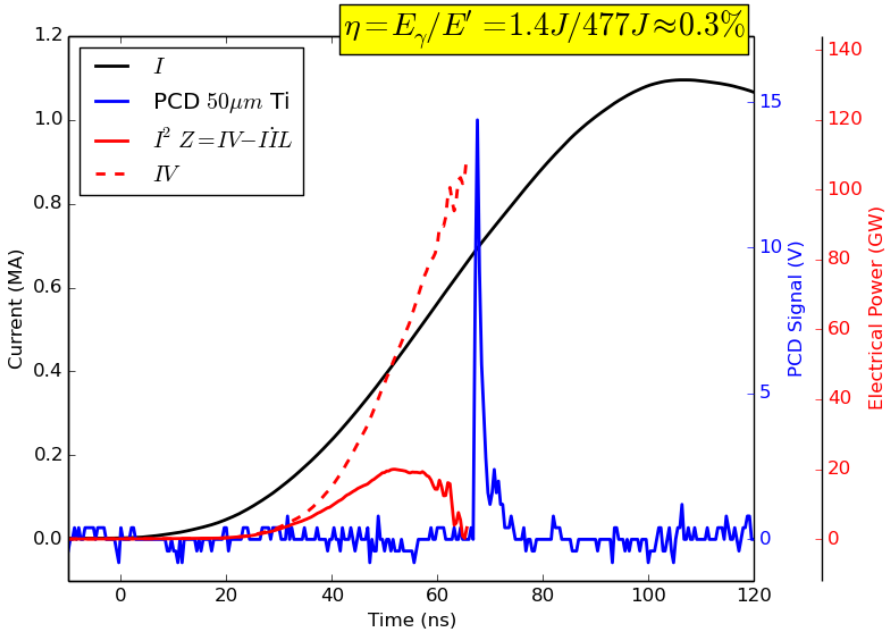

Figure 1.10: The total electrical power delivered, IV (red dashed trace) and the coupled electrical power, I^2Z (red trace), for a Ti hybrid x-pinch driven by the full COBRA current pulse (black trace) and the measured PCD signal voltage (blue trace) filtered with $50\mu m$ of Ti.

Shown in Fig. 1.10 are the results of the previously described analysis applied to a COBRA shot with a Ti hybrid x-pinch as the main load. The total electrical power delivered to the load (red dashed trace) peaks around 110 GW which integrates to approximately 1.5 kJ of total delivered energy. The coupled power, $I^2Z = IV - I\dot{I}L$ (red solid trace) peaks at approximately 20 GW which integrates to about 477 J up to the time of the x-pinch burst.

The PCD voltage (blue trace) peaks near $14V$ which converts to about 2.8 kW of radiated power. Using values of $\Delta\tau_x = 0.5\ ns$, $\Omega = 10^5$, and $\kappa = 0.1$ in Eqn. 1.9 yields approximately 1.4 J of radiated energy or roughly 10^{16} Ti He_α photons into $4\pi\ sr$

These energy values indicate a conversion efficiency of $\approx 0.3\%$ or about 10^{13} photons per joule of coupled energy. In this particular shots total energy account, of the 100 kJ of stored energy in the capacitor banks, only about 1.5% actually made it to the load in the time of interest, with the rest being lost to "overhead" in the pulsed power network. Of this fraction, only about about 30% coupled to the load through joule heating or implosion kinetic energy through $I^2\dot{L}$. Only about 0.3% of this coupled fraction was actually converted to x-ray output that was transmitted through the filter window, of which the majority was assumed to be from the He_α feature.

This analysis scheme was performed on a shot series of 5 , $140\mu m$ diameter Ti hybrid x-pinch loads on COBRA. Precision in the setup was given extra care in order to be as reproducible as possible from one shot to the next. The results of this study are presented in Table 1.1. The first column holds the shot number, the second column holds the total electrical energy E, the third holds the coupled electrical energy E', the fourth holds the emitted x-ray energy E_γ, the fifth holds

the conversion ratio η and the sixth and final column holds the estimated photon count N.

Shot #	E	E'	E_γ	η	N
3300	1887	648	2.4	0.4	2.4×10^{16}
3301	1299	424	3.9	0.9	3.9×10^{16}
3303	1054	413	3.3	0.8	3.3×10^{16}
3305	1585	477	1.4	0.3	1.4×10^{16}
3306	2055	534	1.7	0.3	1.7×10^{16}
Average	1576	499	2.5	0.5	2.5×10^{16}

Table 1.1: Ti hybrid x-pinch efficiency on COBRA. All energies have units of joules, η is a percentage and N is photons emitted into 4π.

Despite the attention to detail in the initial setup of each of these hybrid x-pinch experiments, large variation exists in all categories over this small sample size. There are numerous contributing factors from both the pulsed power machine performance side and the actual x-pinch dynamics side which are not discussed in this thesis further. All x-pinches are inherently random in nature, and the hybrid x-pinch is no exception, which means seemingly small experimental variations can lead to large variations in output. An example of an unknown variable is the quality of the electrical contact between the hybrid electrode and the Ti fine wire, which is completely ignored in most hybrid x-pinch setups.

Nonetheless, it can be taken from this rudimentary analysis that a hybrid x-pinch on COBRA can potentially be used as a Ti He_α probe source in an XRTS experiment, with coupling efficiencies and corresponding photon counts that are similar to those experiments reported earlier that have led to successful scattering experiments. A more detailed method of photometric estimation using image plates is also presented in Sec. 2.6 which gives good agreement with the previous analysis.

CHAPTER 2

THE X-PINCH X-RAY SOURCE

2.1 Z-pinch Introduction

Imploding wire array z-pinches on pulsed-power drivers are currently the brightest x-ray sources in the world, able to convert about 10 – 15% of the stored electrical energy into soft x-rays between 1 and 10 keV [32, 33, 34, 35]. The typical z-pinch experiment for the purpose of x-ray production usually involves a cylindrical arrangement of fine wires bridging the anode and cathode of a current driver (Fig. 2.1a). As current heats the individual wires, the resistivity increases rapidly leading to a large potential difference across the wires. Eventually, desorbed gas or the vapor of the wire material near the wire surface breaks down and plasma forms, resulting in a warm, high-density liquid-solid core surrounded by a hot, low-density coronal plasma. The global $\mathbf{J} \times \mathbf{B}$ force then pushes ablated coronal plasma (Fig. 2.1b) from the initial wire locations towards the geometric center of the array where it thermalizes and compresses into a radiating column of plasma. This current carrying plasma column (Fig. 2.1c) is susceptible to $m = 0$ and $m = 1$ ("sausage" and "kink") instabilities which occur randomly along its entire length with the former mode being more common [36]. This is a highly simplistic explanation that ignores the very real problems of trailing mass and current in the ablation streams and the effects of magneto-Rayleigh-Taylor (mRT) instability. The most intense x-ray emission originates from so called "hotspots" that form in the necks of these $m = 0$ instabilities [37].

The mechanism thought to be responsible for the creation of the hotspots and the intense x-ray burst is known as radiative collapse. The density-dependent

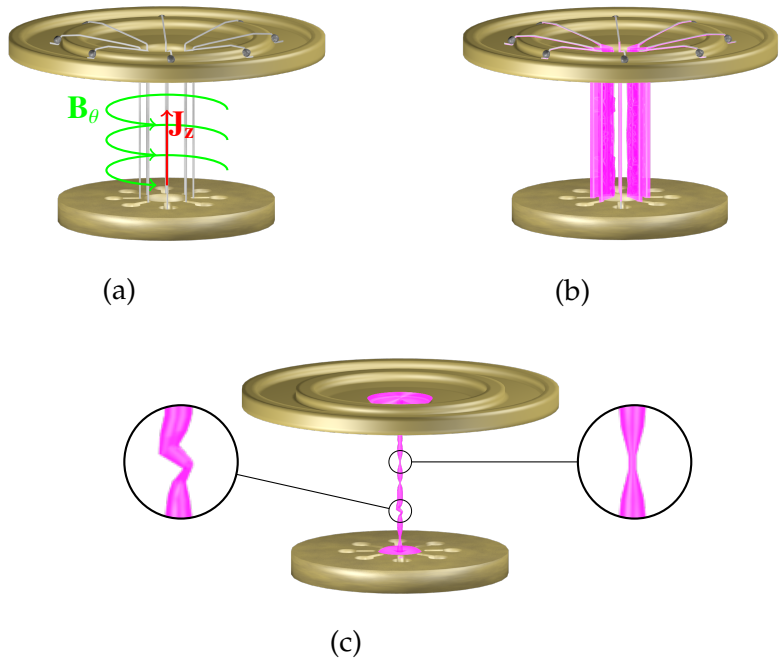

Figure 2.1: (a) Standard wire array example. (b) Ablated wire material is forced to geometric center by $\mathbf{J} \times \mathbf{B}$. (c) Unstable plasma column with $m = 0$ (right) and $m = 1$ (left) instability modes.

rate of radiative cooling in the optically thin plasma neck volume is greater than the ohmic heating rate, which combined with the magnetic field pressure outside allows the neck to further compress resulting in a higher density and consequently higher radiative cooling rate. This feedback process continues rapidly until the plasma density within a very small region ($\sim 1\ \mu m$) becomes optically thick to any $\sim 1\ keV$ radiation trying to escape resulting in energy being increasingly directed into a volume with the only relaxation method to remove it being black body radiation from the increasingly shrinking surface area. At some point and due to an as yet to be determined instability process, the small volume ruptures and explosively disassembles releasing a massive burst of continuum radiation on a picosecond timescale [38]. The immediate region surrounding the hotspot will generally be cooler resulting in copious amounts of line radiation

that can have longer emission lifetimes up to ~ 1 ns. The hotspots are generally about 1 μm in diameter with electron densities $\gtrsim 10^{23}\ cm^{-3}$ and electron temperatures at or above 1 keV [39, 40].

2.2 X-pinch Introduction

As stated previously, the hotspots will form randomly all along the pinch column and collectively within a span of $1 - 50$ ns depending on implosion time and array mass [41, 20, 42]. The random location makes detailed study difficult. The "X"-pinch was introduced to combat this location uncertainty. An x-pinch is easily made by joining an anode and cathode by two parallel fine wires and then twisting the anode or cathode by > 180° (Fig. 2.2).

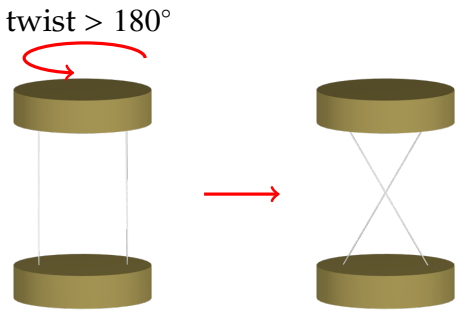

Figure 2.2: An x-pinch is constructed by joining 2 fine wires in parallel across an anode-cathode gap and then twisting > 180°.

The first data on a two-wire x-pinch was published in 1982 by Zakharov et al [43]. The "X" configuration provided a favorable low pressure region above and below the meeting point of the two wires for plasma out-flow. In doing this, the pinch region would be localized to the crossing point of the wires and remove some of the uncertainty in pinch location for the alignment of the diagnostics. Figure 2.3 is a series of radiographs of the pinching process of an x-pinch taken

with the aid of a second x-pinch providing the imaging continuum burst. The left-most image clearly depicts the $\sim 300 - 400\ \mu m$ tall cylindrical pinch column that is only starting to show signs of the $m = 0$ instability mode. The right-most image captures the final moment of the radiative collapse process just before the x-ray burst and rapid disassembly of the plasma column [44].

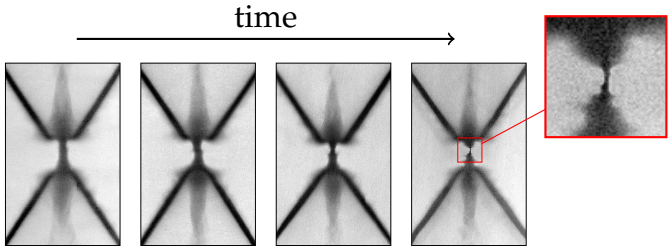

Figure 2.3: A sequence of radiographs depicting the neck formation and pinching of an x-pinch at the crossing point.

In addition to the short, thermal x-ray burst from the hotspot, large inductive voltages that form across the disassembled neck can produce high energy electron beams. An example radiograph of one of these gaps forming approximately 300 ps after the thermal x-ray burst is show in Fig. 2.4. The accelerated electrons collide with the dense plasma on the anode side and produce brehmsstrahlung photons with measured energies ranging from $10 - 60$ keV and durations from $1 - 2$ ns [45].

2.3 X-pinch Applications

2.3.1 Imaging

The rapid and bright x-ray continuum burst from the x-pinch lends itself well to broadband x-ray backlighter imaging of dense plasmas allowing highly ac-

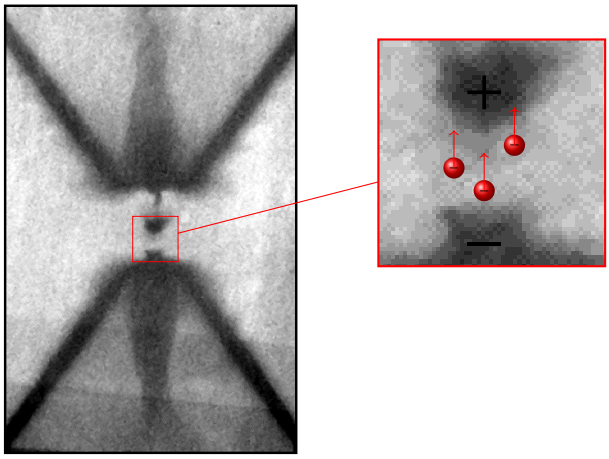

Figure 2.4: Gap formation after the thermal x-ray burst. Hard x-ray brehmsstrahlung photons can be created from the electron beam.

curate measurements of areal density to be made [46, 47, 48]. The technique of x-ray backlighting is based on *absorption contrast imaging*. As a ray moves through a material, its initial intensity is reduced by absorption along the path based on the Beer-Lambert law:

$$I(x) = I_0 e^{-\mu x} \tag{2.1}$$

where I_0 and x are the initial beam intensity and the distance traveled through the material. The variable μ is known as the linear attenuation coefficient and essentially describes how well the material absorbs per unit length.

In addition to broadband backlighting, x-ray monochromators can be used to select a small bandwidth of the transmitted radiation through the imaged object and focus it to a detector. The monochromator can also select the probe bandwidth first and then focus through the imaged object to the detector. This technique is known as monochromatic or quasimonochromatic x-ray backlighting, depending on the experimental details [49, 50].

A third x-pinch backlight imaging technique is known as *phase contrast imag-*

ing which exploits the small variations in the index of refraction, $n = 1 - \delta$, to sharpen the edges of an object through wave front interference. This technique requires the source to have high spatial (or transverse) coherence due to the very small deviations of the indices of refraction from unity, i.e. $\delta << 1$. The micron-scale source size of the hotspot makes this possible [51, 52]. Shown in Fig. 2.5 are comparisons of the absorption contrast and phase contrast imaging techniques applied to a small biological sample.

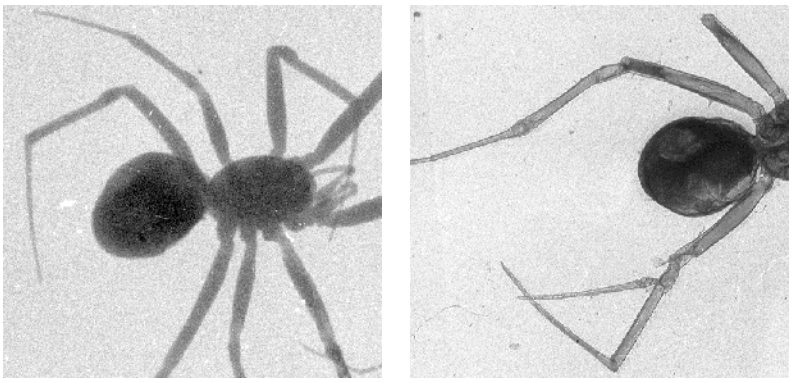

(a) absorption contrast (b) phase contrast

Figure 2.5: (a) Absorption contrast imaging of a spider which relies on mass attenuation of the x-rays through the specimen. (b) Phase contrast imaging of the same spider which relies on wavefront interference revealing sharper details inside the leg joints and abdomen.

2.3.2 X-ray Absorption Spectroscopy

The characteristic uniform broadband burst associated with the Molybdenum x-pinch has also made an excellent diagnostic source for x-ray absorption spectroscopy allowing subnanosecond measurements of density and temperature in warm dense matter experiments [53].

2.4 X-pinch Variants

In the search for better reproducibility and performance, the original 2-wire x-pinch evolved into multi-wire (4 – 12 wires, Fig. 2.6(a)) and "nested" x-pinches [54, 55]. By adding more wires, the $\mathbf{J} \times \mathbf{B}$ force gains better initial inward radial symmetry which helps to further localize the hotspot. The nested x-pinch construction involves coaxially layering different wire materials around a central thick wire as shown in Fig. 2.6(b). For instance, the red central wire could be 25.4 μm NiCr, the blue layer could be six 20.3 μm Mo wires, and the green outer layer could be twelve 17.6 μm W wires, as was used in Ref. [56].

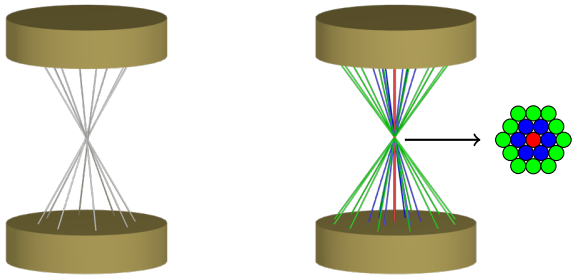

Figure 2.6: (a) Multiwire x-pinch. (b) Color-coded nested x-pinch with view of the densely packed twist-point cross section.

The hybrid x-pinch (see Fig. 2.7) is the latest x-pinch redesign which incorporates solid electrodes that are drilled out along their axis to accept a fine wire passed through the middle [57]. The electrode ends nearest the pinch point are machined to 30° relative to the pinch axis, similar to the angle of the original x-pinch legs. The gap spacing between the anode electrode and cathode electrode is typically 0.5 – 2mm, depending on the driver parameters. There are numerous benefits to this configuration. The setup is much less complicated and time consuming than arranging a multiwire x-pinch, only requiring a single wire to be placed and electrode gap to be set. Generally, the electrodes are

reusable over many shots, only requiring a polishing or a quick remachining on a lathe. The x-pinch dynamics are similar to the standard x-pinches with respect to hotspot formation and thermal x-ray burst duration [58]. An added benefit of the hybrid x-pinch is the absence of strong electron beam formation which is due to the electrode plasma closing the gap shortly after the thermal burst and dissociation, thereby minimizing any potential for electron acceleration.

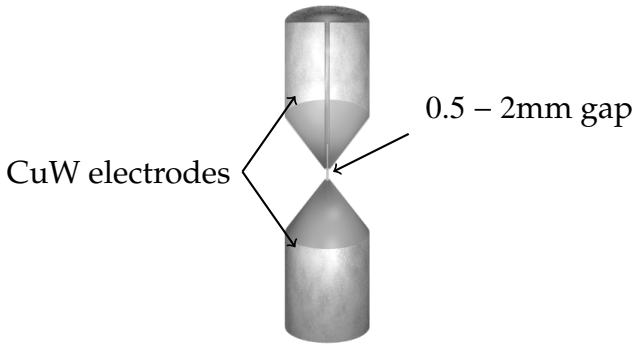

Figure 2.7: The hybrid x-pinch is composed of two CuW electrodes bridged by a fine wire. The top electrode is cut away to show the wire feed-through hole.

2.5 XRTS Source Requirements

X-ray Thomson scattering experiments have historically and predominantly been achieved at large facilities with laser-produced plasma x-ray sources where kilo-Joules of laser energy are converted to x-ray probe radiation [3].

Two types of x-ray emission can occur with laser-plasma sources depending on the pulse-width of the laser. Thermal x-ray sources which can emit He_α and Ly_α radiation are created with relatively longer pulse widths in the range 0.1 – 1ns [14]. The typical laser intensities required for optimum conversion efficiency for thermal x-ray sources is $10^{14} - 10^{16} W/cm^2$. The second type of x-ray

radiation from laser-plasma interactions requires a short-pulse ($\lesssim 10^{-13}$s) to create fast electrons that can create relatively cold K_α characteristic radiation from inner-shell transitions [59]. Laser intensities $> 10^{16} W/cm^2$ are required to effectively drive this process. Both of these types of radiation sources have been successfully used in XRTS experiments [10, 60].

Stringent bandwidth requirements have been determined for an x-ray source to function as an x-ray Thomson scattering probe source in both the collective and noncollective scattering regimes [8, 61, 62]. When probe photons undergo Compton scattering in the dense plasma they are downshifted in energy by an amount determined by the scattering angle, θ, and the incident probe energy, E_0:

$$E_C = \frac{\hbar^2 k^2}{2m_e} \tag{2.2}$$

where

$$k = |\mathbf{k}| = \frac{4\pi E_0}{hc} \sin(\theta/2) \tag{2.3}$$

This downshifted spectral feature is referred to as the *inelastic* or Compton feature. If the width of the spectral line being used for the probe is wider than $E_0 - E_C$, then resolving the inelastic scattered feature will be difficult when considering Doppler broadening effects that will additionally widen the Compton feature. A spectral bandwidth of $\lessapprox 1\%$ has been shown to be suitable for noncollective XRTS experiments which are characterized by large backscattering angles and high probe energies providing a large Compton shift.

The largest restriction in any XRTS experiment is the number of x-ray probe photons, N, able to be produced into 4π steradian within the spectral bandwidth. Only a small fraction of these photons will intercept the scattering volume which subtends some solid angle, $\Omega_{trgt} \approx 0.001 - 0.1$ steradian. Typical

numbers from the literature for N from laser-produced plasma x-ray sources into the scattering volume range from $10^{11} - 10^{15}$ [1, 10, 8]. The author can find no previously determined hard lower limit on N that would result in no scattered x-ray signal from a target near solid density. This is ultimately determined by collection efficiency, detector sensitivity and background levels, all of which vary from experiment to experiment.

2.5.1 Laser-produced Plasma Source Brightness Example

The 4.75keV Ti He_α spectral feature produced from thermal laser-produced plasma x-ray sources has been successfully used in noncollective XRTS experiments in the past [2, 18, 16]. An example calculation of the brightness of such a thermal source is derived by Glenzer *et al.* in [8]. The authors assume a conversion efficiency of $\approx 0.4\%$ into a bandwidth of $\Delta E/E = 0.5\%$ based on a $1kJ$ laser pulse of $100ps$ and intensity of $10^{15} W/cm^2$ onto $1mm^2$. This yields approximately 10^{15} photons into 4π steradian, resulting in a brightness (or brilliance) of $\approx 10^{18}\ photons/s/mm^2/mrad^2/0.5\%BW$.

2.6 Hybrid X-pinch Source Brightness and Photometrics

The abundance of experimental laser-produced x-ray source XRTS data using the Ti He_α line and the detailed study of the Ti x-pinch by numerous authors within the Laboratory of Plasma Studies makes it an ideal candidate for development as a new XRTS probe source. The problem is to determine if the thermal Ti He_α line radiation produced from an x-pinch is bright enough. Sim-

ply determining a photon count may seem sufficient. However, source size and burst duration could be important in future XRTS studies involving the hybrid x-pinch, as these may affect the experimental spatial and temporal resolution achievable in the scattering experiment. Since these values have been measured for Ti x-pinches by numerous authors, we can readily use them in the brightness calculation [51, 63, 38].

The brightness measurement scheme involves focusing the Ti He_α line using a perfect, spherically-bent Ge(400) monochromator onto an SR or TR image plate and then using the image plate response, η_{ip}, (which must include the magnification factor due to the spherically-bent optic and the attenuation due to any filtering) to convert to photons. Knowing the x-ray burst duration, τ_{src} (s), the x-ray source size area, A_{src} (mm^2), the throughput efficiency of the x-ray optic, Ω_{opt} $(mrad^2)$, and the relative bandwidth of the chosen line $(\%\ BW)$ is enough to convert to units of *brightness* to compare with the previous calculation of Glenzer. A model of the experiment arrangement is shown in Fig. 2.8.

$$Brightness = \frac{\eta_{ip}}{\tau_{src}\ A_{src}\ \Omega_{opt}\ 0.5\%BW} \rightarrow \frac{[photons]}{[s]\ \ [mm^2]\ \ [mrad^2]\ \ [\%BW]} \tag{2.4}$$

The synchrotron community has arbitrarily settled on the convention of $0.1\%BW$ for their brightness calculations due to their ability to select continuum radiation with perfect, flat monochromators from the beamline instead of thermal line radiation. The width of the Ti He_α resonance line is approximately 24eV at a central energy of 4750eV, giving a bandwidth of $\approx 0.5\%$.

The following brightness analysis is based on a single $100\mu m$ Ti hybrid x-pinch in the main current path ($1MA$ peak current) on COBRA. A spherically-bent Ge(400) x-ray optic was placed $82cm$ away from the source which focused the collected spectrum onto a TR-type image plate filtered with $20\mu m$ of alu-

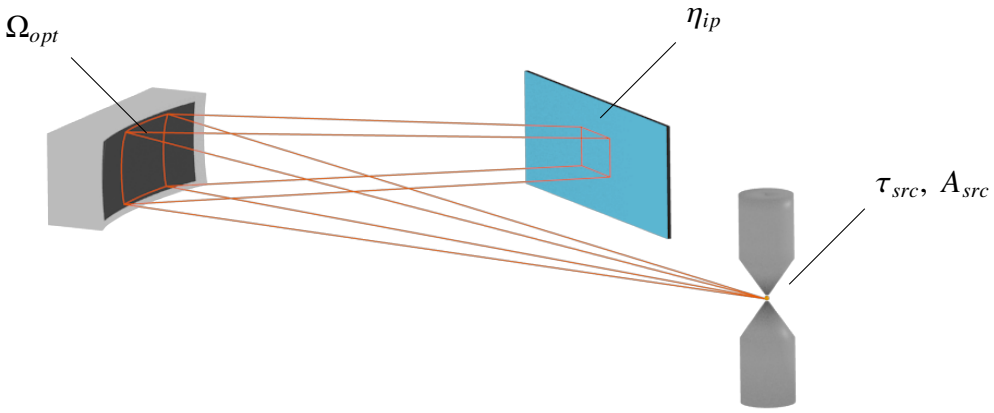

Figure 2.8: A spherically-bent Ge(400) x-ray optic collects light from an x-pinch and focuses it onto an image plate.

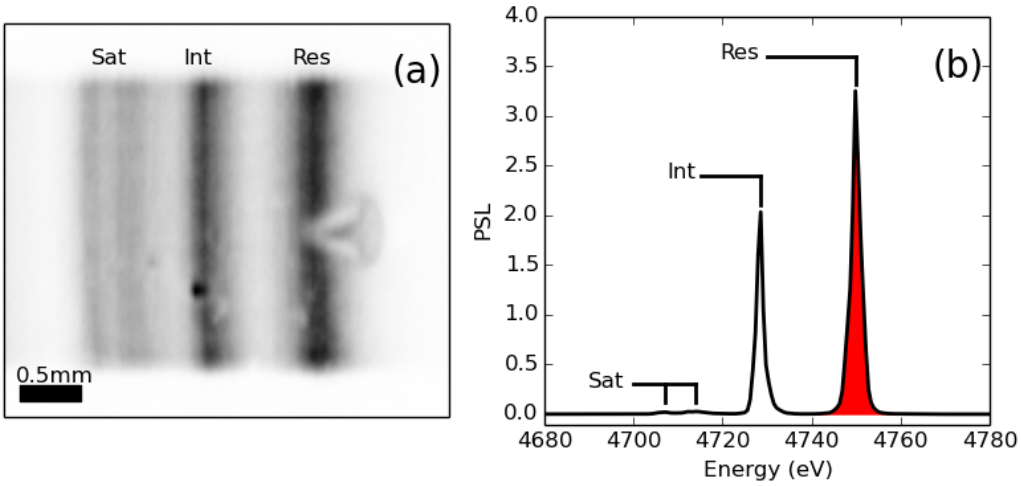

Figure 2.9: (a) Ti He_α spectrum with indicated resonance (Res), intercombination (Int) and satellite (Sat) features. (b) Intensity profile in units of photo-stimulated luminescence (PSL). The red region indicates a 0.5% bandwidth.

minum. The collected spectrum is shown in Fig. 2.9(a). An intensity profile taken across the spectrum is shown in Fig. 2.9(b). The original 16-bit grayscale intensity units have been converted to photo-stimulated luminescence (PSL)

units (see Ch. 4) according to

$$PSL = \left(\frac{R}{100}\right)^2 \left(\frac{4000}{S}\right) 10^{L\left[\frac{G}{2^B-1}-\frac{1}{2}\right]} \tag{2.5}$$

where R, S, L, G, and B are the scan resolution (25 μm), scanner sensitivity (1000), scanner latitude (5), original grayscale value and bit value (16), respectively [64].

The 0.5%BW region (red area under intensity profile curve) covers approximately 9×10^5 μm^2 on the scanned image plate. This is the entire resonance line of the Ti He_α feature. From the intensity profile, the FWHM value is near 1.5 PSL. Taking this as the average for a single pixel translates to a total area PSL value of about 2×10^3 when we consider 625 $\mu m^2/px$. The source diameter and burst duration are estimated to be no larger than 25 μm and no longer than 500 ps [63].

The source diameter converts to an area of approximately 490 μm^2 (0.00049 mm^2). The ratio of the area of the resonance line to the source area indicates a magnification factor of approximately 1×10^3. The 20 μm thick Al filter only transmits about 30% of the photons through. Combining these factors with the 2.5 PSL per x-ray photon response of the TR-type plate results in a total of approximately 2.6×10^9 photons being focused by the Ge(400) optic. The collection solid angle was estimated to be around 10^{-6} sr (1 $mrad^2$) (see Sec. 3.7).

Plugging these values into Eqn. 2.4 yields a brightness value of $\approx 10^{22}$ $photons/s/mm^2/mrad^2/0.5\%BW$. This value is 4 orders larger than that reported by Glenzer for the laser-produced x-ray source. The amount of photons produced by the x-pinch within the 0.5% BW is about 2×10^{15} photons/sr or about 2.5×10^{16} photons into 4π. This gives good agreement with the PCD-based photometric estimates from Sec. 1.4.6.

CHAPTER 3

X-RAY OPTICS

3.1 Introduction

In 1913, W. L. Bragg and W. H. Bragg (son and father, respectively) published their findings on the reflections of x-rays from crystals [65]. In the years since, x-ray spectroscopists have utilized the Braggs' discovery to their advantage by employing crystals of various makeup for the purpose of collecting the emitted x-ray spectra from a plasma and using this information diagnostically to gain an understanding of the physics of the plasma [66][67]. The crystals can range from quite expensive to relatively cheap, depending on material and quality. For instance, we commonly bond cheap, thin mica or KAP (*potassium acid phthalate*) to our own custom built subtrates or optical-quality substrates purchased from an optics manufacturer. In most cases, these custom-built optics are of excellent spectral quality, allowing us to collect high-quality data. Their imaging quality is usually not exceptional due to the imprecise nature of the bonding process we employ. We have also purchased x-ray optics of quartz and germanium from optics manufacturers such as *Inrad Optics*. These optics are much more expensive, but their spectral *and* imaging quality are both superb.

X-ray optics are relatively easy to place and align in an experiment on COBRA (detailed in Ch.6), requiring only a small laser pointer and rotation/translation stage. Care should be taken if the optic is close to a load that can produce debris as this has the potential to render an expensive optic broken and useless. A few layers of mylar or polypropylene placed between the optic and the load will usually suffice. If one is unsure of the amount of debris the

load can produce, a cheaper sacrificial optic should be used for the first few experiments until a high degree of optic-survival confidence is attained, though this is *not* an absolute guarantee of optic survival. *If something can go wrong, it will go wrong...*

A full discussion of the physics of the reflection of x-rays from crystal structures is beyond the scope of this thesis. The following section will provide an introduction to a few key concepts about crystals and Bragg's Law. It will also explain how the efficiency of an optic is determined along with certain focusing and resolution details that will be referred to again in the x-ray Thomson scattering experiments that follow in later chapters. The reader is referred to any crystallography or solid state physics text for a thorough discussion of the subject of Bragg diffraction [68].

3.2 Crystal Structure and Bragg Diffraction

Crystalline solids are characterized by a repeating ordered structure. The two concepts needed to fully define the crystal are the *lattice* and the *basis*. The lattice is a purely mathematical construct that can be defined as

$$L(\mathbf{r}) = \sum_i \sum_j \sum_k \delta(\mathbf{r} - \mathbf{R_{ijk}}) \tag{3.1}$$

where

$$\mathbf{R_{ijk}} = i\mathbf{a} + j\mathbf{b} + k\mathbf{c} \tag{3.2}$$

The i, j, k coefficients are arbitrary integers and $\mathbf{a}, \mathbf{b}, \mathbf{c}$ are the primitive lattice vectors that define a unit cell, i.e., $|\mathbf{a} \cdot \mathbf{b} \times \mathbf{c}|$ is the smallest repeatable volume within the crystal. The basis is simply the smallest group of repeating atoms or

molecules within the crystal, i.e., a unit cell's worth of atoms. The basis atom locations can be defined mathematically by

$$\Gamma_{cell}(\mathbf{r}) = \sum_n x_n\mathbf{a} + y_n\mathbf{b} + z_n\mathbf{c} \tag{3.3}$$

where $0 \leq x_n, y_n, z_n \leq 1$ and the sum is over all atoms making up the basis. In a geometric sense, the entire crystal can be constructed by copying and translating the basis to each lattice point. This process of crystal construction (depicted in Fig. 3.1) can be understood mathematically by convolving Eqn. 3.1 with Eqn. 3.3

$$\begin{aligned}
\Gamma(\mathbf{r}) &= L(\mathbf{r}) \otimes \Gamma_{cell}(\mathbf{r}) \\
&= \int_{-\infty}^{\infty} L(\mathbf{r}_1)\Gamma_{cell}(\mathbf{r} - \mathbf{r}_1)d\mathbf{r}_1 \\
&= \int_{-\infty}^{\infty} \sum_i \sum_j \sum_k \delta(\mathbf{r}_1 - \mathbf{R}_{ijk})\Gamma_{cell}(\mathbf{r} - \mathbf{r}_1)d\mathbf{r}_1 \\
&= \sum_i \sum_j \sum_k \int_{-\infty}^{\infty} \delta(\mathbf{r}_1 - \mathbf{R}_{ijk})\Gamma_{cell}(\mathbf{r} - \mathbf{r}_1)d\mathbf{r}_1 \\
&= \sum_i \sum_j \sum_k \Gamma_{cell}(\mathbf{r} - \mathbf{R}_{ijk})
\end{aligned} \tag{3.4}$$

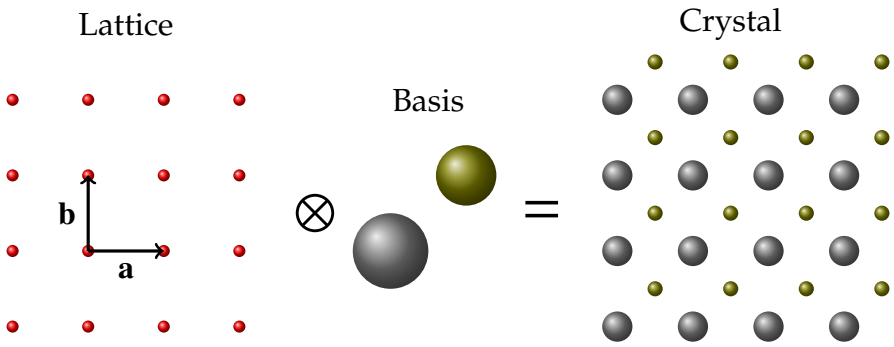

Figure 3.1: A 2-D example of crystal construction using a lattice and a basis. The crystal can be understood mathematically as the convolution of basis with lattice.

Due to the symmetry inherent in a crystal, families of parallel planes exist throughout the lattice. A convenient notation exists to distinguish one family of planes from another through the use of the so-called Miller indices, (h, k, l).

Crystallographers and optics manufacturers will typically denote the crystal makeup and indices together, e.g. Si(111). The indices are determined by finding where along the individual lattice vectors the plane intercepts, taking the inverse of these numbers, clearing the fractions and reducing to lowest terms. For instance, the red plane in Fig. 3.2 intercepts the lattice vectors at $\frac{1}{2}, \infty, \infty$ (planes parallel to lattice vectors intercept at ∞). The inverse of these numbers are $2, 0, 0$, thus this plane is denoted as the (200) plane. Planes which intercept at negative values along an axis are indicated by a bar above the index, e.g.,$(\bar{1}00)$.

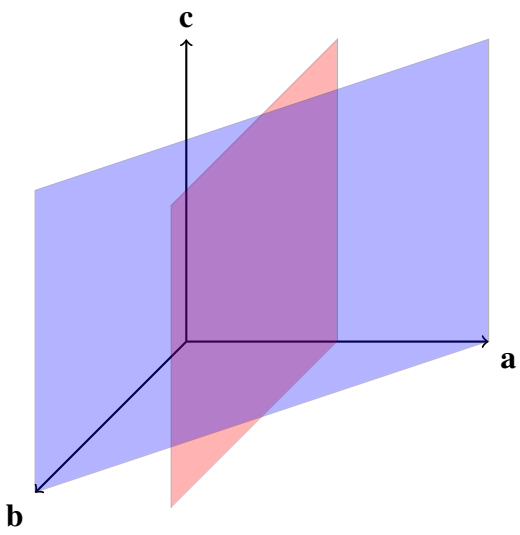

Figure 3.2: The (200) plane in red and the (110) plane in blue.

Reflection of x-rays from a lattice plane can occur for certain combinations of wavelength (λ) and grazing incidence angle (θ) according to Bragg's Law of Diffraction:

$$m\lambda = 2d_{hkl} \sin\theta_B \tag{3.5}$$

where m and d_{hkl} are the reflection order and lattice plane spacing, respectively. Equation 3.5 can also be conveniently recast as

$$m\lambda = 2d_{hkl} \cos\theta_n \tag{3.6}$$

where the normal incidence angle $\theta_n = 90° - \theta_B$ is an experimentally easier variable to verify and align.

In Fig. 3.3, radiation is incident upon a crystal plane at an angle, θ_b, that satisfies Eqn. 3.5. A detector viewing the scattered radiation at the corresponding angle of reflection will see constructive interference of the scattered waves (shown in blue). Another detector observing at an angle of reflection that does not equal the angle of incidence will detect nothing due to destructive interference of the scattered wave (shown in red). In this manner, the crystal structure acts as a monochromator as possibly many different wavelengths can be incident at the same angle, but only a specific wavelength will satisfy Eqn. 3.5. In order to use a crystal for studying a particular wavelength of radiation, it follows from Eqn. 3.5 that $2d \geq m\lambda$.

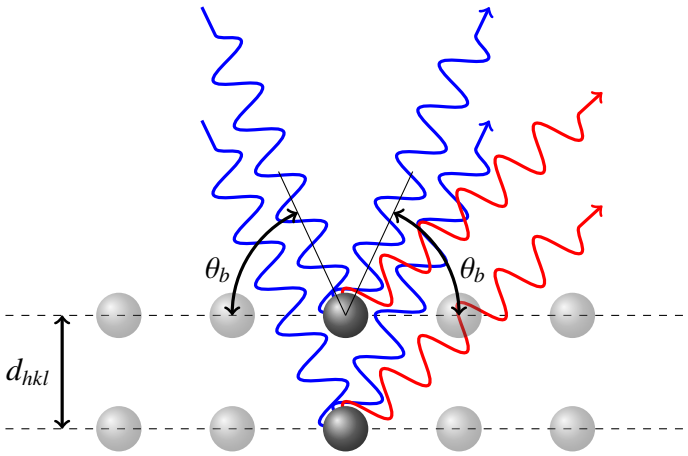

Figure 3.3: Waves of proper wavelength and incidence angle will constructively interfere when viewed at the Bragg angle while destructive interference will result in no observed reflection if viewed off-angle.

Two particular crystals used extensively in this thesis are Ge(400) and HAPG (*highly annealed pyrolytic graphite*)[69]. Germanium forms a diamond structure which is a subset of the *cubic* structure. The d-spacing for cubic crystals is given

by

$$d_{hkl}^{cubic} = \frac{a}{\sqrt{h^2 + k^2 + l^2}} \tag{3.7}$$

where $a = |\mathbf{a}| = |\mathbf{b}| = |\mathbf{c}|$. The graphite found in HAPG forms a hexagonal close-packed structure (hcp) whose d-spacing is determined by

$$d_{hkl}^{hex} = \left[\frac{4}{3a^2}(h^2 + hk + k^2) + \frac{l^2}{c^2} \right]^{-1/2} \tag{3.8}$$

where $a = |\mathbf{a}| \neq |\mathbf{c}| = c$. The details for the crystals relevant to this study are presented in Table 3.1.

Table 3.1: Crystals used extensively.

Crystal	**Miller Indices**	**a** (Å)	**c** (Å)	**2d** (Å)
Ge	(400)	5.658	5.658	2.82
HAPG	(002)	2.461	6.708	6.708

3.3 Reflectivity Profiles and Integrated Reflectivity

According to Eqn. 3.5, only photons of a single wavelength, λ, will be reflected at a given incidence angle. In reality, there is an intrinsic reflection width due to refraction, absorption and multiple scattering within the crystal which allows reflections to occur that deviate slightly from θ_B by some small amount $\pm\Delta\theta/2$. This reflection profile, $R(\theta)$, is referred to as the *rocking* curve or *reflectivity* curve in the literature [70, 71]. It is measured experimentally by recording the reflected intensity as a function of incidence angle as the crystal is rotated or "rocked" through the Bragg condition as a highly collimated beam of photons impinges the crystal surface.

The previous section defined crystalline structure as a perfect, ordered repeating lattice that fills all space. In practice, the macroscopic finite-sized crys-

tals used for x-ray spectroscopy are rarely considered perfect across their entire volume; they are usually interspersed with dislocations and voids. These imperfections lead to wider and lower reflectivity curves. As an approximation, the rocking curve can be considered Gaussian in nature and therefore fully defined by a peak reflectivity, R_0, and a full-width at half-maximum (FWHM) measurement across the rocking curve, $\Delta\theta_{rc}$.

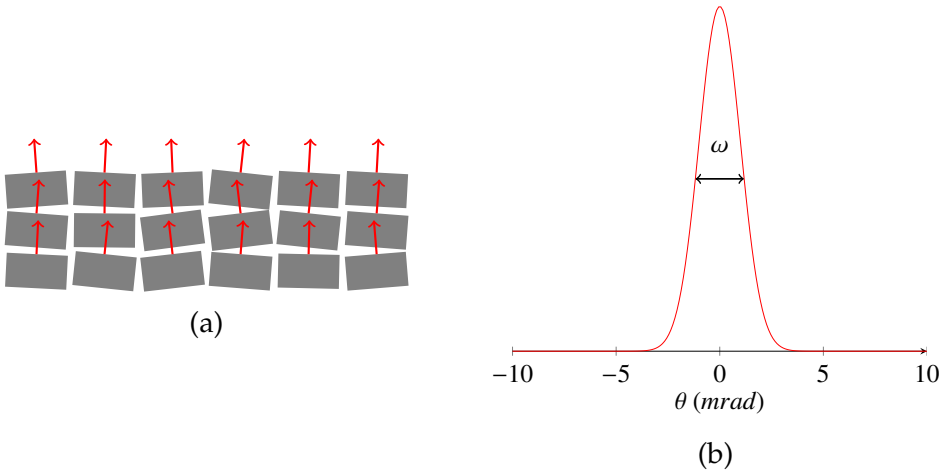

(a) (b)

Figure 3.4: (a) Idealized model of imperfect or mosaic structure. (b) The crystal is composed of tiny, perfect crystallites with randomized normal vectors that fit a Gaussian distribution. The FWHM of this distribution is the mosaic spread of the crystal.

Reflectivity profiles for perfect and imperfect crystals can also be calculated using *dynamical* diffraction theory, as put forth by Darwin [72, 73] and *kinematic* diffraction theory, respectively. The kinematic approximation (also known as weak-scattering approximation) is a simpler theory which ignores multiple scattering effects and assumes reflections take place from small, perfect crystallites with random orientations throughout the crystal region as shown in Fig. 3.4a. These types of crystals are known as *mosaic* crystals and have a defined mosaicity or mosaic spread, ω, which is a measure of the angular spread of the normal vectors of the random crystallites (Fig. 3.4b). Calculations for curved crystals, such as cylindrically or toroidally bent, involve using the finite-difference

method to solve a system of hyperbolic partial differential equations known as the Takagi-Taupin equations which are derived from Maxwell's equations in a deformed periodic medium [74].

Raytracing and x-ray optics programs such as *SHADOW* and *X-ray OPtics (XOP)* are conventionally used to determine the optical properties of an x-ray system [75, 76]. SHADOW/XOP contains many useful subroutines for numerically calculating the reflectivity profiles of flat and bent, perfect or mosaic, x-ray optics. An example calculation is shown in Fig. 3.5 for a flat Quartz(100) and spherically-bent Ge(400) optic.

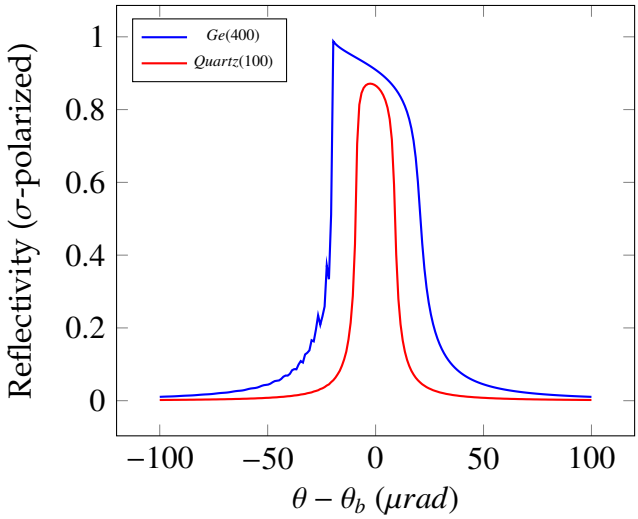

Figure 3.5: Example reflectivity profiles calculated by the XOP subroutine *Xcrystal*.

A second, and experimentally more useful, characterization metric exists in the form of the *integrated reflectivity*. Not surprisingly, it is obtained by integrating the reflectivity curve:

$$R_{int} = \int_{-\infty}^{\infty} R(\theta) d\theta \tag{3.9}$$

R_{int} has units of radians and can be used to determine the collection efficiency of an x-ray optic in an experiment. Imperfect or mosaic crystals will have lower

and wider rocking curves, but their R_{int} will generally be much greater than a perfect crystal, leading to enhanced efficiency.

The upper and lower limits on integrated reflectivity can also be calculated analytically using the kinematic and dynamical theories of diffraction. The R_{int} of a real crystal will fall somewhere between these limits. Perfect, flat crystals will be closer to the dynamical limit, R^P_{int}, while bent crystals will approach the kinematic model limit, R^M_{int}. If the measured R_{int} is in good agreement with the kinematic limit then the crystal can be considered *ideally* mosaic [77]. Thermal corrections are sometimes included, but I have left them out for simplicity:

$$R^P_{int} = \frac{8}{3\pi}\frac{\lambda^2 r_e |F_{hkl}|}{v_c sin(2\theta)}\left(\frac{1+|cos(2\theta)|}{2}\right) \tag{3.10}$$

$$R^M_{int} = \frac{1}{2\mu}\frac{\lambda^3 r_e^2 |F_{hkl}|^2}{v_c^2 sin(2\theta)}\left(\frac{1+cos^2(2\theta)}{2}\right) \tag{3.11}$$

Both models depend on a fundamental parameter, F_{hkl}, known as the crystal structure factor which describes scattering from the electrons in a unit cell of a crystal [78]. The variables λ and θ are the photon wavelength and the Bragg angle. The parameter v_c is the volume of the unit cell, i.e. $|\mathbf{a}\cdot\mathbf{b}\times\mathbf{c}|$. The constant r_e is the classical electron radius of $2.8179 \times 10^{-15} m$. The variable μ only appears in R^M_{int} and is the linear absorption coefficient (m^{-1}) for the crystal material. Plotted in Fig. 3.6 are the R^M_{int} (red) and R^P_{int} (green) limits for a Ge(400) optic based on Eqns. 3.10 and 3.11.

The XOP subroutine *Xcrystal_bent* was used to numerically calculate an $R_{int} \approx 1.67 \times 10^{-4}$ *rad* using the Takagi-Taupin model based on the parameters of the Ge(400) optic used in this study. The analytical solution from Eqn. 3.10 yields an $R_{int} \approx 1.77 \times 10^{-4}$ *rad*. The disagreement is $\approx 6\%$.

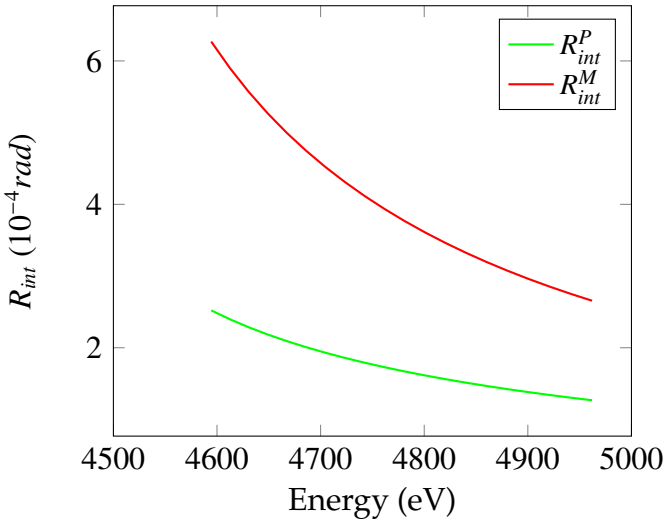

Figure 3.6: The calculated upper and lower limits on integrated reflectivity for a Ge(400) crystal.

3.4 Spherical Focusing

The horizontal (meridional, spectrally dispersive) and vertical (sagittal, non-dispersive) focusing properties of spherically-bent x-ray optics can be determined using proper forms of the Gaussian thin lens approximation formula that is commonly applied to optical lenses [79]:

$$\frac{1}{d_s} + \frac{1}{d_i} = \frac{2}{r_h \, sin\, \theta} = \frac{1}{f_h} \tag{3.12}$$

$$\frac{1}{d_s} + \frac{1}{d_i} = \frac{2 \, sin\, \theta}{r_v} = \frac{1}{f_v} \tag{3.13}$$

where d_s is the source-to-optic distance, d_i is the optic-to-image distance, r_c is the crystal radius of curvature and f is the focal length. The subscripts v and h denote the vertical (sagittal) and horizontal (meridional) planes, respectively. For a spherically-bent optic, $r_h = r_v$.

Shown in Fig. 3.7 in red is another useful conceptual device commonly used in x-ray spectroscopy known as the *Rowland circle*. The plane of the Rowland

circle is not coincident with the plane of the image in this figure, making it appear as an oval. It is a "focal circle" with diameter $D = r_h$ that is tangent to the crystal surface at the point of reflection. If a monochromatic x-ray source is placed on this circle, all x-rays that meet the Bragg criterion will be reflected and focused symmetrically to an image point that also lies on the circle. For a given crystal, every point on the Rowland circle corresponds to a different x-ray wavelength.

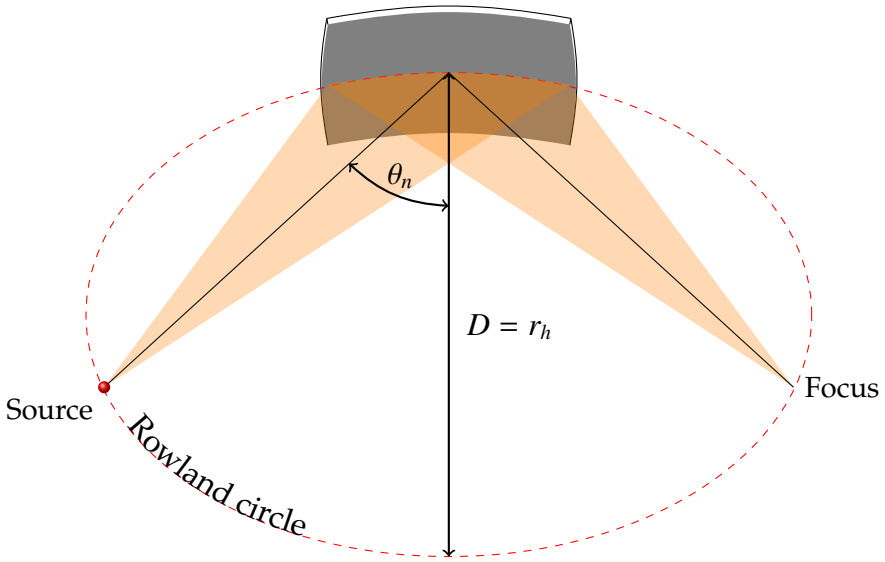

Figure 3.7: The Rowland circle (dashed red) with a diameter equal to the horizontal bend radius of the optic. For a point source placed on the circle, only a single wavelength of radiation that satisfies Eqn. 3.6 will be symmetrically focused to a point.

3.4.1 Astigmatism

Astigmatism occurs when $f_v \neq f_h$. For a spherically-bent optic, astigmatism can generally be ignored for $\theta_b \gtrsim 80°$ as demonstrated in Fig. 3.8. Toroidally-bent crystals with properly chosen r_h and r_v can remove the astigmatism for angles smaller than 80°.

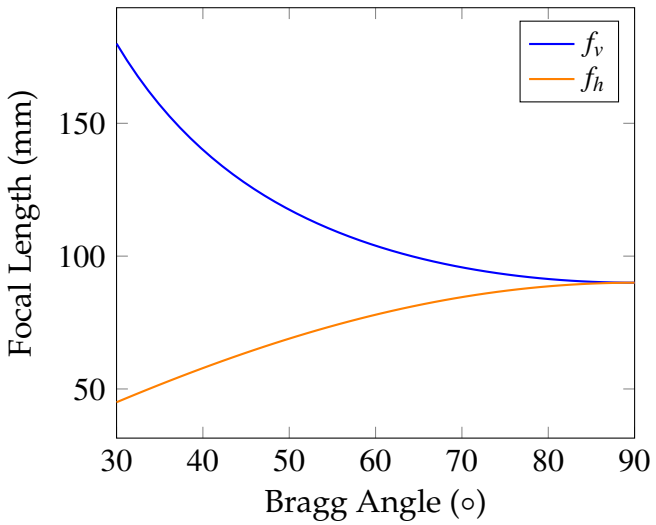

Figure 3.8: The focal lengths in the horizontal and vertical directions as a function of incidence angle.

3.5 Mosaic Focusing

The collection of weak scattering signals is most easily done with highly efficient, ideally mosaic optics such as HAPG which have fundamentally different focusing properties than perfect crystals. A unique property demonstrated in Fig. 3.9 is known as parafocusing [80]. When $d_s \approx d_i$, a photon from a suitably divergent source can, on average, find a crystallite that satisfies the Bragg condition within the bulk of the crystal volume. This allows spectral resolution across a relatively large bandwidth, something that is not generally possible when $d_s \approx d_i$ when using a perfect crystal.

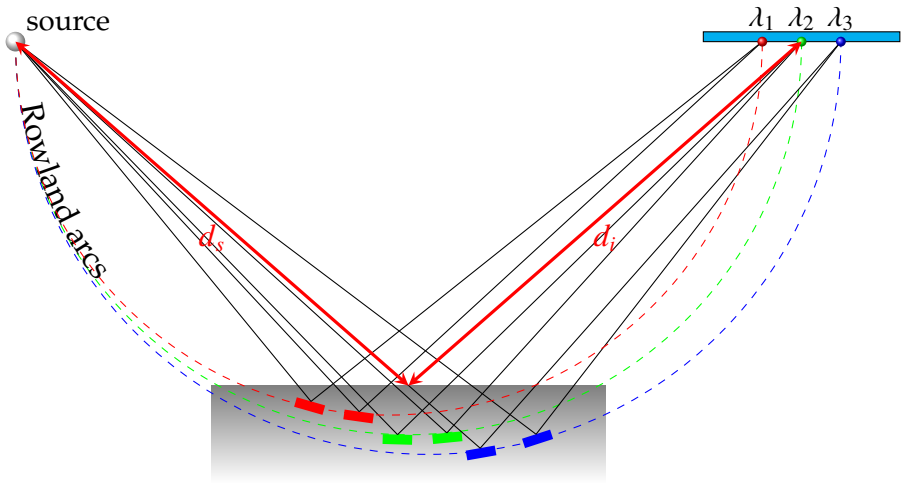

Figure 3.9: An exaggerated model of the parafocusing effect observed in mosaic crystals. When $d_s \approx d_i$, photons of the same energy can find crystallites aligned along a specific Rowland arc, $R \approx \frac{d_s}{2sin(\theta_b)}$, within the bulk of the crystal that will satisfy the Bragg condition.

3.6 Spectral Resolution

The energy resolution or bandwidth of a Bragg spectrometer can be derived using Eqn. 3.5

$$\lambda = \frac{2d}{m} \sin\theta \tag{3.14}$$

$$\Delta\lambda = \lambda' - \lambda = \frac{2d}{m} [\sin\theta' - \sin\theta] \tag{3.15}$$

where,

$$\theta' = \theta + \Delta\theta \tag{3.16}$$

Dividing Eqn. 3.15 by Eqn. 3.14 and substituting Eqn. 3.16

$$\frac{\Delta\lambda}{\lambda} = \frac{\sin(\theta + \Delta\theta) - \sin\theta}{\sin\theta} \tag{3.17}$$

Then using the definition of the derivative,

$$\cos\theta = \frac{\sin(\theta + \Delta\theta) - \sin\theta}{\Delta\theta} \tag{3.18}$$

and allowing $\Delta\theta$ to remain finite, Eqn. 3.17 becomes

$$\frac{\Delta\lambda}{\lambda} \approx \frac{\cos\theta\,\Delta\theta}{\sin\theta} = \frac{\Delta\theta}{\tan\theta} \tag{3.19}$$

Replacing $\Delta\theta$ with the rocking curve FWHM, $\Delta\theta_{rc}$, yields the spectral resolution due to the intrinsic uncertainty of the crystal, $\Delta\lambda_{rc}/\lambda$. For most perfect x-ray optics, this value is typically $1-2$ orders of magnitude smaller than the natural width of a soft x-ray spectral line ($\sim 10^{-3}$).

Geometric contributions can also significantly impact the total resolution and in many cases will be the dominant blurring mechanism. Broadening due to source size is determined by:

$$\frac{\Delta\lambda_{source}}{\lambda} \approx \frac{w}{d_s}\frac{1}{\tan\theta} \tag{3.20}$$

where w is the width of the source and d_s is the source-to-optic distance. Broadening due to penetration depth (volume diffraction) in the optic is determined by:

$$\frac{\Delta\lambda_{depth}}{\lambda} \approx \frac{\lambda_{mfp}\cos^2\theta}{2d_i} \tag{3.21}$$

where λ_{mfp} is the mean-free-path distance in the material and d_i is the detector-to-optic distance. Depth broadening has been shown to be of primary concern for HOPG optics [81]. The individual contributions to broadening are typically assumed to be gaussian in nature, and so the individual terms are summed in quadrature to obtain the total spectral resolution:

$$\frac{\Delta\lambda_{tot}}{\lambda} = \sqrt{\left(\frac{\Delta\lambda_{rc}}{\lambda}\right)^2 + \left(\frac{\Delta\lambda_{source}}{\lambda}\right)^2 + \left(\frac{\Delta\lambda_{depth}}{\lambda}\right)^2} \tag{3.22}$$

3.7 Throughput Estimation

The throughput of an x-ray spectrometer can be defined as:

$$\Omega = \eta_c \, \phi_h \, \phi_v \tag{3.23}$$

where η_c is the efficiency of the crystal and ϕ_h (ϕ_v) is the angle subtended by the actively reflecting portion of the crystal surface relative to the source in the horizontal (vertical) direction. By assuming that the crystal diffracts along its entire vertical height, h_v, ϕ_v can be approximated as h_v/d_s. The efficiency of the crystal is simply the reflectivity, and the horizontal acceptance angle will be limited by the rocking curve width. These two items are related through Eqn. 3.9 and allow Eqn. 3.23 to be rewritten as:

$$\Omega \approx R_{int} \frac{h_v}{d_s} \tag{3.24}$$

For a more accurate estimate of throughput, one must consider the influence of crystal geometry and experiment geometry [82]. To simply demonstrate the effect of geometry on throughput, we consider the reflections in Fig. 3.10. Rays from two different source locations intercept a curved crystal at normal incidence angles θ_n' and θ_n'', diverging by the half-angles ϕ' and ϕ'' from the central ray which intercepts at an angle θ_n. Intrinsic uncertainty allows the prime rays to be diffracted as long as $|\theta_n - \theta_n'| \leq \Delta\theta_{rc}/2$. For the equality case, the rays from s' will subtend a smaller horizontal acceptance half-angle than those from s'' and consequently a smaller throughput value when the full case is considered.

A full geometrical analysis of the throughput was performed and coded into a python script to determine $\Omega \rightarrow \Omega(r_c, h_v, d_s, R_{int})$. The results are plotted in Fig. 3.11 for the r_c = 180mm Ge(400) optic used in the FXRTS experiments (described in Ch.6) on COBRA assuming an $R_{int} = 1.77 \times 10^{-4}$ rad.

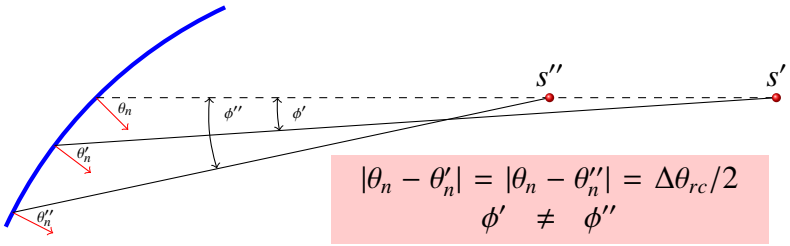

Figure 3.10: The effect of geometry and crystal placement on the horizontal acceptance angle.

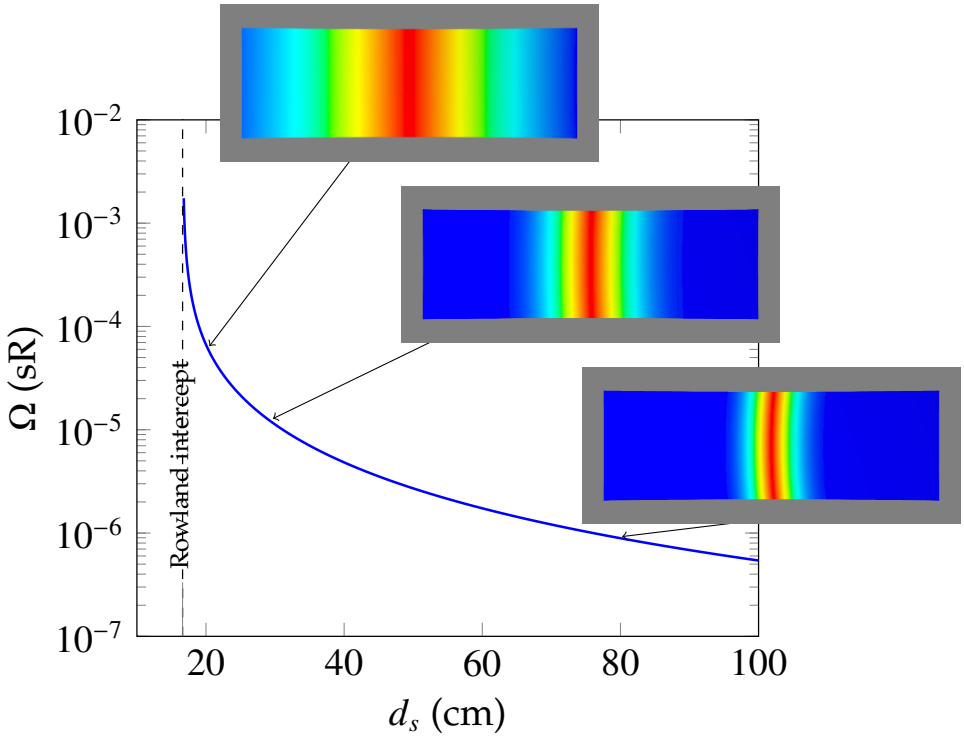

Figure 3.11: Throughput as a function of distance from the source for a spherically-bent Ge(400) optic with a 180mm radius of curvature. The three images are the surface reflection profiles for a 50eV wide line at 20, 30 and 80cm from the source. The strongest reflection intensity is red and the weakest is shown in blue.

As the source moves closer to the Rowland circle position indicated by the vertical dashed line, the throughput approaches an upper limit that is determined by the actual dimensions of the face of the crystal, i.e. the entire face of the optic participates in diffraction and the horizontal acceptance angle will be limited by the optic width and Bragg angle. The three images associated

with the plot are the surface reflection profiles for a 50eV wide line source at 20, 30 and 80 cm distances from the optic calculated with the aid of a custom raytracing program. The strongest reflection intensity is colored in red with the weakest in blue. Clearly, more and more of the surface actively participates in reflection as the optic approaches the Rowland circle intercept distance.

CHAPTER 4

IMAGE PLATES

4.1 Introduction

Image plates (IPs) are a reusable image storage medium capable of detecting ionizing radiation. They have also been used to detect electrons, protons, neutrons and α-particles in addition to photons [83, 84, 85]. Originally invented in the 1980's, they were used heavily within the biomedical industry. Since their creation, they have become increasingly used in high energy density plasma physics experiments due to their high quantum efficiency, robustness, wide dynamic range, linearity and ease of use [86]. Their high quantum efficiency value ($\approx 0.5 - 0.8$) has facilitated the observation of the weak scattering signals found in XRTS experiments [8].

IPs are used in conjunction with a special scanner to retrieve the latent image information. The Laboratory of Plasma Studies currently uses the General Electric produced Typhoon FLA 7000. The IP types used in this thesis are the TR (*tritium*) and SR (*super resolution*) type plates from Fuji BAS (Biological Analysis Systems).

The plates are used exactly as one would use a standard x-ray film in an imaging or spectroscopic mode. They can be trimmed to fit inside the many custom pinhole and slit stepwedge cameras currently employed on XP and COBRA experiments. Despite their numerous advantages over standard x-ray film, the achievable resolution is limited intrinsically by the scanner step-size to $25\mu m$ and further degraded by scattering processes that arise during the scanning pro-

cedure to about $100\mu m$ [87]. If high imaging resolution is required, film is still considered superior due to the $\sim 1\mu m$ grain size.

After use, the IP can be erased by exposure to intense white light for $10 - 30$ minutes. Sometimes, exceptionally intense experimental conditions can cause latent *ghost* images which the author has found difficulty erasing with simple white light exposure. In these cases, replacing 2 of the 5 halogen lamps in the eraser with UV lamps and repeating the erasing procedure seemed to remedy the ghosting in accordance with Ohuchi-Yoshida *et al.* [88].

4.2 Design

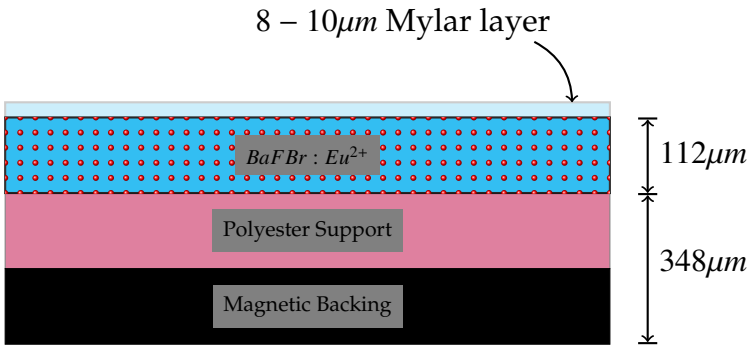

Figure 4.1: Fuji BAS-SR image plate cross-section.

IPs are generally composed of three layers (Fig. 4.1): phosphor, support and ferrite backing.

The support layer and ferrite backing provide mechanical strength and the ability to remain attached to the magnetic scanning tray while inverted during the scanning process. The backing and support layers amount to about 350μm of thickness in total.

The phosphor layer is a flexible crystalline active layer composed of barium fluoro-bromide with trace amounts of bivalent europium ($BaFBr : Eu^{2+}$). The stoichiometry and thickness of the crystalline layer differs depending on the type of plate. The SR-type plate utilizes the previous compound at a thickness of $112\mu m$ while the TR-type is only $60\mu m$ thick and additionally doped with iodine, formulated as $BaFBr_{0.85}I_{0.15} : Eu^{2+}$.

The SR-type also employs a thin $(8 - 10\mu m)$ mylar layer for protection. The TR-type was initially developed to detect weak beta emission during tritium decay and therefore lacks the protective covering.

4.3 Photostimulated Luminescence (PSL)

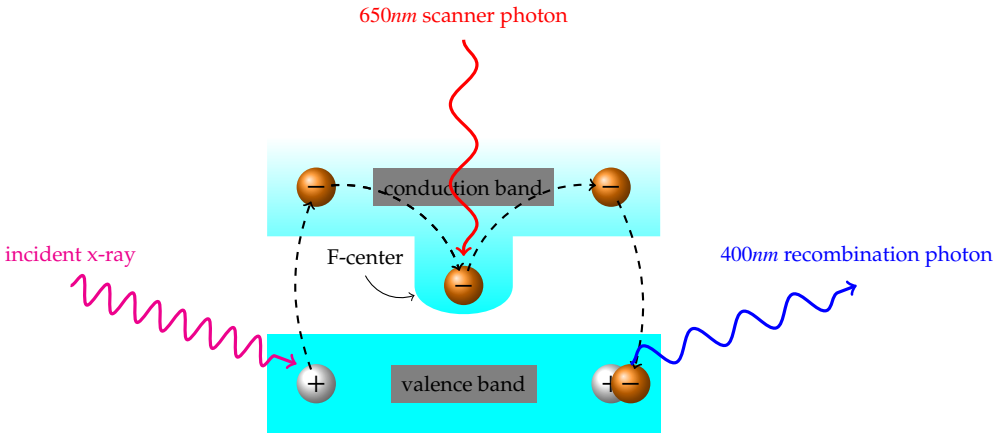

Figure 4.2: The PSL cycle. From left to right, an incidenct x-ray photon liberates an electron into the conduction band where it is trapped in an F-center. Scanner light ejects the electron from the F-center which then recombines in the valence band and emits a recombination photon.

The process of photostimulated luminescence (PSL) is how the latent image is acquired from the crystalline phosphor layer. The entire cycle, which consists of a single electron interacting with three different photons, is shown in Fig. 4.2.

An incident x-ray photon is absorbed by the IP, which converts Eu^{2+} to Eu^{3+} and ejects the electron from the valence band into the conduction band leaving behind a positively-charged hole. The electron can become trapped in a metastable potential well, i.e. lattice defect, known as an *F-center* (from the German *farbe zentrum* for color center).

At this point, the image information is stored by the electron in the F-center and the IP scanner is needed to retrieve it. Random thermal fluctuations can also free the electron from the F-center given enough time, resulting in a less intense final image.

The scanner emits 650nm photons onto the IP, which can give the trapped electron enough energy to escape the potential well. When the electron returns to the valence band and recombines with the positive hole ($Eu^{3+} + e^- \rightarrow Eu^{2+}$), a 400nm recombination photon is emitted which is collected and amplified by a photomultiplier tube. This signal is then digitized and stored in a 16-bit TIFF image file. PSL levels can be recovered using the formula

$$PSL = \left(\frac{R}{100}\right)^2 \left(\frac{4000}{S}\right) 10^{L\left[\frac{G}{2^B-1}-\frac{1}{2}\right]} \tag{4.1}$$

where R is the scan resolution in μm, S is the sensitivity setting (PMT voltage gain for GE scanners), L is the dynamic range or latitude, B is the bit depth, and G is the raw grayscale value. The parameters are chosen before each scan by the user.

4.4 Sensitivity Comparisons to DEF X-ray Film

IP sensitivities have been studied by a few authors over varying bandwidths. Meadowcroft et al. have absolutely calibrated the Fuji BAS IPs (Fig. 4.3) in the energy range of 0 – 100keV and measured the thermally-induced fading as function of time [89]. Haugh et al. have also studied IP sensitivity from 700 – 5000eV and noted a factor of 3 disagreement with Meadowcroft sensitivities within that range that could not be accounted for [90].

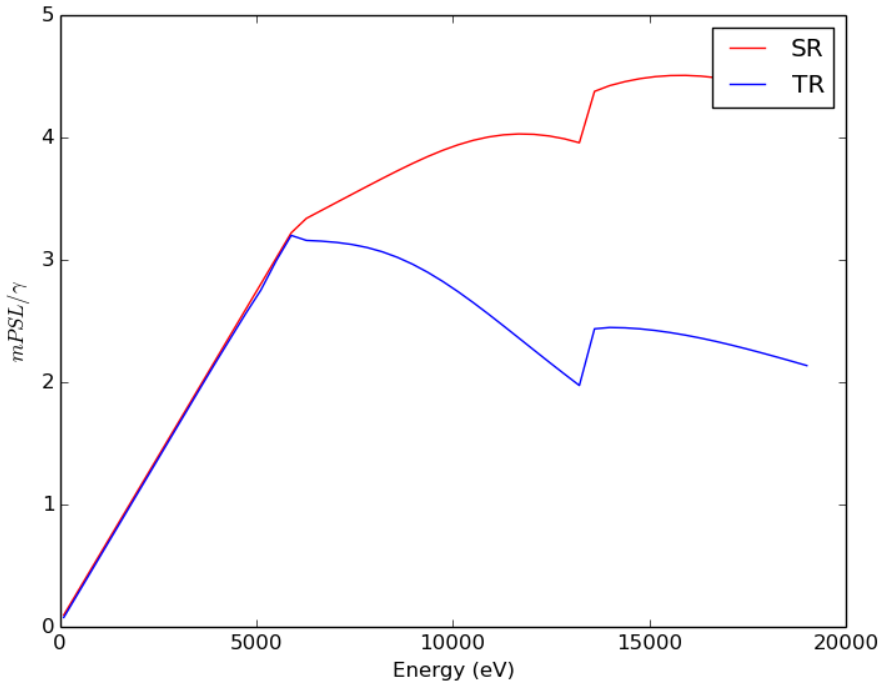

Figure 4.3: Theoretical image plate response curve in units of photo-stimulated luminescence.

DEF (double emulsion film or direct exposure film) x-ray film from Kodak has been characterized most completely by Henke et al.[91]. DEF is no longer produced by Kodak at this time, but a small cache of it was being stored by a few resourceful Russian scientists. The availability and known sensitivity of

the DEF prompted a concise comparison study against the TR and SR IP types, similar in nature to that performed by Chandler et al. in Ref [92] between Kodak Biomax MS and DEF.

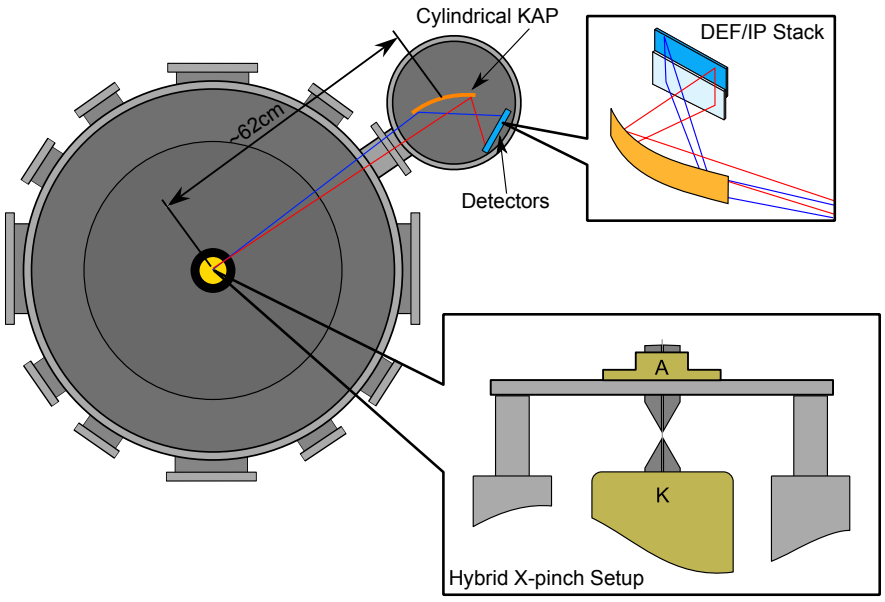

Figure 4.4: DEF/IP sensitivity comparison study experimental arrangement.

The sensitivity comparison study was performed using the XP driver. A small spectrometer body was attached to one of the diagnostic ports on the XP chamber as shown in Fig. 4.4. A cylindrically-bent KAP crystal collected light from an x-pinch in the main load and focused the light onto a detector "stack" composed of DEF/TR, DEF/SR, or TR/SR arranged in an overlapping fashion which allowed the line radiation to fall on both detector types simultaneously as exemplified in Fig. 4.5.

The wire material in the hybrid x-pinch was chosen to provide strong K-shell or L-shell lines in the range of 1 – 5keV. The lines chosen for analysis were an He-like Al line ($2p - 1s$) near 1.59keV, an Na-like Nb line ($3d - 2p$) near 2.42keV, an O-like Mo line ($3p - 2s$) near 3.07keV, and an He-like Ti line ($2p - 1s$) near

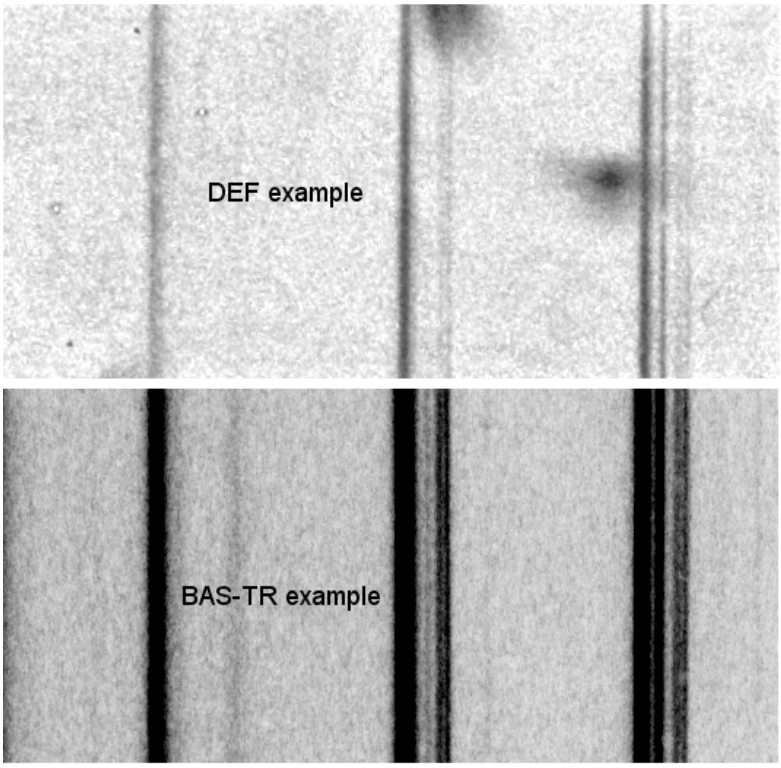

Figure 4.5: DEF/IP detector stack example.

4.75keV.

The DEF chemical development procedure was performed as carefully as possible to match the conditions in Appendix A of Ref. [91]. After development, the DEF films were digitized on a flatbed scanner alongside calibrated neutral density stepwedges and saved in a 16-bit TIFF image file. The TR and SR IPs were scanned with a 25μm step size at a PMT voltage gain setting of 500 (comparable to S 1000 for Fuji scanners) and a latitude setting of 5. The images were saved in a 16-bit TIFF image file.

For each shot number, the two recording media were analysed using the ImageJ program [93] as follows: Depending on the hybrid wire material used, the spectral line in question previously mentioned was identified and an aver-

age intensity, I_{line}, was determined. A suitably uniform area of background was identified and an average intensity, I_{bg}, was determined. The difference of the two values yielded the background-corrected intensity

$$I^c_{line} = I_{line} - I_{bg} \tag{4.2}$$

The values of I^c_{line} for each detector type were then compared. The results of this analysis are shown in Fig. 4.6.

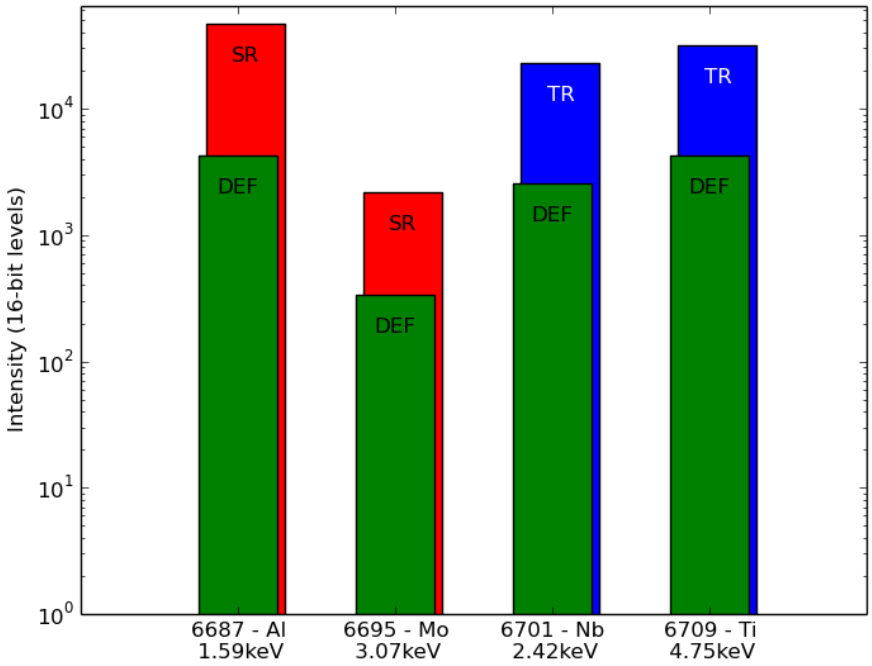

Figure 4.6: DEF vs. IP signal intensity measurements arranged by shot number on XP. The hybrid wire material used as well as the line energy used in the analysis is indicated with the shot number.

From an initial inspection of the plot, the IPs (both TR and SR) show about 10X higher grayscale intensity levels than the DEF for each shot. The average experimental intensity ratio is in fact 8.5 ± 1.7. This agrees with Meadowcroft's analysis of the TR and SR types, which were shown to have similar sensitivies

in this energy range, i.e. if one type outperforms DEF then so should the other to a similar degree in that range.

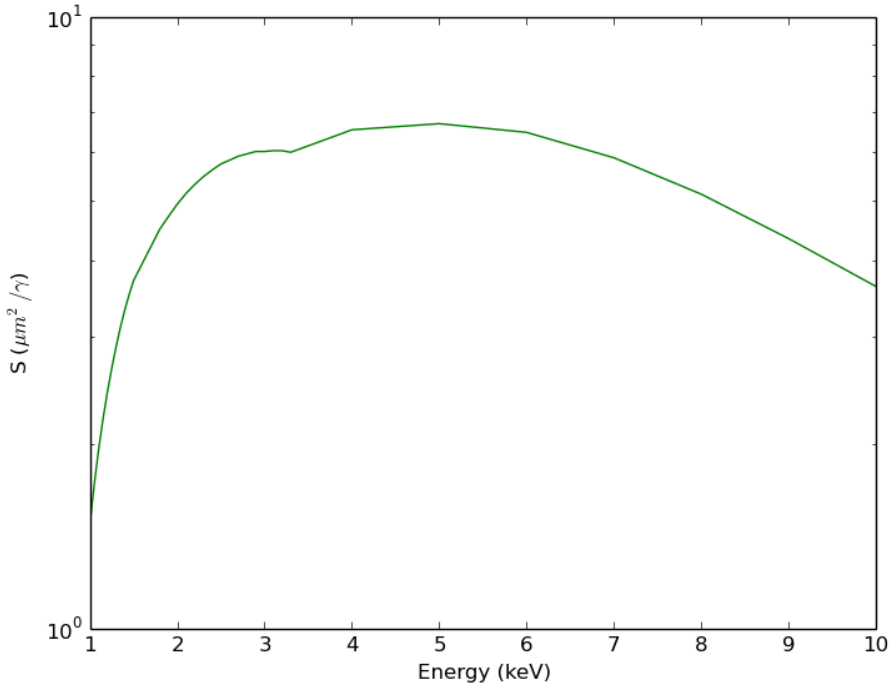

Figure 4.7: DEF sensitivity curve defined by Henke for $D_s = 0.5$.

Henke defined DEF sensitivity in Ref. [91] as the inverse of the intensity (photons/μm^2) required to achieve a specular optical density (D_s) of 0.5. Because the DEF images were scanned with a flatbed scanner and not a calibrated densitometer, the optical density measurements for the sensitivity comparison are actually closer to a diffuse optical density (D_d). The difference between D_s and D_d amount to the way light is collected through the image sample [94]. Henke also provided experimentally measured conversion ratios of D_s/D_d with a first order correction being

$$D_s \approx 1.9 D_d \tag{4.3}$$

where a densitometer using a 0.1×0.1 numerical aperture provided the D_s mea-

surement. Using this conversion, a specular optical density of 0.5 would be converted to a diffuse optical density of about 0.26 which is equivalent to a measured 16-bit grayscale intensity of about 19600 on our stepwedge-calibrated flatbed scanner. This grayscale value can be converted to PSL using Eq. 4.1 to facilitate a change of the sensitivity units of $mPSL/\gamma$ shown in Fig. 4.3 in order to compare to the DEF sensitivity units of $\mu m^2/\gamma$ shown in Fig. 4.7. This is accomplished by multiplying both IP sensitivity curves by the scanned pixel area ($625\mu m^2$) and then dividing by the grayscale-to-PSL conversion ($\approx 2.5\ mPSL$). The modified IP sensitivity curves are plotted in Fig. 4.8 along with the DEF sensitivity curve across the range of interest.

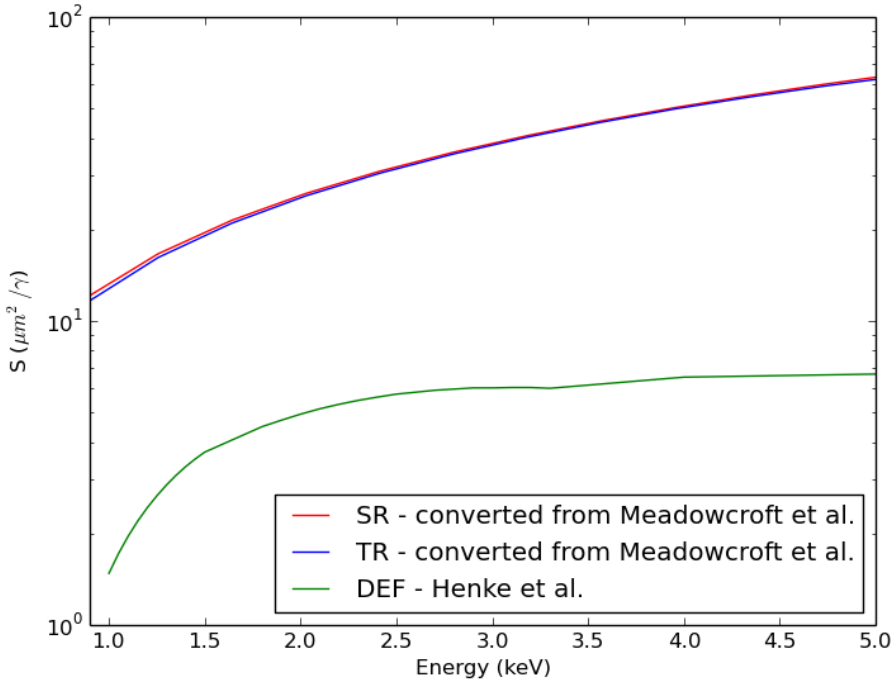

Figure 4.8: DEF and IP sensitivity curves.

Taking an average of the theoretical sensitivity ratios at the energy points of the experimental study yields a value of about 7.1 ± 1.6, indicating good agreement with the observed results.

4.5 TR vs. SR

The relative response of TR and SR was also compared in this range. The results are presented in Fig. 4.9, where a Na-like Ag line ($3d - 2p$) near 3.22keV was used for shot 6698 instead of the Mo line used previously.

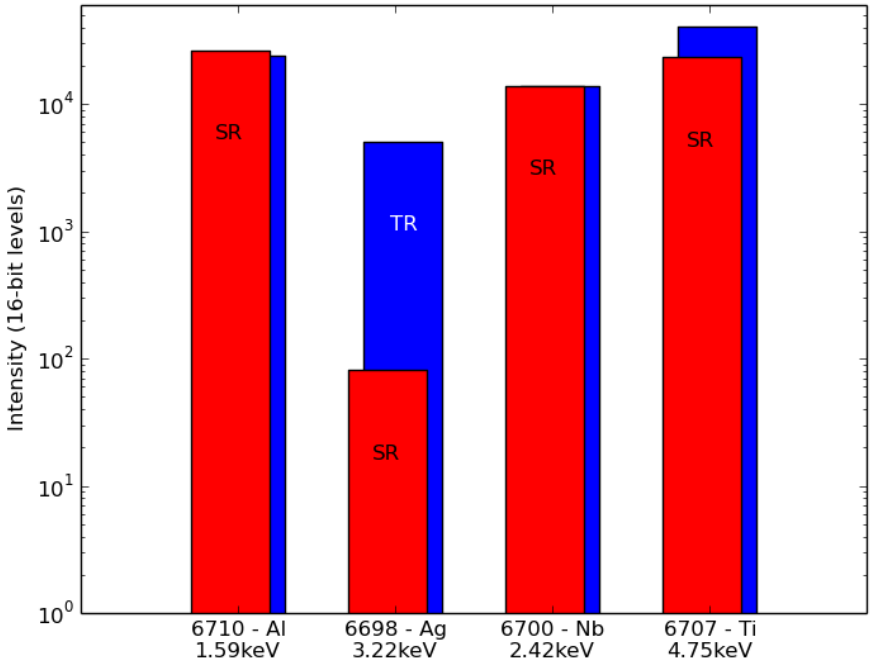

Figure 4.9: SR vs. TR response in the energy range of 1 – 5keV.

Shot 6698 presented an unexpected deviation in the response between SR and TR thought to be due to a large amount of e-beam generated background radiation which resulted in a largely non-linear background correction that severely reduced the value of I^c_{line}. The other shots in the series show TR and SR to have similar responses in accordance with theory. The result of shot 6698 prompted an additional comparison of the signal-to-background ratio between TR and SR IPs.

4.5.1 TR vs. SR Signal-to-Background

The signal-to-background ratio (SBG) is defined here as the ratio of the derived I^c_{line} intensity to the measured I_{bg} intensity. The results of the analysis grouped by shot number are shown in Fig. 4.10.

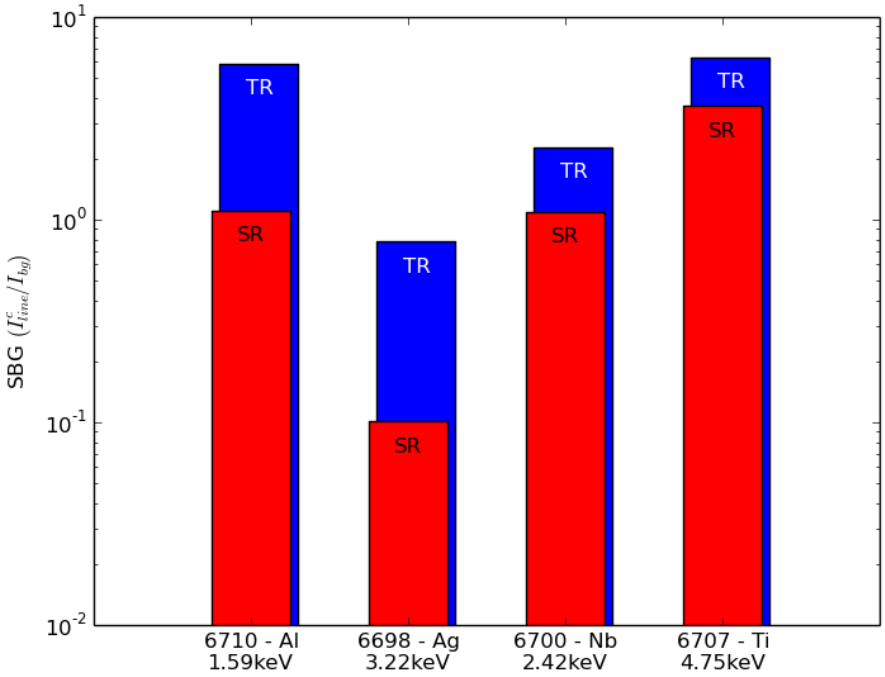

Figure 4.10: Signal-to-background level comparison between SR and TR.

The TR-type IP SBG was superior to the SR-type in every case. This is likely due to the 15% lower density and 46% thinner design of the TR plate which results in less absorbed harder background radiation.

CHAPTER 5

X-RAY THOMSON SCATTERING THEORY

5.1 Introduction

This chapter presents a basic introduction to scattering theory. A working knowledge of scattering theory is needed in order to properly analyze scattered spectra. The analysis of all the scattered spectra obtained in pursuit of this thesis was carried out with the aid of proprietary software called SPECT3D [95]. Proper use of the code requires an understanding of a scattering concept known as the total dynamic structure factor, which will be discussed here.

Many basic electromagnetic theory texts offer a more detailed run through of scattering theory, such as Jackson's *Classical Electrodynamics* or Griffith's *Introduction to Electrodynamics*. An excellent text covering x-ray and neutron scattering is *Elementary Scattering Theory* by D. S. Sivia. For a detailed presentation on Thomson scattering theory with recently updated chapters on x-ray Thomson scattering, *Plasma Scattering of Electromagnetic Radiation: Theory and Measurement Technique* by Sheffield *et al.* is recommended.

5.2 Classical Scattering Theory

When an electromagnetic wave interacts with a free electron, the electron is accelerated by the electric field of the wave, the direction of which is referred to as the wave polarization. Any charged particle undergoing acceleration emits radiation. Therefore the electron can be viewed as a scatterer of the incident

electromagnetic wave.

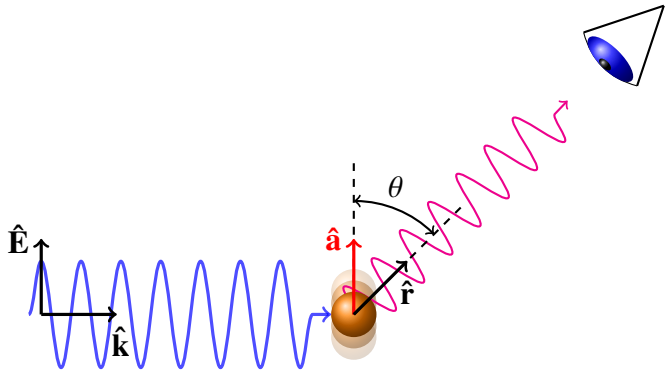

Figure 5.1: The electric field of the incident wave (blue) accelerates the electron (gold sphere) which re-emits radiation (magenta). An observer in the direction of $\hat{\mathbf{r}}$ will see some component of the scattered wave.

If the velocity of the particle is small ($v << c$ where $c \approx 2.99 \times 10^8\ m/s$), the radiated electric field observed at some distance r is given by:

$$\mathbf{E}_{rad} = \frac{q}{4\pi\epsilon_0 c^2 r}(\hat{\mathbf{r}} \times (\hat{\mathbf{r}} \times \mathbf{a})) \tag{5.1}$$

where $\mathbf{a}$ is the acceleration vector and $\hat{\mathbf{r}}$ is the unit vector pointing toward the observer (see Jackson, Ch. 14 [26] or Griffiths, Ch. 11 [96]). It is obvious from the cross product terms that no radiation field is measured when the observer is viewing parallel to the acceleration, *i.e.* $\hat{\mathbf{r}} \parallel \mathbf{a}$, therefore $\hat{\mathbf{r}} \times \mathbf{a} = 0$. A schematic diagram of the scattering process is shown in Fig. 5.1.

The instantaneous power radiated per unit solid angle (W/sr) can now be found with the aid of the Poynting flux:

$$\frac{dP_{rad}}{d\Omega} = r^2|\mathbf{S}| = \frac{r^2|\mathbf{E} \times \mathbf{B}|}{\mu_0} = \frac{r^2|\mathbf{E}|^2}{\mu_0 c} \tag{5.2}$$

where $d\Omega$ is the differential solid angle.

Plugging Eqn. 5.1 into Eqn. 5.2 and simplifying the cross-product terms yields

$$\frac{dP_{rad}}{d\Omega} = \frac{\mu_0 q^2 a^2 sin^2(\theta)}{16\pi^2 c} \tag{5.3}$$

Integrating Eqn. 5.3 over the entire solid angle to get the total radiated power results in:

$$P_{rad}^{total} = \frac{\mu_0 q^2 a^2}{16\pi^2 c} \int_0^{\pi} sin^3(\theta) d\theta \int_0^{2\pi} d\phi = \frac{\mu_0 q^2 a^2}{6\pi c} \tag{5.4}$$

which is the classical result of Larmor for a dipole radiator [96].

The characteristic "donut"-shaped radiation pattern based on Eqn. 5.3 is shown in Fig. 5.2.

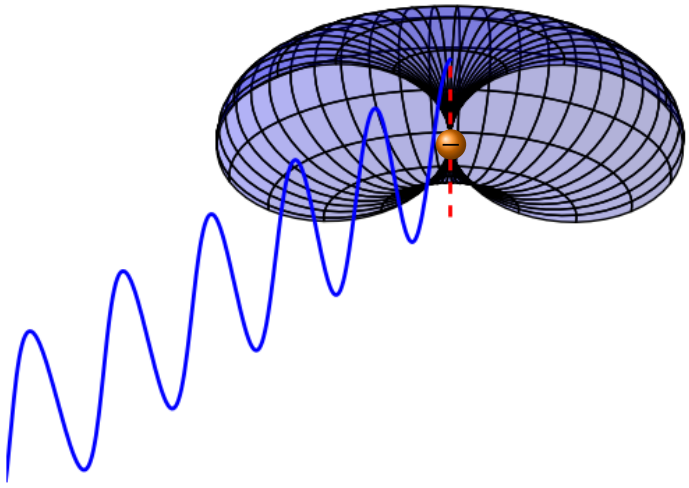

Figure 5.2: The electric field shown in blue accelerates the electron along the dashed red line causing it to emit radiation in a "donut"-shaped pattern. An observer looking down the acceleration axis would see no scattered radiation.

The scattering of light by a free electron just described is known as Thomson scattering. The process is called Rayleigh scattering if the scattering is from bound electrons in atoms or molecules. The physics of Rayleigh scattering differs from Thomson scattering in that the electron is treated as a bound oscillator, introducing an ω^4 frequency dependence for the scattered intensity which is not found in the previous derivations. For an atom or molecule, the bound electrons

act to polarize the atom or molecule in the presence of the incident electric field and collectively radiate as a dipole. When Lord Rayleigh (John Strutt) made his calculations in 1871 [97], the existence of the electron had not yet been proven and would not be until the experiments of Thomson in 1897 [98].

A fundamental quantity involved in all scattering analysis is the Thomson scattering cross section, σ_T, which has dimensions of area and describes how likely a scattering event from a single electron will be. This quantity can be recovered using the time averages of Eqns 5.2 and 5.3 via the following definition:

$$\left\langle \frac{dP}{d\Omega} \right\rangle = \langle S \rangle \frac{d\sigma}{d\Omega} \tag{5.5}$$

where $d\sigma/d\Omega$ is the differential scattering cross-section which has dimensions of area per unit solid angle [26].

We procede by first writing the acceleration of the electron as

$$a = \frac{q|\mathbf{E}|}{m_e} = \frac{qE_0 cos(\omega t)}{m_e} \tag{5.6}$$

where $\mathbf{E}$ is the electric field of the incident wave and m_e is the electron mass ($\approx 9.11 \times 10^{-31}\ kg$). The time average of the a^2 term in Eqn. 5.3 is thus

$$\langle a^2 \rangle = \left\langle \frac{q^2 E_0^2 cos^2(\omega t)}{m_e^2} \right\rangle = \frac{q^2 E_0^2}{2m_e^2} \tag{5.7}$$

allowing the time average of Eqn. 5.3 to be written as

$$\left\langle \frac{dP_{rad}}{d\Omega} \right\rangle = \frac{\mu_0 q^2 \langle a^2 \rangle sin^2(\theta)}{16\pi^2 c} = \frac{\mu_0 q^4 E_0^2 sin^2(\theta)}{32\pi^2 m_e c} \tag{5.8}$$

The time average of the Poynting flux for the incident wave is likewise written as

$$\langle S \rangle = \frac{E_0^2}{2\mu_0 c} \tag{5.9}$$

Dividing Eqn. 5.8 by Eqn. 5.9 now yields the differential scattering cross-section

$$\frac{d\sigma}{d\Omega} = \frac{\mu_0^2 q^4}{16\pi^2 m_e^2} sin^2(\theta) = r_e^2 sin^2(\theta) \tag{5.10}$$

where r_e is the classical electron radius ($\approx 2.8 \times 10^{-15}\ m$).

Finally integrating Eqn. 5.10 over the entire solid angle yields the Thomson scattering cross section:

$$\sigma_T \equiv \int_\Omega \frac{d\sigma}{d\Omega} d\Omega = r_e^2 \int_0^\pi sin^3(\theta) d\theta \int_0^{2\pi} d\phi = \frac{8\pi}{3} r_e^2 \tag{5.11}$$

which has a numerical value of approximately $6.65 \times 10^{-29}\ m^2$.

5.3 Compton Scattering

The equations of the previous section are all based on the premise that light is a wave and that the scattered wavelength, λ', is equivalent to the incident wavelength, λ_0. This wavelength equality implies *elastic* scattering. The experiments of Compton in which the scattering of Mo K_α radiation from graphite blocks resulted in $\lambda_0 \neq \lambda'$, i.e. *inelastic* scattering, were the first convincing experimental evidence demonstrating the quantum nature of light [99].

Compton postulated that the recoil of the scattering electron reduced the energy available to the scattered photon. By using conservation of momentum and Einstein's mass-energy relation, the wavelength increase of the scattered photon was determined to be

$$\lambda' - \lambda_0 = \frac{h}{m_e c}(1 - cos(\theta_s)) \tag{5.12}$$

where h is Planck's constant ($\approx 6.626 \times 10^{-34} J\ s$). The change in wavelength is a function of the observed scattering angle, θ_s, shown in Fig. 5.3. The observed

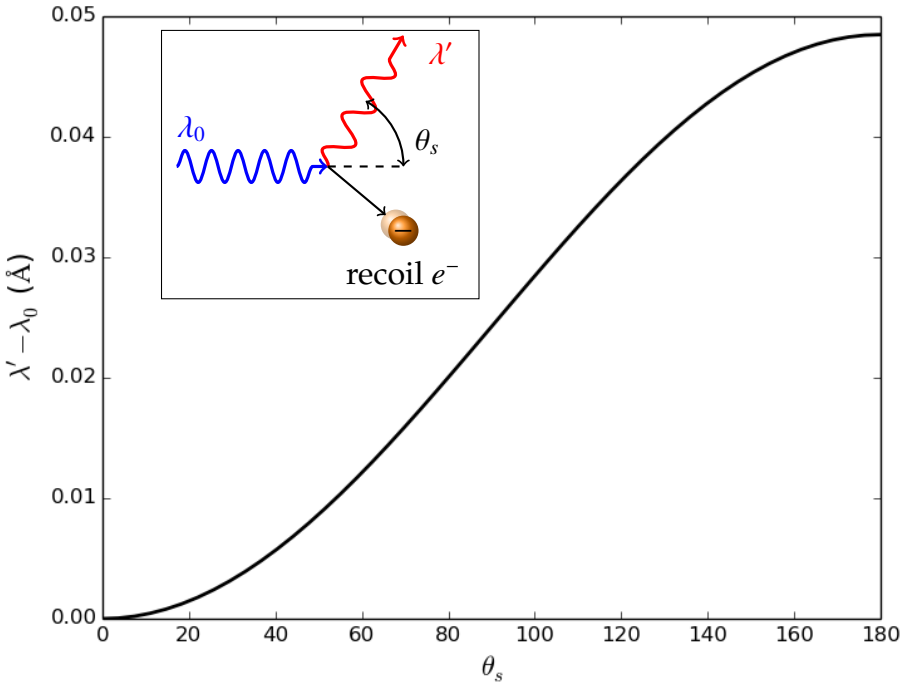

Figure 5.3: Compton shift vs. scattering angle where the scattering angle is defined by the figure shown inset.

shift in wavelength (energy) for the scattered photon is determined by geometry of the experiment, which can range from zero to twice the Compton wavelength of the electron ($\frac{h}{m_e c}$) at 180° backscattering.

Compton scattering can occur from both free electrons and weakly bound electrons in an atom, where the binding energy is less than the Compton energy ($E_b < \hbar^2 k^2 / 2m_e$). For strongly bound electrons, the mass term in Eqn. 5.12 must include the combined mass of the electron and ion which reduces the magnitude of the observed shift in scattered wavelength.

5.4 X-ray Thomson Scattering

X-ray Thomson scattering is defined as the combination of elastic scattering from strongly bound electrons and inelastic scattering from free and weakly bound electrons [100]. The scattering parameter (or α parameter) is a dimensionless quantity which indicates the probing scale length of the experiment:

$$\alpha = \frac{1}{\lambda_S k} \tag{5.13}$$

where the scattering k (see Fig. 5.4) is a function of the incident probe wave vector and the observed scattering angle given by

$$k = |\mathbf{k}| = 2k_0 sin(\theta_s/2) \tag{5.14}$$

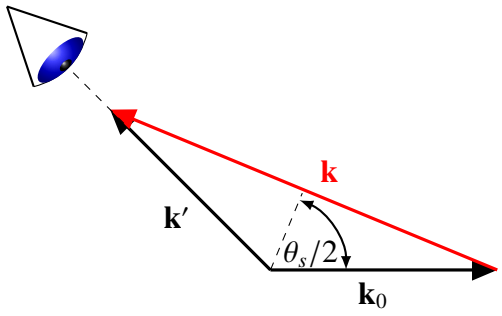

$$k = |\mathbf{k}' - \mathbf{k}_0| = 2k_0 sin(\theta_s/2)$$

Figure 5.4: Scattering vector diagram definition. The scattering vector $\mathbf{k}$ (red arrow) is the vector sum of the observed scattering vector $\mathbf{k}'$ and the initial probe vector $\mathbf{k}_0$.

The characteristic shielding length λ_s is determined by the conditions of the plasma being probed:

$$\lambda_S = \begin{cases} \lambda_D = \left(\frac{n_e q^2}{\epsilon_0 k_B T_e}\right)^{-1/2}, & \text{classical plasma} \\ \lambda_{TF} = \left(\frac{m_e q^2}{\pi \epsilon_0 \hbar^2}\left(\frac{3n_e}{\pi}\right)^{1/3}\right)^{-1/2}, & \text{degenerate plasma} \end{cases} \tag{5.15}$$

where λ_D is the Debye shielding length and λ_{TF} is the Thomas-Fermi shielding length for a Fermi-degenerate system (see App. A).

5.4.1 Noncollective Scattering Regime

When the shielding length in the plasma is shorter than the scattering length ($\approx k^{-1}$), the α parameter is smaller than one, and the scattering is described as *noncollective*. In this regime, the motion of the individual electrons are probed in the direction of $\mathbf{k}$, thus allowing a direct measurement of the electron velocity distribution function. Typically, noncollective XRTS experiments are characterized by large probe energies and backscattering angles greater than 90°.

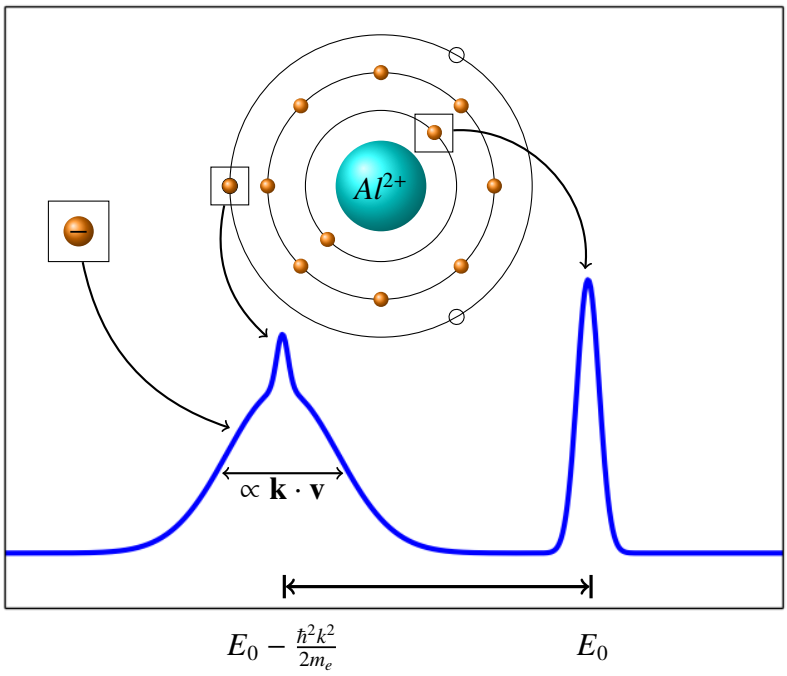

Figure 5.5: Noncollective scattering example plot.

An idealized, theoretical noncollective scattering spectrum is shown in Fig. 5.5. The initial probe energy at E_0 is downshifted and broadened by a combination of the Compton and Doppler effects

$$\hbar\omega = \frac{\hbar^2 k^2}{2m_e} \pm \hbar\mathbf{k} \cdot \mathbf{v} \tag{5.16}$$

In the case of scattering from a classical plasma, the width of the downshifted Compton feature will be proportional to $T_e^{1/2}$, and will be the result of scattering from free electrons and weakly bound electrons ($E_b < \hbar^2 k^2/2m_e$). For a Fermi-degenerate plasma, the width will be proportional to the Fermi energy and thus $n_e^{1/3}$. The unshifted peak at E_0 is the result of scattering from tightly bound electrons ($E_b > \hbar^2 k^2/2m_e$) on the ion.

The experiments of this thesis were all performed well within the noncollective regime.

5.4.2 Collective Scattering Regime

When the shielding length in the plasma is much larger than the scattering length, the α parameter becomes larger than one, and the scattering is considered *collective*. Collective scattering experiments are characterized by weaker probe energies and are predominantly carried out in a forward scatter geometry with $\theta_s < 90°$. Scattering in this regime is distinctly different from the noncollective, with plasma waves, i.e plasmons, being the primary scattering source. Consequently, diagnostic information is obtained through the modified Bohm-Gross dispersion relation [5]:

$$\omega_{pl}^2 = \omega_p^2 + 3k^2 v_{th}^2 (1 + 0.088 n_e \Lambda_e^3) + \left(\frac{\hbar k^2}{2m_e}\right)^2 \tag{5.17}$$

where

$$\omega_p = \left(\frac{n_e q^2}{\epsilon_0 m_e}\right)^{1/2} \tag{5.18}$$

is the plasma frequency,

$$v_{th} = \left(\frac{k_B T_e}{m_e}\right)^{1/2} \tag{5.19}$$

is the thermal velocity, and

$$\Lambda_e = \frac{\hbar}{(2\pi m_e k_B T_e)^{1/2}} \tag{5.20}$$

is the thermal De Broglie wavelength for the electron [101]. For a classical, collisionless plasma, Eqn. 5.17 simplifies to the Bohm-Gross relation taught in introductory plasma physics courses:

$$w_{pl}^2 \approx \omega_p^2 + \frac{3k_B T_e}{m_e} k^2 \tag{5.21}$$

No collective XRTS experiments were attempted in the pursuit of this thesis.

5.5 The Total Dynamic Structure Factor : $S(k, \omega)$

For an XRTS experiment involving an unpolarized source such as the x-pinch, the total scattered power P' into frequency interval $d\omega$ and solid angle $d\Omega$ from a plasma of electron density n_e and thickness l is given by

$$P'\, d\omega\, d\Omega = P_0\, \frac{3}{16\pi^2}\, n_e \sigma_T l\, S(k, \omega) \left(1 - \frac{1}{2} sin^2(\theta_s)\right) d\omega\, d\Omega \tag{5.22}$$

where k is defined by Eqn. 5.14, and P_0 is the incident power [102].

$S(k, \omega)$ is the total electron dynamic structure factor (DSF), which is defined as the Fourier transform of the electron-electron density fluctuation, *i.e.* the electron-electron correlation function [8]. This term alone dictates the overall theoretical shape of the scattered signal, and it must include terms for the inelastic Compton scattering from free and weakly bound electrons and elastic scattering from the tightly bound electrons [103]. These three cases are sometimes referred to as *free-free*, *bound-free* and *bound-bound* indicating the state of the electron before and after the scattering event.

The standard form used for the total dynamic structure factor was initially derived by Chihara [104] as

$$S(k,\omega) = |f_I(k) + q(k)|^2 S_{ii}(k,\omega) + Z_f S^0_{ee}(k,\omega) + Z_b \int \tilde{S}_{ce}(k,\omega-\omega') S_s(k,\omega') d\omega' \quad (5.23)$$

The first term in Eqn 5.23 is referred to as the ion feature. It accounts for bound electrons through the ionic form factor $f_I(k)$ and free or valence electrons that participate in shielding the ion through $q(k)$ [103]. $S_{ii}(k,\omega)$ is the ion-ion density correlation function, which can be approximated as static due to the slow variation of the ion motion relative to the experiment time, *i.e.* $S_{ii}(k,\omega) \approx S_{ii}(k)\delta(\omega)$ [105]. $S_{ii}(k)$ can be significant when scattering from metals if the Laue condition (Bragg condition in momentum space) is fulfilled by k [18].

The second term in Eqn 5.23 is referred to as the electron feature and it accounts for the inelastic scattering from free electrons that are neither bound nor participating in shielding in the plasma. $S^0_{ee}(k,\omega)$ is the electron-electron density correlation function.

The last term, known as the bound-free feature, describes inelastic scattering that can occur from bound electrons. $\tilde{S}_{ce}(k,\omega)$ describes the structure of the core electrons which is modulated by the self-motion of the ions, described by $S_s(k,\omega)$. This scattering is inelastic only when the final state of the electron is *free*. This can only occur if the energy transferred to the electron is greater than the binding energy of the electron, $\hbar\omega > E_b$. The effects of continuum lowering in high density systems must also be accounted for, as this can effectively lower E_b [103]. Accurately modeling this contribution is a subject of active research, and current models such as the impulse approximation (IA) or the plane wave form factor approximation (PWFFA) can be used to describe bound-free scattering [106].

CHAPTER 6

EXPERIMENTAL RESULTS AND ANALYSIS

6.1 Introduction

The XRTS results discussed in this chapter were all obtained in the noncollective regime from "cold" aluminum using a titanium hybrid x-pinch as the probe source on the COBRA pulsed power driver. Attempts at a *direct* x-ray Thomson scattering (DXRTS) technique using cold carbon were also attempted by placing the carbon target near the x-pinch. This resulted in unexpected signals thought to be due to the presence of W in the spectrometer collimating snout (Sec. 6.4.2). These experiments were also plagued by high background levels produced from both the x-pinch and the COBRA driver itself. The weak scattering signals combined with the time-integrating nature of the image plates only served to further restrict the background radiation requirements.

To combat this, a novel experimental arrangement based on monochromatic backlighting techniques was developed. In a monochromatic (or quasi-monochromatic) backlighting setup, the focusing and bandwidth properties of a spherically-bent x-ray optic (see Ch. 3) are used to collect and focus x-rays through an imaging or absorption target thereby improving signal-to-noise ratios [49].

In a *focused* x-ray Thomson scattering (FXRTS) experiment, a spherically-bent optic is used to collect the desired probe light from the hybrid x-pinch and focus it onto a target. This is accomplished by placing the scattering target at the spectral (meridional) focal point. By placing the source far outside the

Rowland circle of the spherically-bent optic, the target, focusing and collection optics, and image plate detectors can all be positioned at a distance far removed from the intense sources of background noise that are found close to the load region. The distance from the load region also provides more opportunity for debris shielding.

6.1.1 General FXRTS Setup

The reader should reference Figs. 6.1, 6.2 and 6.3 during the following description. For the experiments on COBRA, a small spectrometer chamber ($\approx 40\ cm$ diameter) was attached to the main vacuum chamber through a 5 cm diameter vacuum flange. The FXRTS setup was arranged in this chamber with a Ge(400) optic (180 mm radius of curvature) mounted on a rotation stage approximately $82cm$ from the main chamber center acting as a focusing optic. A $125\mu m$ Ti hybrid x-pinch in the main current path provided the source of $4.75keV$ Ti He_α probe photons. At this distance, the active surface area (see Sec. 3.7) of the optic was estimated to cover a solid angle of about $10^{-6}sr$. Based on the photometric estimations from Sec. 2.6 and Sec. 1.4.6, a Ti x-pinch can produce $\gtrsim 10^{15}$ photons per steradian in He_α radiation. This leads to a reasonable number of probe photons ($\gtrsim 10^9$) focused onto the target.

In order to reflect and focus the probe x-rays, a grazing angle of $\approx 67^\circ$ was set for the collection optic by using a small helium-neon (HeNe) laser pointer. The surface of the Ge optic was sufficiently reflective to see the green laser light and initial alignment proceded as follows: The laser pointer was mounted at the location of the x-pinch and pointed at the center of the Ge optic. The optic

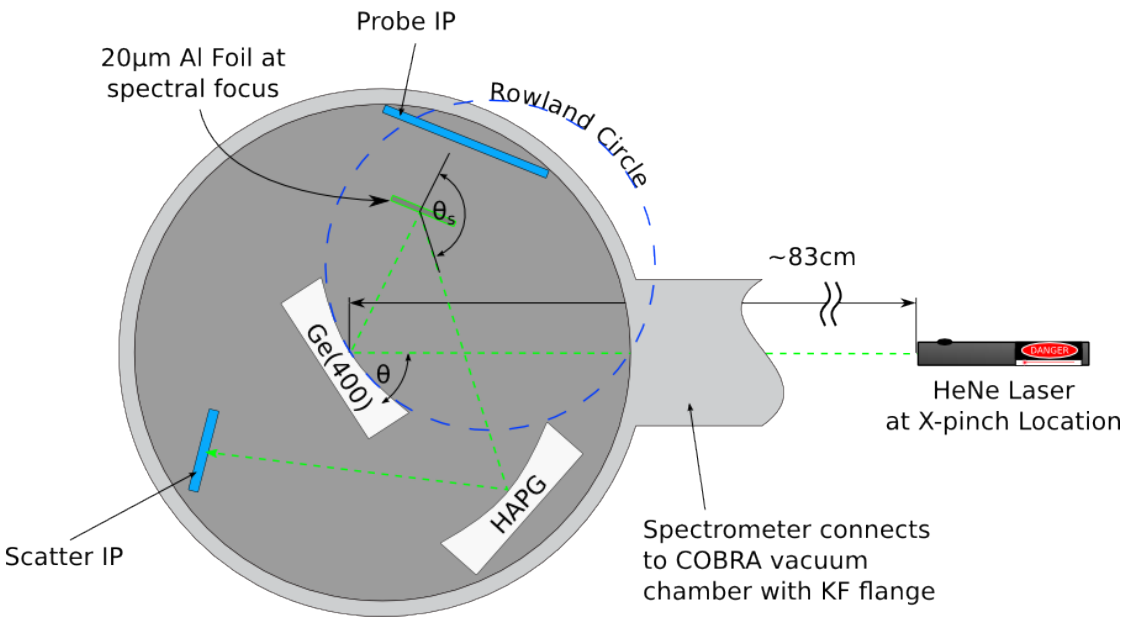

Figure 6.1: Top-down view of FXRTS alignment setup. The dashed green line indicates the path of a photon from the HeNe laser during the alignment procedure. θ_s and θ_n indicate the backscattering angle and the incident Bragg angle, respectively.

was rotated until the reflected point was aligned with the laser source. With the laser still mounted in place, a short focal length lens was mounted on the HeNe laser to cause the laser light to diverge in order to cover the entire face of the Ge optic. With a grazing angle of $\theta = 67.3°$ determined with Eqn. 3.5 for a 1^{st} order reflection of 2.61Å photons, the normal incidence angle for the Ge optic was determined as $\theta_n = 90° - \theta$.

With the Ge optic angle properly set, the Al scattering target was then placed at the spectral focal position. The thickness of the Al target was chosen to be $20\mu m$ in order to minimize the chances of secondary scattering events within the bulk of the target. The proper location of the target was determined experimentally by moving the Al target away from the Ge optic along the path of reflected laser light until the light was focused to a $\approx 2 - 3mm$ tall vertical line. The width of this line was estimated to be approximately 500 μm, due to un-

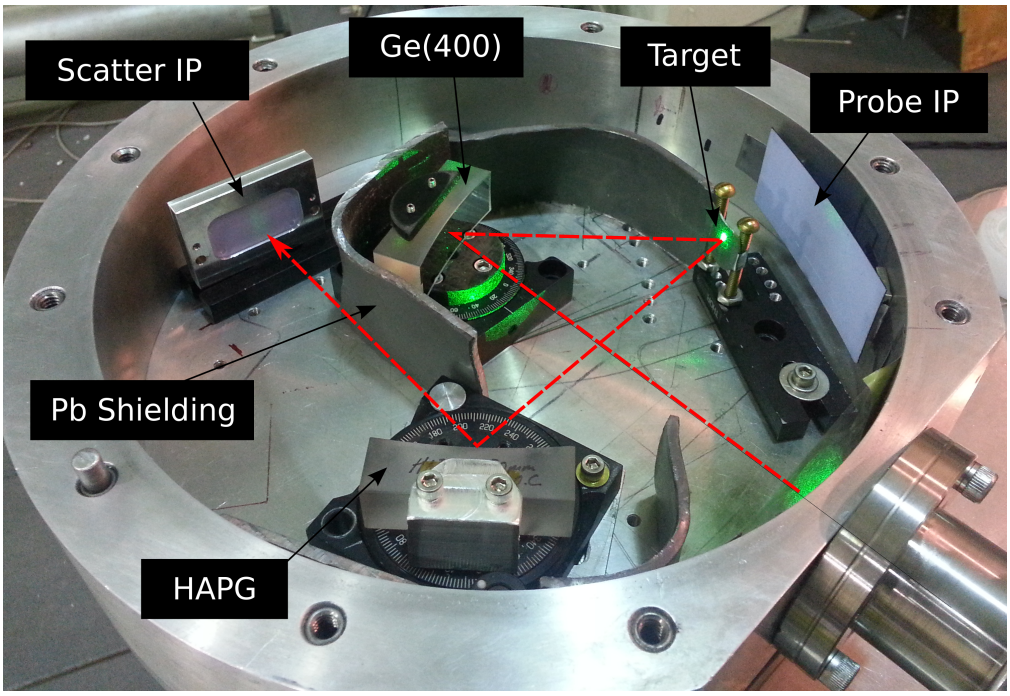

Figure 6.2: The FXRTS chamber during the initial laser alignment procedure. The red dashed line is the assumed path that a scattered photon could take during the experiment. A very dim reflection of laser light can be seen focused on the scatter IP.

certainty in the actual placement of the foil. The astigmatism associated with spherically-bent optics (discussed in the X-ray Optics chapter) is why this line is not a point as one might expect. This astigmatism is not experimentally relevant as the room-temperature Al strip is static and the temperature and density of the Al is assumed to be uniform along this focal line during the time scale of the experiment. However, this could be a problem for future experiments involving compression and/or heating of the target which may result in mixed scattering signals along this focal line if not properly spatially resolved by the collection optic.

With the Ge focusing optic and Al scattering target in proper position, the spherically-bent HAPG collection optic was then positioned and aligned approximately $12cm$ from the target at a backscattering angle θ_s between 135° –

145°, depending on the shot. This angle was measured with a large protractor to an accuracy of ±3°. The HAPG incidence angle was more difficult to zero and set due to the weak reflection of the laser light from the Al strip target, which had already been diminished by the reflection from the Ge(400) surface. The laser could not be relocated to this position due to space constraints and the fear of misaligning the target itself. The Al strip was observed to have a side which was slightly more reflective than the other, and this side was always used in the setup to help with the alignment. The initial "zeroing" and alignment proceeded in a manner identical to that previously described for the focusing optic. The HAPG optic used was employed in 2^{nd} order to satisfy both Bragg's Law and the geometric constraint of the small spectrometer chamber. To reflect the scattered light near 2.61 Å, a grazing angle of 51.2° degrees was determined and a corresponding normal incidence angle of 38.8° was applied to the rotation stage with the zero correction. A picture of the FXRTS chamber during the laser alignment procedure is shown in Fig. 6.2.

The detectors used to collect the scattered photons and the probe photons were BAS-TR uncoated IPs and BAS-SR coated IPs (see Ch. 4). The sensitivies of both types are similar near 5 keV. To collect the probe spectrum, an unfiltered SR-type IP was placed directly behind the Al target approximately $10 - 15cm$ away from the target. This provided enough distance for the focused probe photons which were not absorbed or scattered to de-focus in the spectral and vertical directions and provide a clear image of the spectrum on the IP. The HAPG mosaic optic was employed in a mosaic mode (see Sec. 3.5) with the TR-type IP was placed a distance from the HAPG equal to the distance from the HAPG to the scattering target. This IP was also unfiltered, though Pb shielding was placed strategically to keep stray light from the source from intercepting

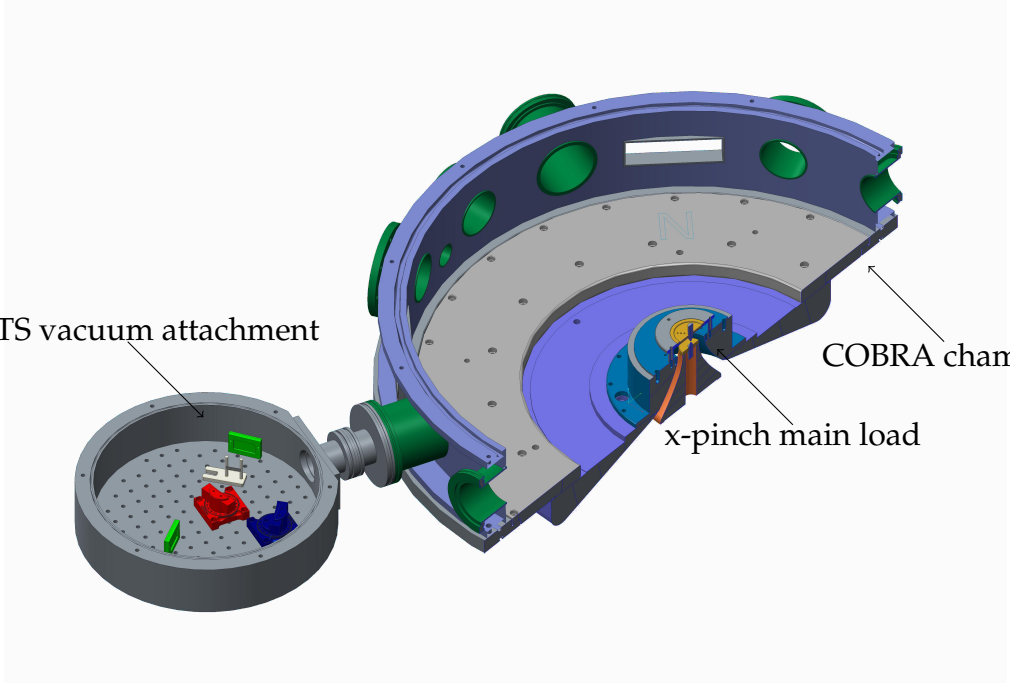

Figure 6.3: CAD model of the FXRTS setup on COBRA. The main chamber of COBRA is cut-away to show the cathode stalk.

the IP.

6.2 The Scattering Model for "Cold" Aluminum

Before the actual analysis of the experimental data, it is beneficial to discuss on a broad level how the scattering from the cold Al was modeled in SPECT3D.

As discussed in Sec. 5.5, the three contributions to an XRTS signal are from free (free-free), weakly bound (bound-free) and tightly bound electrons (bound-bound). The free and weakly bound electrons result in inelastic scattering while the tightly bound electrons result in elastic scattering. For inelastic scattering to take place, energy must be transferred to the electron. For the non-relativistic free electron case this will always occur. However, for the bound case, the

Compton energy must exceed the binding energy for inelastic scattering to occur. The first 5 ionization energies for Al are shown in Table 6.1, below [107].

Table 6.1: Ionization energies for Al.

#	**Energy (eV)**
1^{st}	5.9858
2^{nd}	18.828
3^{rd}	28.447
4^{th}	119.992
5^{th}	153.825

A single atom of Al is composed of 13 bound electrons, with 2 in the K-shell, 8 in the L-shell and 3 in the M-shell. However, for bulk Al at room temperature, the 3 M-shell electrons are considered conduction electrons (valence electrons), which are delocalized and free to move through the lattice. These 3 valence electrons are considered "free" for the purposes of the XRTS analysis using SPECT3D.

The remaining electrons in the K and L shells would appear to have higher ionization potentials than can be overcome by the Compton energy exchange, which for these experiments ranged from $78eV - 80eV$ based on the scattering angle and probe energy. It could be assumed that these remaining electrons fall in the category of tightly bound. This is not generally true, however, due to the phenomenon of *continuum lowering* or ionization potential lowering. When an atom is placed in an external electric field, the ionization potential is lowered due to the shielding of the external field. For a grouping of atoms or ions with a complicated structure where the field of one ion can influence the ionization potential of its neighbor, such as in a plasma or a metal, the problem becomes quite complicated [108]. This ionization lowering can have subtle effects on the bound-free calculations for an XRTS experiment [106]. This is an active area of

research for XRTS experiments, and a full theoretical treatment is beyond the scope of this thesis. SPECT3D provides a choice between two well known (but debated) models for continuum lowering in its bound-free calculations: Stuart and Pyatt (SP) [109] or Ecker and Kroll (EK)[110]. The user can also turn off all bound-free scattering calculations in the code if so desired. Pertaining to the XRTS simulations of this thesis, no difference was observed in the calculated $S(k,\omega)$, whether using SP, EK or none, indicating that the bound-free scattering contribution for cold Al is insignificant in the cases studied.

The calculation for the bound-bound scattering contribution from cold Al depends on the value of S_{ii} from Eqn. 5.23 and is highly dependent on the initial experimental setup. Because the Al has a lattice structure defined by reciprocal lattice vectors **G**, the Laue condition of $\mathbf{\Delta k} = \mathbf{G}$ (equivalent to the Bragg condition in a k-space derivation, see Ref. [68]) can be satisfied by the probe k-vectors as shown in Fig. 6.4. This will result in the signal being dominated by elastic scattering due to the "boost" from constructive interference by the reflection planes in the Al lattice. This fact has actually been exploited in recent XRTS experiments to observe the phase change in shocked graphite [18].

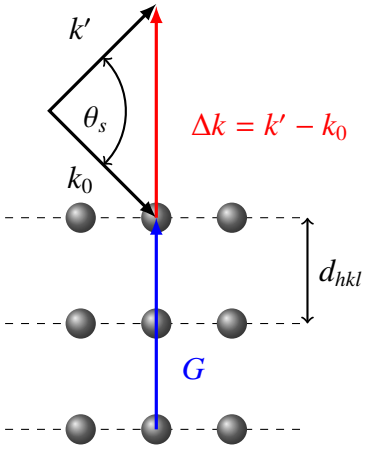

Figure 6.4: The Laue condition of $\Delta k = G$ can result in an observed increase in elastic scattering. This is identical to the Bragg Condition discussed in Ch. 3.

Determining which k-vectors satisfy the Laue condition is equivalent to finding the $S_{ii}(k)$ for Al, and this can be done in two ways.

The first method involves computing the radial distribution function (RDF) for an FCC lattice and then Fourier transforming to find the Bragg peaks in momentum space. An RDF is computed by building a 3-dimensional lattice identical to an Al face-centered cubic (FCC) lattice [111]. A lattice point close to the center of the volume is picked as a starting point. A spherical shell of radius R and thickness dr is constructed around this center point. The radius of the shell is increased in small steps where at each step the number of lattice points within R and $R + dr$ is counted and stored. This continues until the edges of the lattice are met. Counts are also built statistically by choosing multiple starting points and averaging the counts into an array. This array is then Fourier transformed to get $S_{ii}(k)$.

The second analytical method involves solving for the reciprocal lattice vectors through

$$G_{hkl} = \frac{2\pi}{a}\sqrt{h^2 + k^2 + l^2} \tag{6.1}$$

where a is the lattice constant and h, k, l must be all even or all odd, *e.g.* (111), (200), (113), etc. This method does not actually yield the entire S_{ii}, but only the location of the Bragg peaks in reciprocal space [68]. The two methods were used to compute the S_{ii} for an aluminum lattice with an $a = 4.05$Å, shown in Fig. 6.5.

SPECT3D allows the user to input values of $S_{ii}(k)$, referred to as the *ion feature* in the code. The previously calculated $S_{ii}(k)$ served as a starting point for analysis of the cold scattering results.

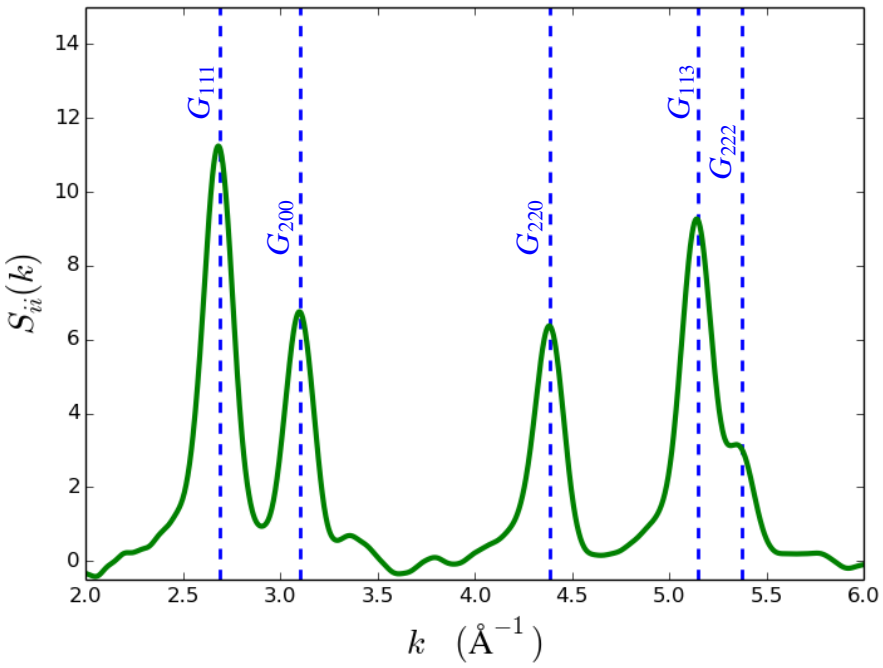

Figure 6.5: The computed Al ion-ion density correlation factor $S_{ii}(k)$ (green trace) based on the FFT of an RDF. The blue dashed vertical lines are the reciprocal lattice vectors that satisfy the Laue condition. These correspond to the location of the Bragg peaks in reciprocal space.

6.3 Cold Scattering Results

The FXRTS experiments described next were based on the previously described setup, with small changes to the backscattering angle and/or collection optic distances depending on the experiment. Once the specific COBRA experiment was carried out, the IPs were removed from the chambers with care taken not to expose the IPs to ambient light. The IPs were then scanned one at a time with a 25μm step size, sensitivity of 1000 and latitude of 5 (See Ch. 4). The images were saved in a 16-bit TIFF format for later analysis.

6.3.1 COBRA shot 2999

COBRA shot 2999 was performed at a backscattering angle of 140° ± 3° ($|k| \approx 4.52\text{Å}^{-1}$). False color images of the scattered signal and the probe spectrum are shown in Fig. 6.6 where the colorbar units are in $mPSL$ ($PSL \times 10^{-3}$).

The most intense region of the scattered signal (yellow to bright green in color)) covers an area of approximately 10^7 μm^2 on the IP with peak intensity pixel averages of ≈ 1 $mPSL/px$. Starting from here, we can work backward with order-of-magnitude estimates to arrive at a probe intensity estimate. At these energies, the IP response is $\sim 10^{-3}$ PSL/γ and the scanned pixel area is $\sim 10^3$ μm^2 indicating $\sim 10^4$ collected scattered photons. The HAPG optic collection solid angle was ~ 0.1 sr which results in $\sim 10^6$ photons scattered into 4π from the target. Based on a scattered fraction of $n_e \sigma_T l \approx 0.001$ where $n_e \sim 10^{24}$ cm^{-3} for Al, the total number of photons focused onto the target would have been $\sim 10^9$.

The focused probe area A_{foc} on the Al target is $\sim 10^6$ μm^2 which translates to a flux of $\sim 10^3$ photons/μm^2 at the target. Accounting for a geometric magnification factor of $\sim 10^{-1}$ from the spherical Ge optic and a transmission of $\sim 10\%$ through the Al foil, we arrive at an estimated photon flux on the probe IP of ~ 10 photons/μm^2. This translates to ~ 10 PSL/px. This level corresponds to a dark red color level, which is found in the strong centers of the resonance and intercombination lines in Fig. 6.6(b) (shown as *Int* and *Res*), indicating a fairly accurate estimate.

The source fluence can also be estimated based on a calculated optic throughput of $\sim 10^{-6}$ sr based on the analysis in Section 3.7. Assuming $\gtrsim 10^9$ photons were focused onto the Al target requires $\gtrsim 10^{15}$ photons/sr produced from the

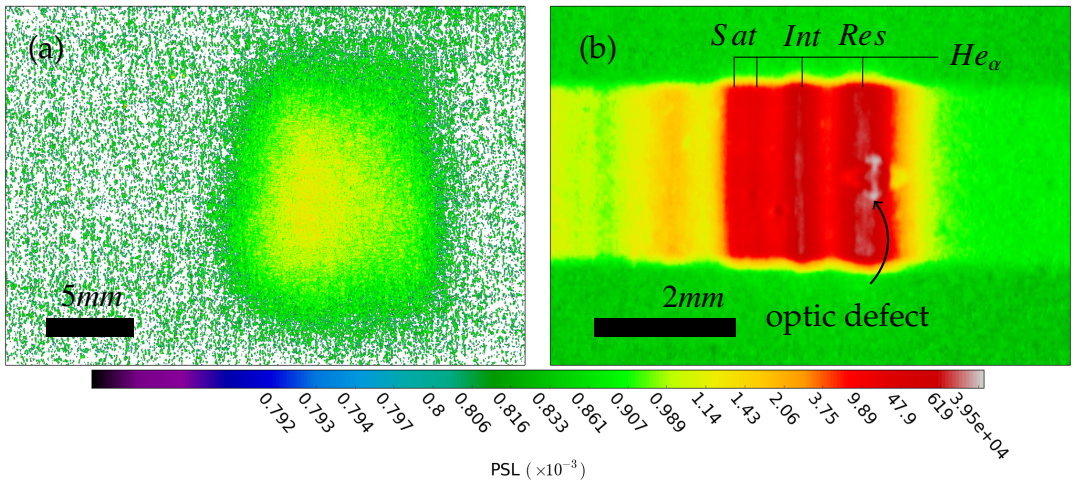

Figure 6.6: COBRA shot 2999 results: (a) The collected scattered spectrum shown in false color. (b) The Ti He_α probe spectrum for the same shot. The Ge optic has a small ovular surface defect which appears in the spectrum indicated by the arrow. Colorbar units are in $mPSL$.

x-pinch. This is in good agreement with the photon count estimates of Sec. 1.4.6 and Sec. 2.6.

SPECT3D was used to fit a theoretical scattering spectrum to an intensity profile of Fig. 6.6(a). If the reader is unfamiliar with what an intensity profile (or "lineout") involves, see App. B.2. A lineout was also taken across the collected probe spectrum of Fig. 6.6(b) and loaded into the code to function as the probe spectrum in the calculation. This lineout along with the convolved result based on a spectral resolution of 250 from the HAPG optic are shown in Fig. 6.7 to demonstrate the effect that the HAPG mosaic optic has on a collected signal. The resolution value of 250 is in close agreement with the estimated experimental resolution of the HAPG optic based on Eqn. 3.22. The limiting factor in the resolution was the source width of $\approx 500\ \mu m$ due to the uncertainty in physical placement of the Al target at the precise focal position.

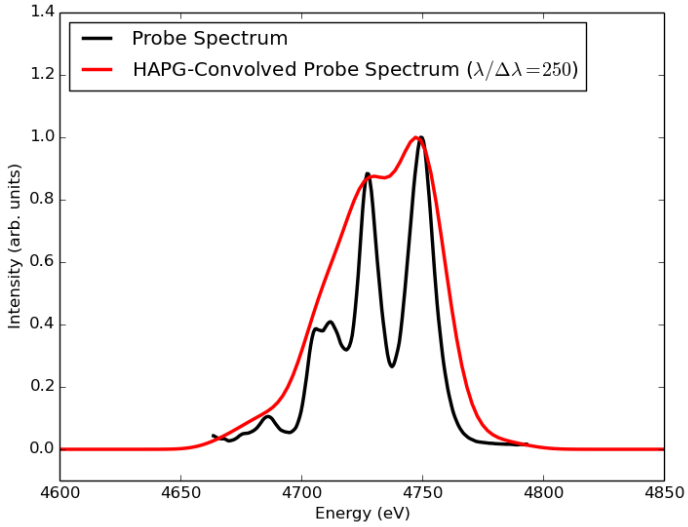

Figure 6.7: Probe spectrum lineout for COBRA shot 2999 convolved with the HAPG resolution of $\lambda/\Delta\lambda \approx 250$.

The value of $|k| \approx 4.52$ Å^{-1} from the experimental setup was compared to the computed $S_{ii}(k)$ of Fig. 6.5 to determine trial values of S_{ii} for input into SPECT3D. A plot better showing the k-vector region of interest in shown below in Fig. 6.8. The light red region in the plot centered near the vertical dashed line indicates the uncertainty in the scattering vector due to the experimental uncertainty of measuring the backscattering angle. This uncertainty translates to upper and lower limits for the value of $S_{ii}(k)$ for use in the code. Examples of the effect of different $S_{ii}(k)$ values on the total dynamic structure factor (DSF) computed by SPECT3D are shown in Fig. 6.9. As the value of S_{ii} gets larger in this plot, the scattering k-vector moves closer to the G_{220} reciprocal lattice vector resulting in an increase in elastic scattering.

An S_{ii} value of 0.8, along with a Z_f value of 3 based on the valence electrons being treated as free yielded the best fit for the scattered signal from COBRA shot 2999. This fit is shown in Fig. 6.10. The total DSF signal (shown in red)

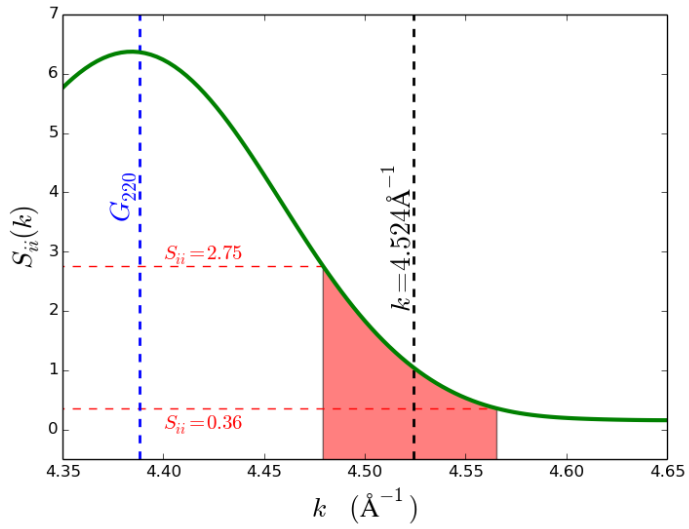

Figure 6.8: The experimental uncertainty in backscattering angle measurement translates to upper and lower estimates for S_{ii} in SPECT3D.

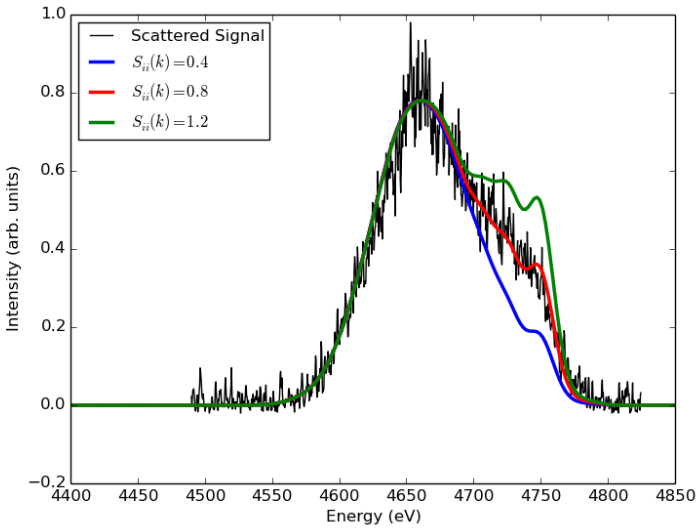

Figure 6.9: The scattered signal shown with various SPECT3D fits based on different values of $S_{ii}(k)$.

has also been broken down into its 3 contributing scattering sources: free-free (green dashed), bound-bound (solid black) and bound-free (purple solid with dots). The bound-free contribution appears to contribute negligibly in this case. Scattering from the valence electrons (free-free) appears to be the dominant scat-

tering mechanism which has been expectedly downshifted by approximately 78 eV. The intensity of the elastic scattering component from the tightly bound electrons within the Al lattice appears to be about half the signal intensity of the inelastic component from the free electrons. This is also expected based on the nearby location of the Bragg peak in k-space.

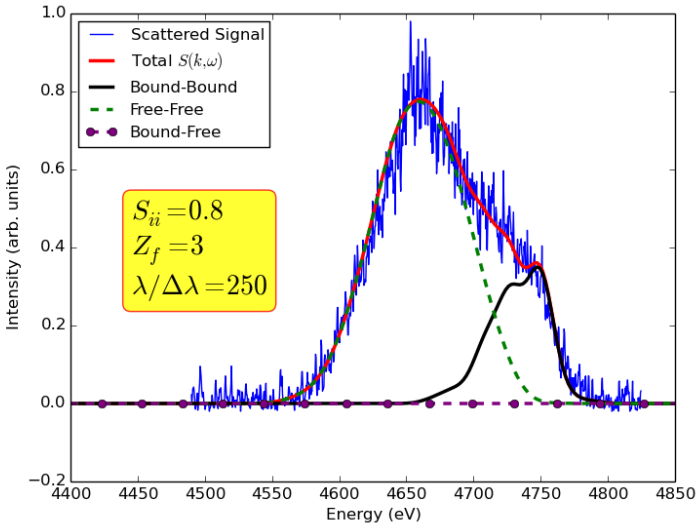

Figure 6.10: SPECT3D fit for COBRA shot 2999.

6.3.2 COBRA shot 3036

COBRA shot 3036 was performed at a backscattering angle of 145° ± 3° ($|k| \approx 4.60$ Å^{-1}). The Ge(400) optic was also turned vertically (taller than wider) in an attempt to increase the effective active surface area to reflect more photons. This was based on the assumption that Bragg diffraction occurs across the entire vertical direction of the crystal perpendicular to the direction of diffraction. This resulted in a slightly taller focal line produced at the Al target during the laser alignment procedure. The HAPG optic was also moved slightly further

away from the scattering target to a distance of 14.5 mm. To remain in a mosaic focusing mode, the scatter IP was also moved 14.5 mm away from the HAPG.

The scanned IP images of the scattered signal and the probe spectrum are shown in Fig. 6.11. Comparing Fig. 6.11(a) to Fig. 6.6(a), the most obvious difference is a much cleaner background level. While the images do have slightly different scales, the scattered signal of shot 3036 also appears to be less broadened relative to its height.

A repeat of the photon flux estimate analysis follows. The scattered signal on Fig. 6.11(a) covers an area of $\sim 10^6\ \mu m^2$ at an average PSL level of $\sim 1\ mPSL/px$ which translates to $\sim 10^3$ collected photons. The collection solid angle for the HAPG is still $\sim 0.1\ sr/4\pi$ and the scattered fraction is unchanged at $\sim 10^{-3}$ resulting in $\sim 10^8$ photons at the target. Dividing this by the focal area of $\sim 10^6\ \mu m^2$ yields a flux of $\sim$ 100 photons/μm^2. The magnification factor for this shot is $\sim 10^{-2}$ and the transmission through the 20 μm foil remains the same at $\sim 10\%$. The end result is an expected flux of $\sim 100\ mPSL/px$ at the probe IP. This estimate agrees well with the levels observed in the resonance and intercombination lines shown in Fig. 6.11(b).

Lineouts of Figs. 6.11(a) and (b) were taken as before. The probe spectrum lineout was fed into SPECT3D to model the probe source. Shown in Fig. 6.12 is the $S_{ii}(k)$ plot in the k-vector region of interest. The backscattering angle was experimentally measured to be around 145° ± 3°. The value of the scattering k-vector is indicated by the vertical dashed black line with the light red region indicating the uncertainty. This uncertainty suggests $0.16 \lesssim S_{ii} \lesssim 0.5$. It will be shown that the lower limit is in fact slightly higher than the best fit value.

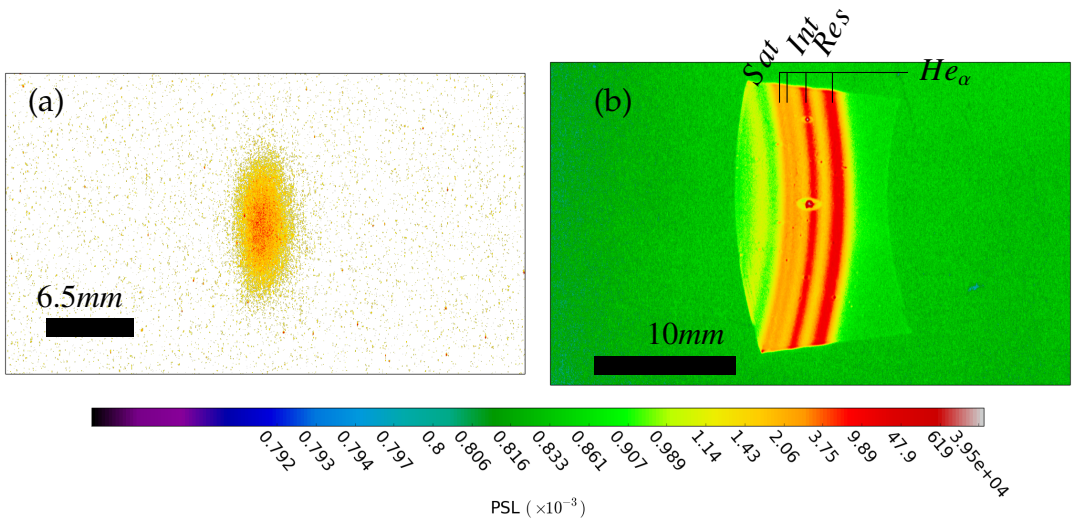

Figure 6.11: COBRA shot 3036 results: (a) The collected scattered spectrum shown in false color. (b) The Ti He_α probe spectrum for the same shot. Colorbar units are in *mPSL*.

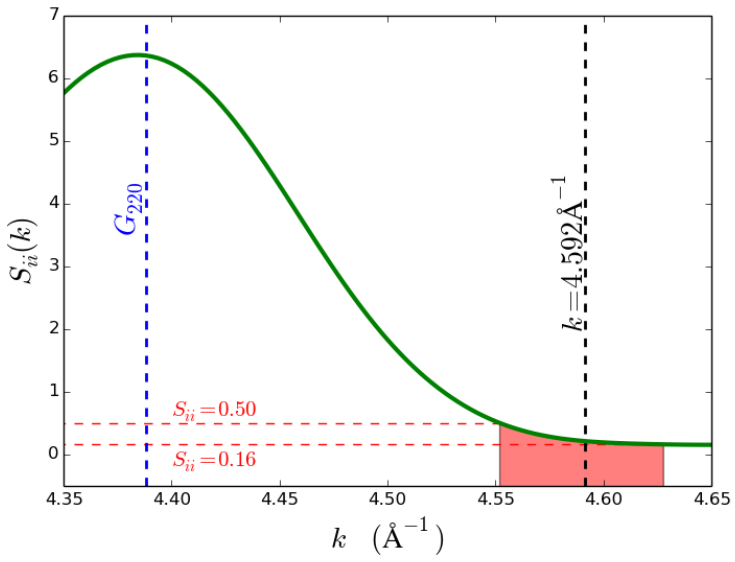

Figure 6.12: S_{ii} limits for COBRA shot 3036.

Multiple values of the total DSF were calculated based on different values for S_{ii} shown in Fig. 6.13. The best fit was determined by how well the "wing" (magnified inset in Fig. 6.13) at 4.75 *keV* was fit as this was the only region that

displayed a large disagreement between the theories. The lower limit value of 0.16 does appear to just dip into the noise of the wing. However, a value of 0.1 provides a better fit through the noise. Obviously, this value lies outside the limits based on the computed $S_{ii}(k)$ values, which were based on the Fourier transform of the RDF described earlier. A smoothing factor was also added to the final FFT, which likely led to this small lift in the floor value of the overall $S_{ii}(k)$ plot.

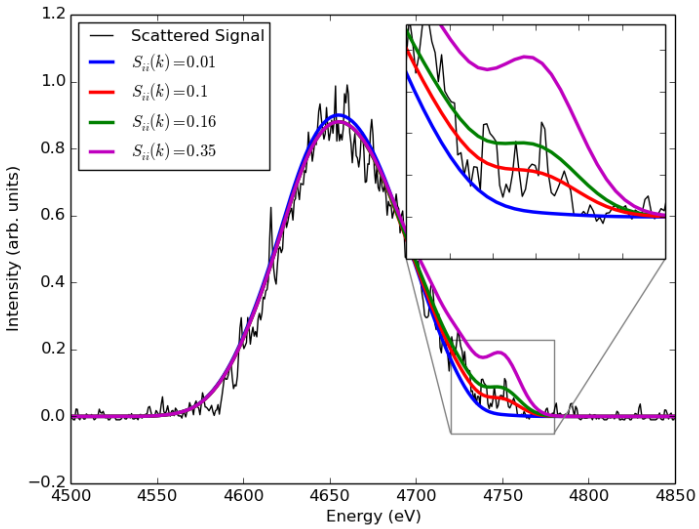

Figure 6.13: The scattered signal shown with various SPECT3D fits based on different values of $S_{ii}(k)$. The best fit was determined by how well the wing region (shown inset) was fit.

The best fit DSF (smoothed assuming $\lambda/\Delta\lambda = 250$) based on $S_{ii}(k) = 0.1$ and $Z_f = 3$ is shown with the separate components that comprise the total in Fig. 6.14. The elastic compenent from the tightly bound electrons (solid black) is overshadowed by the inelastic component from the free electrons (dashed green) which is downshifted in energy by approximately 80 eV. Slightly changing the scattering angle resulted in moving further away from the G_{220} reciprocal lattice vector in k-space and consequently destroying the elastic "boost"

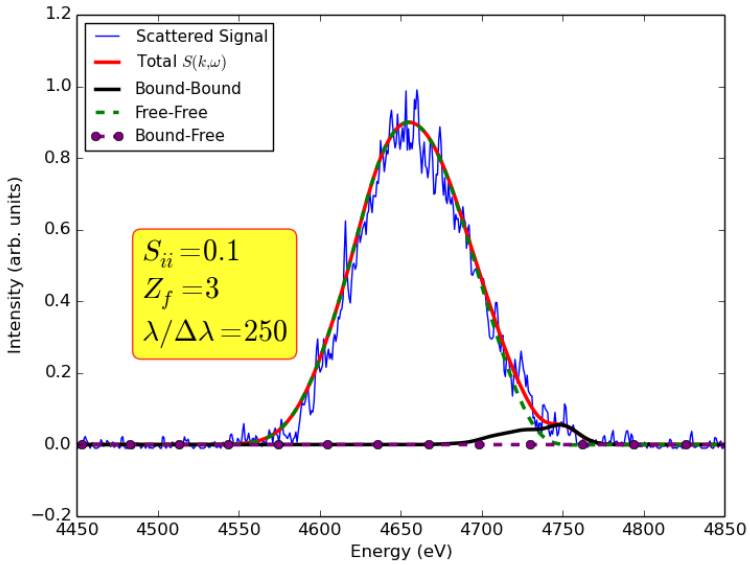

Figure 6.14: SPECT3D fit for COBRA shot 3036.

observed in shot 2999. The contribution from bound-free scattering (solid purple with dots) remains negligible.

6.4 Attempts at Direct Scattering

All attempts at direct scattering were performed on a 125 μm thick graphite (carbon) foil. This was done in the hope that the thicker target would result in a larger proportion of scattered photons based on Eqn. 1.1 while simultanously avoiding multiple scattering events.

6.4.1 Spectrometer Design

For the direct xrts (DXRTS) experiments, a new scattering spectrometer was designed and built to function inside the COBRA main chamber. This spectrometer was designed to serve or facilitate multiple purposes: mechanical alignment for the hybrid electrodes, collimation of the probe x-rays, optic protection and alignment, IP shielding, backscattering angle alignment and scattering collimation, accurate target placement, and target heating via high-voltage feedthroughs to an independentally triggered capacitor discharge bank. The full spectrometer CAD model is shown in Fig. 6.15 inside the COBRA chamber.

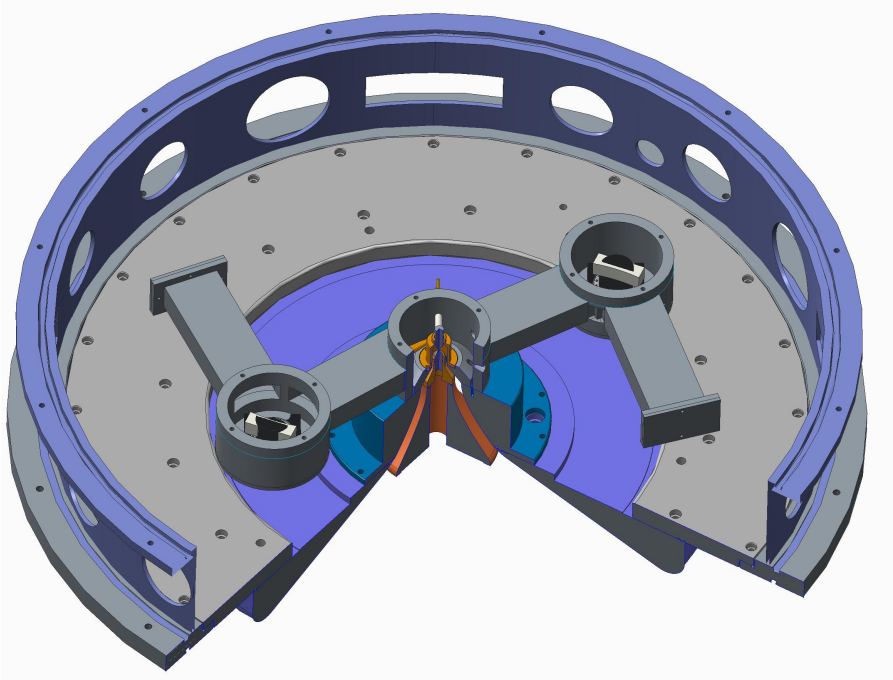

Figure 6.15: Direct XRTS experimental setup.

A simplified top-down view of the DXRTS setup with dimensions is shown in Fig. 6.16 to complement Fig. 6.15. The backscattering angle (126°) and optic normal angles (77.6°/2 = 38.8°) were rigidly set by the spectrometer design. Both spectrometers used HAPG optics functioning in the mosaic focusing mode

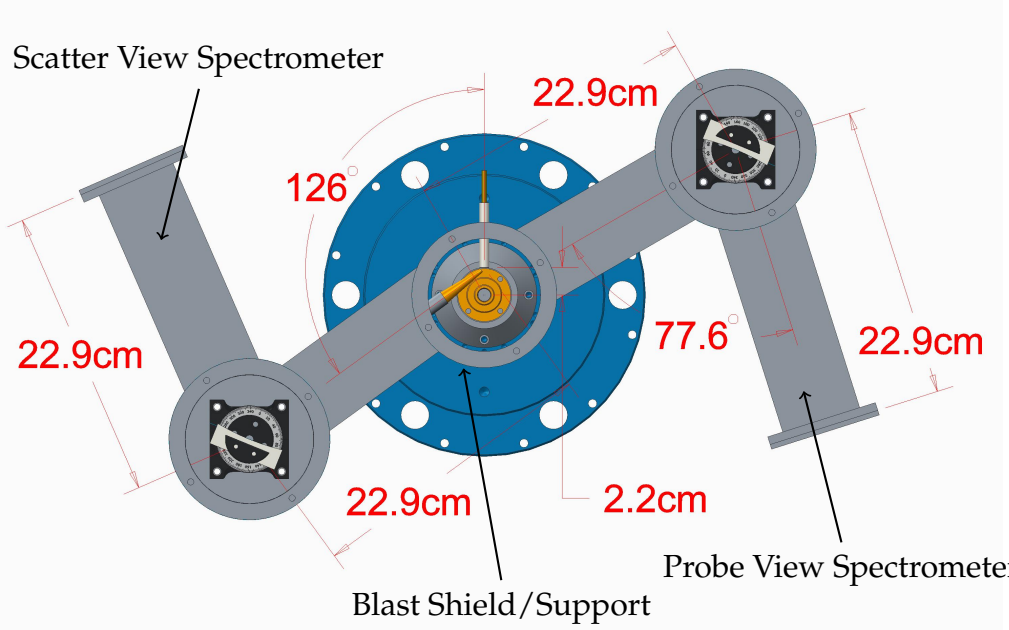

Figure 6.16: Top-down view of the DXRTS setup with angular and distance dimensions.

in a 2^{nd} order reflection. Both spectrometers also used the TR-type image plates. The scatter IP was unfiltered, and the probe IP used a 50 μm Ti filter. The spectrometers were mechanically supported in a mirrored, semi-symmetrical arrangment by a rigid 0.5in. thick cylindrical aluminum blast shield. The blast shield was bolted directly to the COBRA "top hat" segment (shown in blue) and centered concentrically about the anode-cathode (A-K) region.

Figure 6.17 should be referenced for all descriptions in the following paragraph. The DXRTS setup placed the target material, 125 μm carbon in this instance, approximately 2 cm away from the hybrid x-pinch source. The target was supported at the ends of two high-voltage (HV) electrodes which fed through the outer blast/support shield. The top electrode was insulated. The HV electrodes were meant to allow a current from a secondary independent pulser setup to heat the target. This was not attempted during these experi-

ments due to technical difficulties and time constraints. The radiation from the hybrid x-pinch was restricted by a secondary inner shield of copper-tungsten (Cu-W) which also served as the return current path for the hybrid electrodes. The pinhole in the shield acted to collimate the probe x-rays. The combined pinhole collimation and distance from the source resulted in a target *active* area of approximately 5.7 mm^2 which subtended a solid angle of $\approx 10^{-2}$ sr. Assuming $\sim 10^{15}$ photons/sr are produced from the pinch results in a fluence of $\sim 10^6$ photons/μm^2 at the target which is 3 orders of magnitude larger than the fluence from the FXRTS experiments.

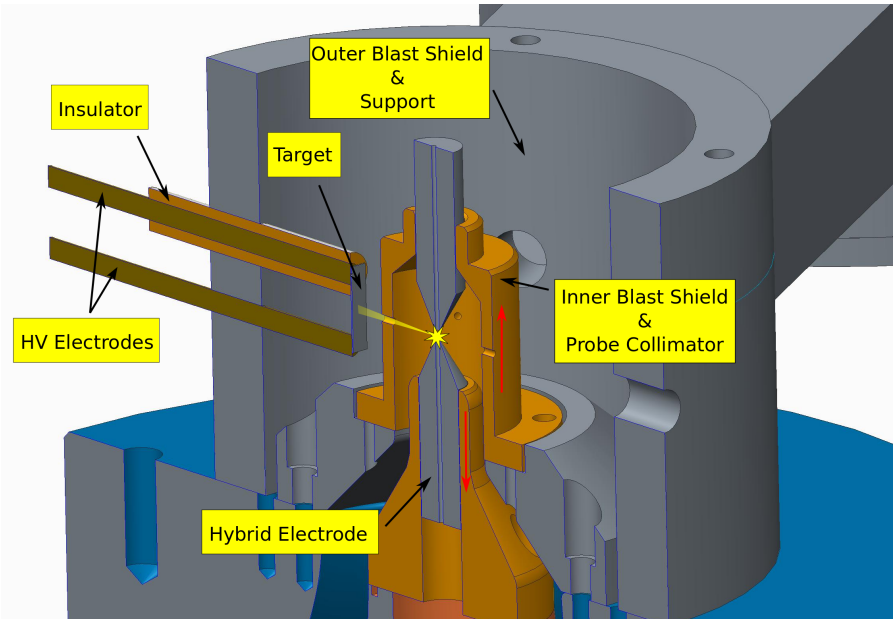

Figure 6.17: Magnified sectional view of the scattering region. The HV electrodes also functioned as the target holder. The red arrows indicate the direction of positive current flow.

The backscattered radiation from the source was observed by the scattering spectrometer at a backscattering angle of 126° through a Cu-W collimating snout with a 1 *mm* pinhole that was meant to restrict the view of the target to the active scattering region only as shown in Fig. 6.18. The tip of the snout was approximately 2 *mm* away from the active target area.

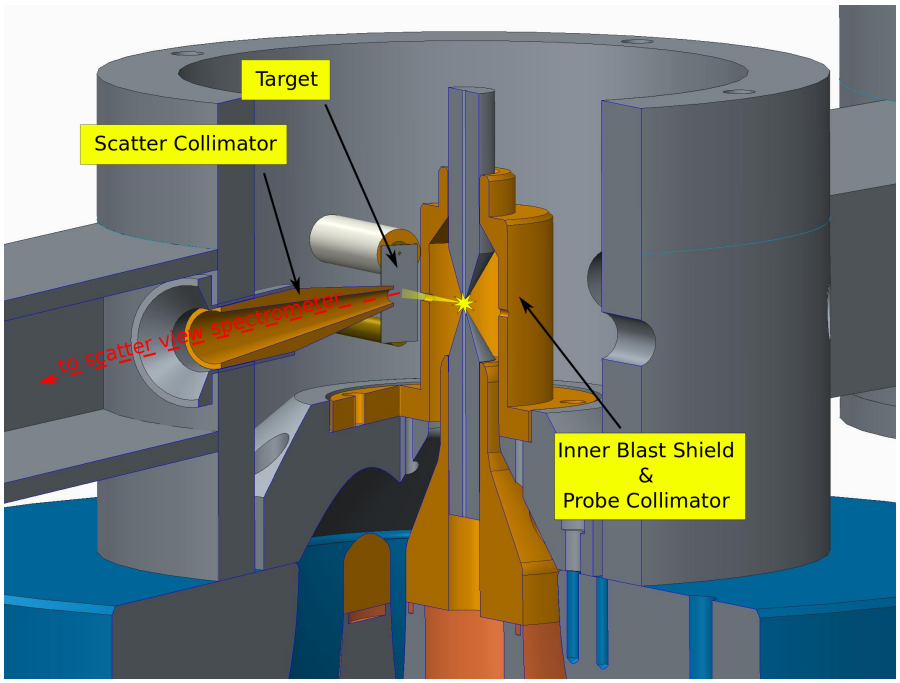

Figure 6.18: Magnified sectional view of the scattering region with scatter collimator added.

The probe view spectrometer directly observed the hybrid x-pinch probe source approximately 22.9 *cm* away as shown in Fig. 6.19.

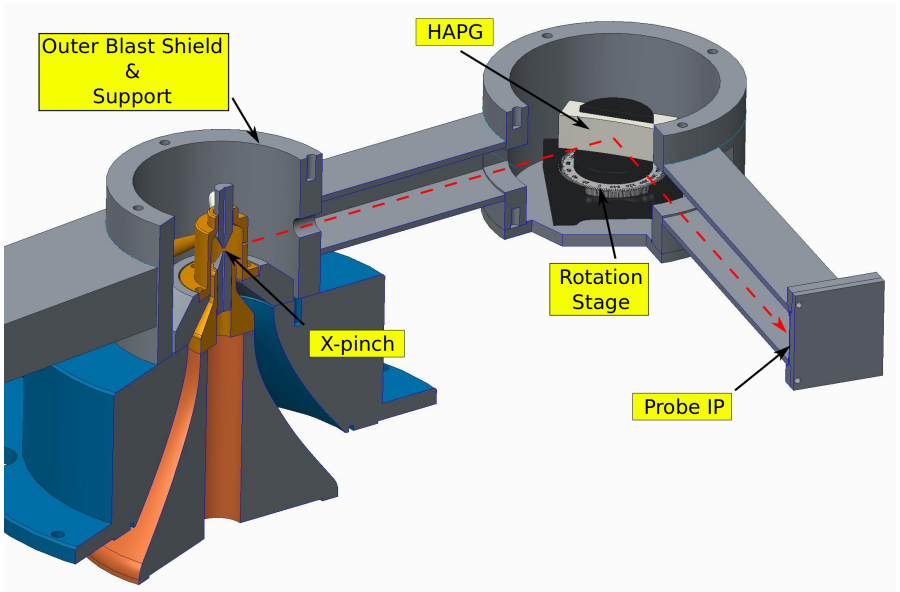

Figure 6.19: Sectional view of the probe view spectrometer arm.

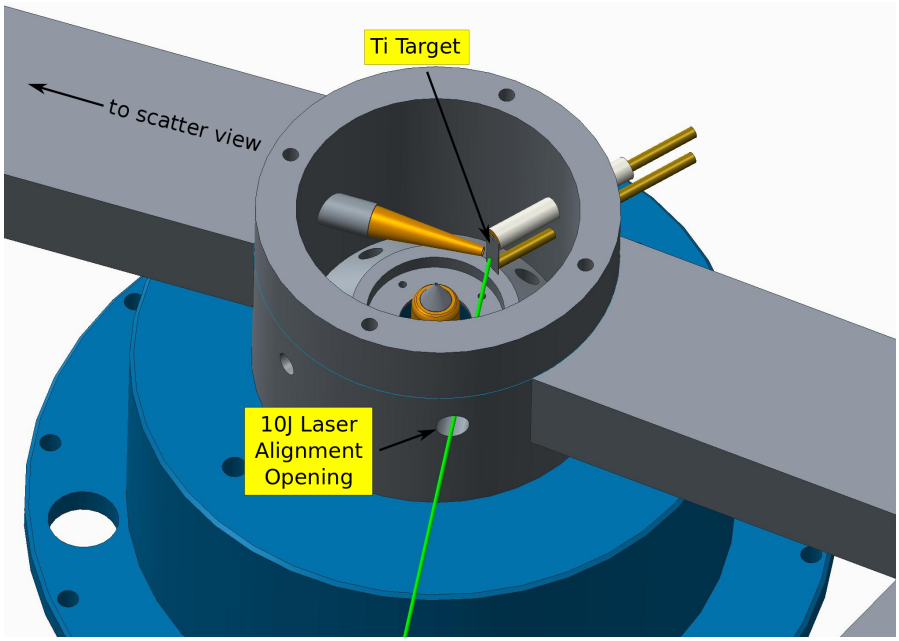

Figure 6.20: The scatter view spectrometer was aligned by using a $10J$ laser focused onto a Ti foil at the target location. The weak Ti He_α radition from the resultant plasma source was used to verify the alignment.

To align the scattering view spectrometer, a laser-produced plasma (LPP) was created at the location of the scattering target by focusing a 527 nm laser capable of producing 10 J in a 3 ns pulse onto a Ti foil. A laser alignment thru-hole was designed into the outer shield to facilitate this as shown in Fig. 6.20. The weak amounts of Ti He_α radiation created from the LPP combined with the high efficiency of the HAPG optic was expected to be sufficient for this technique.

The entire design and construction of the DXRTS setup was done as precisely as possible. The hope was that the tight tolerances built into the mechanical design would do most of the heavy lifting in terms of the optic alignment. In pursuit of this goal, the IPs used were also trimmed to precisely fit the spectrometer ends and match each other so image alignment could be simply achieved by lining up the IP edges.

6.4.2 COBRA shot 3300: DXRTS Initial Result

After the COBRA experiment was carried out, the IPs were removed from their spectrometers and scanned and recorded in a manner consistent with the FXRTS experiments. False-color images from COBRA shot 3300 are shown in Fig. 6.21. Figure 6.21(a) is the scattered spectrum and Fig. 6.21(b) is the probe spectrum. A cursory examination of the results would seem to indicate a misalignment based on the width of the scattered signal to that of the probe input signal. The collected spectrum from a Ti LPP is shown in Fig. 6.21(c). This image appears to share some of the characteristics of the collected scattered signal of Fig. 6.21(a). This is reasonable as both images were collected from the scatter view arm with identical source locations and Bragg angle settings for the HAPG optic.

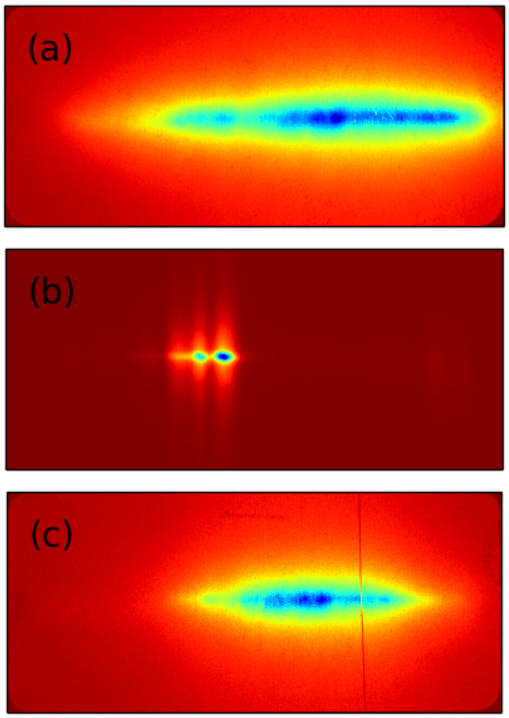

Figure 6.21: COBRA shot 3300 results: (a) Scattered spectrum from cold carbon. (b) Probe Ti He_α spectrum. (c) Spectrum collected from the laser-produced plasma (LPP) using the 10 J laser on a Ti foil.

Intensity profiles across the width of the images were taken. These energy calibrated intensity profiles are shown together in Fig. 6.22. The magnitudes of each signal have been scaled arbitrarily to best present their features. In the 4800 eV–4950 eV energy range, the Ti LPP spectrum (green trace) displays peaks that match well with the collected scattered signal from the cold carbon target (red trace). This is interesting as carbon (neutral or charged) should have no lines in this region in either 1^{st} or 2^{nd} order reflections from the HAPG optic [112]. This reflection order distinction is important as the scatter IP was unfiltered, and the HAPG was aligned to collect a 4.75 keV signal in 2^{nd} order meaning lower energies, around 2.38 keV, can also be collected in 1^{st} order.

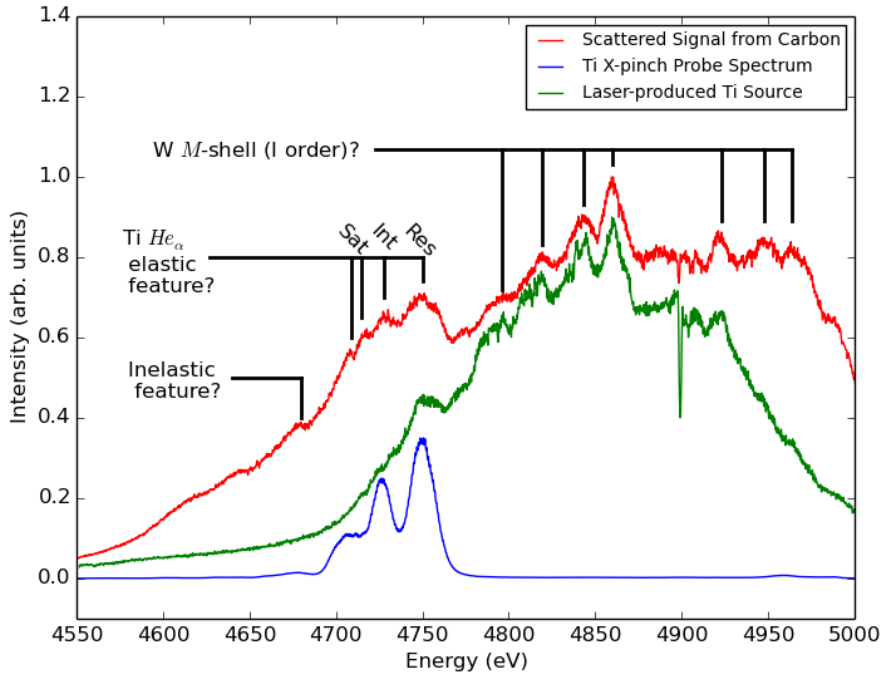

Figure 6.22: COBRA shot 3300 intensity profiles. It is suspected that the spectral features found at energies larger than 4750 eV consists of tungsten M-shell radiation reflected in 1^{st} order, due to the presence of tungsten in the collimating snout.

It is suspected that the collimating snout, which was made of an alloy con-

sisting of roughly 90% W, 6% Ni, and 4% Cu was somehow heated due to its close proximity to the target in both the alignment shot using the LPP and the actual scattering experiment. These lines are thought to be from tungsten *M*-shell transitions being reflected in 1^{st} order by the HAPG optic [112].

At lower energies, both the scattered spectrum and the Ti LPP spectrum display peaks that align well with the Ti He_α probe spectrum from the hybrid pinch (blue trace). The LPP signal displays a feature that appears to align with the resonance line of the probe spectrum near 4.75 keV. The carbon scattered spectrum also shares this feature along with features that align well with the intercombination and Li-like satellite lines. The expected Compton shift for any inelastic signal is approximately 70 eV, which agrees well with the location of a feature found near 4.68 keV indicated in Fig. 6.22. The large continuum slope that this signal is sitting on makes detailed analysis all but impossible.

The mere presence of a signal at the probe energy indicates a large elastic contribution from the tightly bound electrons in the carbon sample. This is certainly possible as the scatter k-vector value was 4.29 Å^{-1} and carbon does have reciprocal lattice vectors near 4.01 Å^{-1} and 4.68 Å^{-1}. Though the uncertainty in backscattering angle is much smaller due to mechanical tolerances in the design, the graphite foil is assumed to have a large mosaic structure which means the peaks associated with an S_{ii} function could potentially be quite broad. A single atom of carbon has 4 valence electrons. When found in a hexagonal structure as in graphite, 3 of those valence electrons participate in strong bonding with neighboring atoms, leaving 1 electron free [113]. With elastic scattering originating from 5 bound electrons and inelastic scattering originating from 1 free electron, it is not difficult to imagine that a small value of $S_{ii}(k)$ could dramati-

cally increase the relative intensity of the elastic signal to that of the inelastic.

CHAPTER 7

CONCLUSIONS

The experiment and results discussed in the previous chapter should serve as a proof-of-principle for any future attempts at x-pinch based XRTS on heated or compressed materials on COBRA. To date, the only results able to be cleanly collected were from the FXRTS setup involving scattering from undriven, cold aluminum foil, though not for lack of trying.

7.1 Background Limitations

The DXRTS experiments, which were more akin to the original experiments of Glenzer in that the target was placed in close proximity to the hybrid x-pinch source, have mostly resulted in high background noise levels on the image plates rendering any scattering results unrecoverable. Even the FXRTS experiments were sometimes plagued by high levels of background radiation. However, the IP detectors were most susceptible to background noise inside the main COBRA chamber, where electron-beam-induced x-rays from insulator stack breakdown in the COBRA adder region and/or from x-pinch gap formation were more difficult to shield.

A TR-type IP, which was functioning as the scatter IP on one such experiment, is shown in Fig. 7.1(a). This particular IP had no direct view of the x-pinch and was shielded on all sides by multiple layers of 250 μm thick Pb tape. The PSL levels across the entire IP appear to be quite uniform, with a slight gradient moving from left to right. A histogram was computed based on the levels inside

the region indicated by the black outline. The result is plotted in Fig. 7.1(b). The histogram shows a peak near 2 $mPSL$. The reader should recall from Sec. 6.3 that the average scattered signal intensity was ~ 1 $mPSL$ (about 6000 16-bit grayscale level) with background levels around 0.8 $mPSL$ (about 70 16-bit grayscale level).

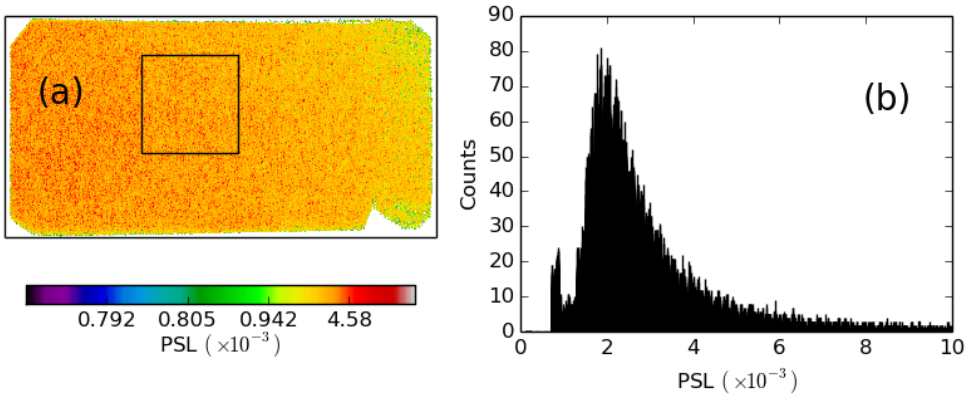

Figure 7.1: Background level analysis: (a) An IP displaying a fairly uniform and high-level background. (b) A histogram computed based on the pixels inside the black square.

It was found during the course of the experiments that the background intensity levels could be partially lowered by a careful cleaning of the insulator rings inside the COBRA vacuum adder region. During each shot, impurities are coated onto every surface inside the vacuum region. If enough of these impurities build up on the surface of an insulator that typically holds off voltages of order 100 kV, breakdowns will eventually occur which will produce Brehmsstrahlung radiation that can permeate many layers of shielding, depending on the thickness and material.

7.2 X-pinch Uncertainty

The x-pinch is a highly empirical device, prone to multiple pinches and, in the case of the hybrid x-pinch, sometimes explosively damaging to nearby optics and/or detectors. Hybrid x-pinch reproducibility has also been observed to be slightly worse than that of standard 2-wire and nested x-pinches [58]. The major selling point is their ease of setup.

In Fig. 7.2, two different COBRA shots are compared that utilized a 140 μm Ti hybrid x-pinch as the main load. Both x-pinches used gap setting of 2 mm between the hybrid electrodes. The load current for 3303 appears to have a slightly faster rise time, peaking roughly 5 ns before 3305, which could indicate a slightly lower load impedance for that case. The PCD signal for 3303 shows 3 peaks: one at 60 ns and two near 102 – 105 ns.

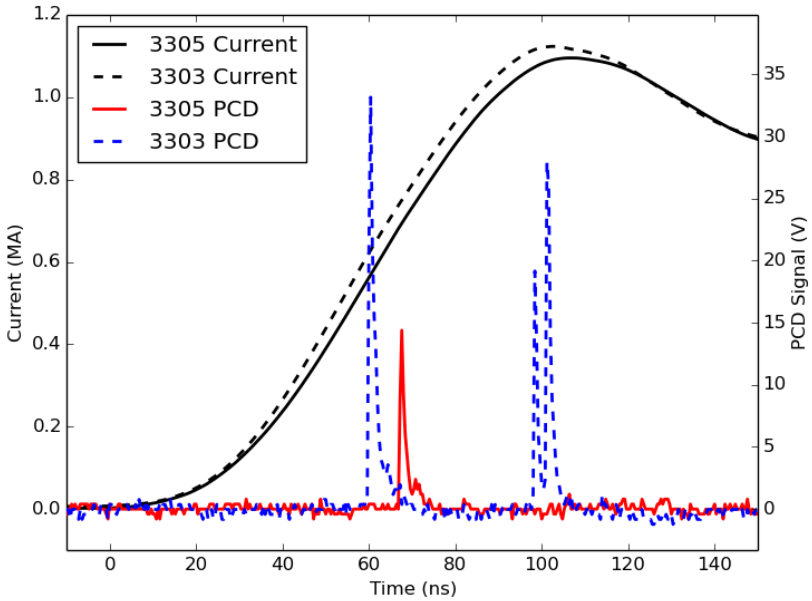

Figure 7.2: COBRA shot 3305 vs. COBRA shot 3303. Despite the initial setups being as identical as possible, the x-pinch burst results are very different.

A multiple burst x-pinch can produce problems for an XRTS experiment. Ideally, a single hotspot burst would yield the best results. Generally, an x-pinch can re-pinch after the first pinch if the linear mass of the wire is too low. However, if the linear mass is too high, the relatively large amount of "colder" material surrounding the hotspot that does not participate in the pinch could act to absorb many of the photons produced during the burst. Reference [57] provides detailed tables of linear mass and hybrid x-pinch results for experiments on both COBRA and XP.

If two or more hotspots occur in the x-pinch, temporally and spatially seperated, the experiment could suffer from the lack of time resolution and, depending on the optical setup, the lack of spatial resolution. Any overlapping scattered signals collected would be impossible to deconvolve. Gated detectors could overcome this limitation in theory, but currently the x-pinch has a large uncertainty ($\sim \pm 5\ ns$) as far as initial burst timing is concerned, which has empirically been determined to be a function of the linear mass of the wire and the rise time of the pulsed power driver [48]. The temporal uncertainty in burst timing may also affect future attempts at scattering from fast phenomena, such as shocks in a dense plasma [9].

As mentioned before in the introduction, one of the large experimental uncertainties is how well (and where) the fine wire makes contact between the electrodes. A few scenarios for wire contact through the hybrid electrodes are presented in Fig. 7.3. During each shot involving a hybrid x-pinch it was attempted to pull the fine wire taunt until the Pb weight caught at the base of the cathode and secure the free end at the anode with tape. Despite this, it is still uncertain how the wire might reposition itself (if at all) during vacuum com-

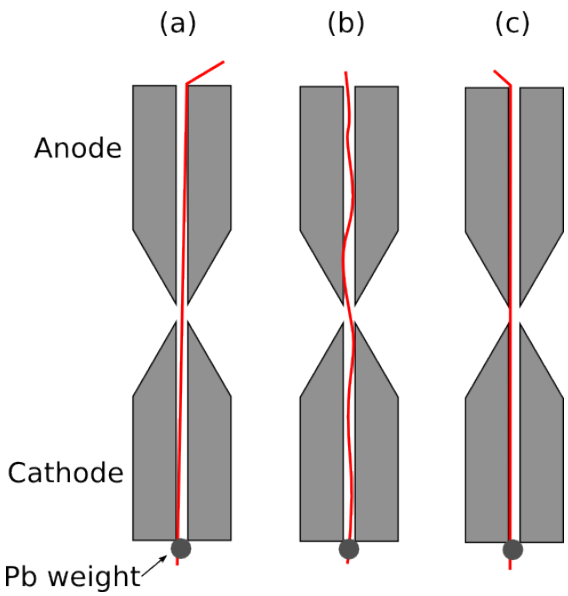

Figure 7.3: Hybrid x-pinch wire scenarios: (a) The fine wire is pulled taunt through the hybrid electrodes at a slight angle from top to bottown making contact only near the ends. (b) The wire is twisted and bent through the hybrid electrodes making electrical contact at multiple points. (c) The wire makes contact fully along a single side of each hybrid electrode.

pression of the anode-cathode gap between the hybrid electrodes, which has been estimated to be about 100 μm [114]. Figure 7.3(b) is one possibility. If a wire is making contact fully along the inside of the hybrid electrode as in Fig. 7.3(c), this could potentially lead to a lower initial inductance and faster rising current pulse similar to the current trace for COBRA shot 3303 in Fig. 7.2.

7.3 Thoughts on Direct Scattering

A direct XRTS experiment is attractive for a few reasons. First, the solid angle that the target subtends can be increased by many orders of magnitude, resulting in more probe photons delivered to the target. This, of course, leads to more scattered photons and, hopefully, more collected photons. Secondly, since the

hybrid x-pinch is driven in the main current path of COBRA, if the target were placed near the source in a direct setup, it could potentially be heated and/or compressed by including it in the return current path in series with the load. Of course this setup could negatively impact the source itself if the inductance of the target became too large and hindered current flow before the x-pinch actually pinched. An independent current driver, such as provided by a small capacitor discharge circuit capable of storing $\sim 100\ J$, can provide the highest degree of freedom with the scattering experiment as far as timing is concerned. This type of driver can still deliver enough energy to completely vaporize a thin foil target or wire, which for the 20 μm Al foil target used in the FXRTS experiments amounted to approximately 20 J.

The results discussed in Sec. 6.4.2 showed that the collimating snout used in the DXRTS setup could potentially produce line radiation and continuum that would be mixed with the scattered signal. This problem could be remedied in two ways. Obviously, filtering the IP such that only the spectra from a 2^{nd} order reflection (and higher) could be transmitted is the easiest way to eliminate some of the radiation. Moving the snout further away from the target so that it has less chance to be heated is also an option. This does open the field of view of the spectrometer slightly, so the pinhole at the end of the snout would have to be made slightly smaller to compensate.

In closing, the x-pinch is a remarkable pulsed-power x-ray source which has been applied to x-ray imaging, absorption, and now, x-ray Thomson scattering. Though only scattering results from cold targets were observed, this diagnostic does have potential for further interesting development within the pulsed power community as this diagnostic can provide information in high-density

systems where others cannot. In the author's opinion, the key to this is further development of the hybrid x-pinch source itself and the mitigation of high background levels. The kJ-class lasers currently used for XRTS experiments are unmatched in the realm of timing and reproducibility. The hybrid x-pinch may never reach this level of reproducibility, but the x-ray output-to-cost benefits are enormous in comparison.

APPENDIX A

PLASMA PARAMETER SPACE

Two important energies to consider in a plasma of electron density n_e and electron temperature T_e are the Coulomb interaction energy and the thermal or kinetic energy. The Coulomb energy per electron within a unit volume can be determined by:

$$E_c = \frac{q^2}{4\pi\epsilon_0 r_{ws}} \tag{A.1}$$

where ϵ_0 is the permittivity of free space ($\approx 8.85 \times 10^{-12}\ F/m$), q is the elementary charge ($\approx\ 1.6 \times 10^{-19}\ C$) and r_{ws} is the so called Wigner-Seitz (or ion-sphere) radius defined as:

$$r_{ws} = \left(\frac{4\pi n_e}{3}\right)^{-1/3} \tag{A.2}$$

The thermal energy of an electron with 3 degrees of freedom at temperature T_e is defined as

$$E_k = \frac{3}{2} k_B T_e \sim k_B T_e \tag{A.3}$$

with k_B being the Boltzmann constant ($\approx\ 1.38 \times 10^{-23} J/K$). The ratio of these energy values is known as the electron-electron coupling constant [115]:

$$\Gamma_{ee} = \frac{E_c}{E_k} = \frac{q^2}{4\pi\epsilon_0 k_B T_e} \frac{1}{(3/4\pi n_e)^{1/3}} \tag{A.4}$$

Knowing the value of Γ_{ee} can be helpful when attempting to simplify certain calculations and, more importantly, when determining which aspects of physics cannot be neglected in the calculation. A plasma parameter space plot is presented in Fig. A.1 with divisions determined by Γ_{ee}'s value relative to unity.

The white region where $\Gamma_{ee} << 1$ is considered the "ideal" plasma regime where the effects of Coulomb coupling can be safely ignored and thermal effects

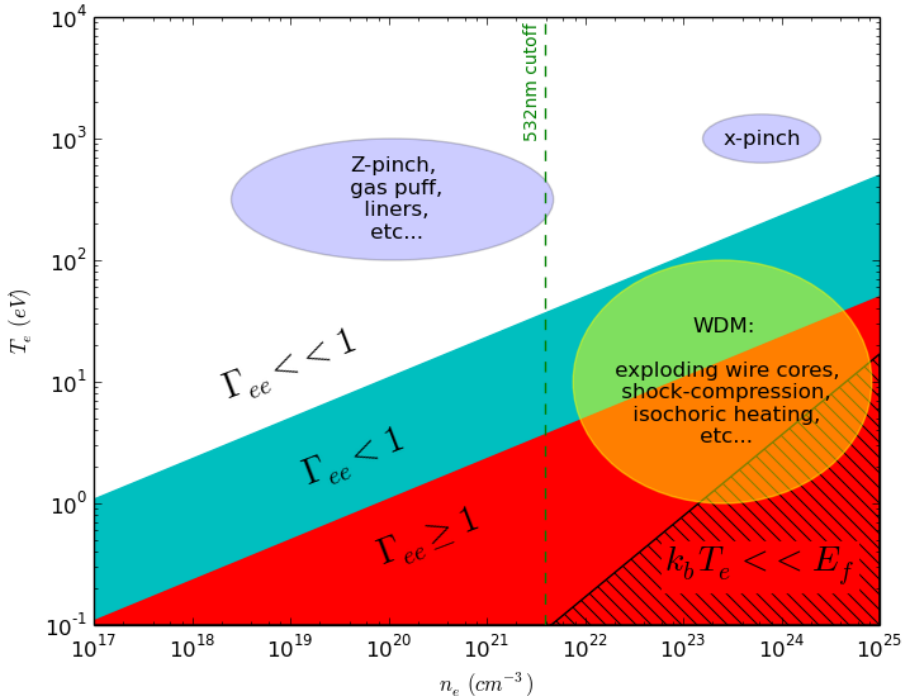

Figure A.1: Plasma parameter space.

are dominant. The majority of the plasmas created by the pulsed power drivers in LPS are within this regime during the time of interest. These include imploding z-pinch plasmas and gas puff work [20, 116]. Plasmas in the blue region ($\Gamma_{ee} < 1$) are considered *weakly coupled*. Plasmas with parameters falling in the red region ($\Gamma_{ee} \geq 1$) are considered *strongly coupled* or *non-ideal*. Here, the effects of Coulomb collisions dominate the plasma dynamics [117].

The hatched area in Fig. A.1 indicates Fermi-degenerate matter, where quantum mechanical effects play a strong role. Here, the value of Γ_{ee} must be calculated by replacing the thermal energy with the Fermi energy, defined as

$$E_f = \frac{\hbar^2 (3\pi^2 n_e)^{2/3}}{2m_e} \tag{A.5}$$

The conduction electrons within a metal lattice are an example of a strongly coupled, Fermi-degenerate system. An important aspect of a Fermi-degenerate system is that the electron velocity distribution will not follow a "classical" Maxwell-Boltzmann distribution whose width is determined by temperature, but by a Fermi-Dirac distribution whose width is determined by density [68].

Warm dense matter (WDM) is a relatively ill-defined material state with densities ranging from $0.01 - 100.0\ g/cm^3$ and temperatures from $0.1 - 100\ eV$, indicated by the yellow ellipse in Fig. A.1. In general, this describes a material that is too hot to be described by solid-state physics where the average electron temperature is of order $0.01\ eV$ and the density is too high to ignore Coulomb effects or, in degenerate cases, quantum mechanical effects [118]. An example of a pulsed power produced WDM plasma is the cold core of a current driven exploding wire [53].

APPENDIX B

SPECT3D MODELING

The cold scattering results collected were analyzed using SPECT3D. SPECT3D works by computing the scattered radiation incident on a detector by solving the radiation transfer equation along a number of lines of sight (LOS) through a plasma grid target based on the impinging radiation from an x-ray source [95]. The density and temperature target grid can be time-varying or static. The scattering cross section is computed at each grid based on the local conditions and then accounted for in the radiation transfer.

B.1 Target

A subprogram called *Plasma Grid Generator* included with SPECT3D was used to create a 1D planar (slab) representation of the Al target for use in the XRTS code, shown in Fig. B.1. The target was initialized at a thickness of $20\mu m$ containing 25 grid points of a uniform temperature of $25meV$ $(293K)$ and uniform density of $2.7g/cm^2$. This program also allows multi-dimensional targets with mutliple distributions of temperature and density to be created, though this was not needed for the analysis of the cold scattering results.

B.2 Source

The probe source spectrum can be modeled a number of ways using SPECT3D. The simplest method is to use a preprogrammed Gaussian or Lorenztian wave-

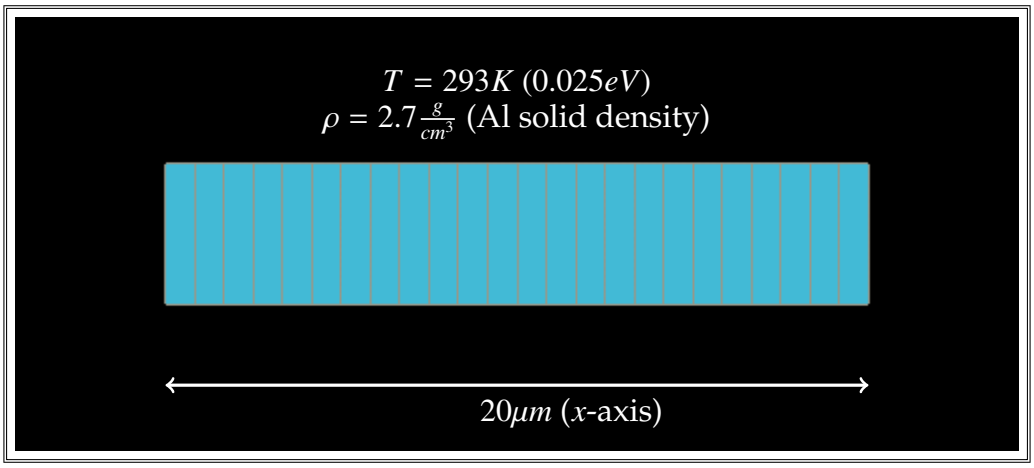

Figure B.1: Simulation grid for 20μm Al foil created with Plasma Grid Generator in SPECT3D.

form which can be modified by changing the FWHM and the intensity. The more accurate method is to use the table input method which reads in a .dat or .txt file containing the values of the experimental waveform. This was the preferred method as the probe spectrum was collected on each shot. The probe waveforms were obtained directly by taking an intensity profile (or "lineout") (a 1-D reading of position and intensity) along the dispersive direction of the IP which collected the probe spectrum for each shot. The x-position values were then converted to the known energy values of the Ti He_α spectrum and fed into the table. An example of a lineout is shown in Fig. B.2.

B.3 Scattering Angles

Backscattering angles are set within the SPECT3D program by relative positioning of the detector and the source which can be independently positioned by the user, with the assumption that the target is centered at $(0, 0, 0)$. For these simulations, the source was placed on the x-axis at a position of $0.01cm$ away

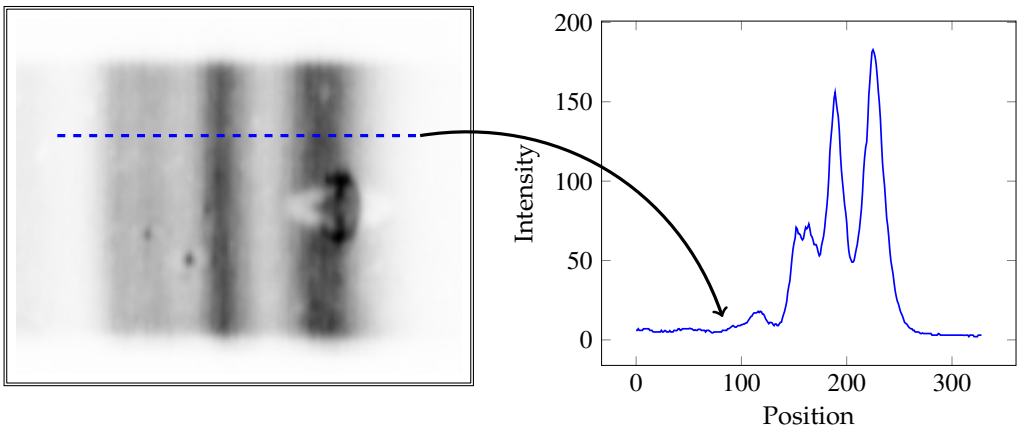

Figure B.2: An example of an intensity profile ("lineout"). The grayscale intensity values along the blue dashed line are plotted against their position values.

from the target. The detector was positioned $4cm$ away along the z-axis. The backscattering angle was set for each simulation by shifting the detector along the positive x-axis a given amount until the proper angle was reached. The target has finite dimension ($20\mu m$) along the x-axis and considered infinite in the y and z planes. The infinite dimensions are limited by computational bounds set by the user, *e.g.* $-200\mu m \leq y \leq 200\mu m$. The bounds can be further restricted in the simulation by adding apertures.

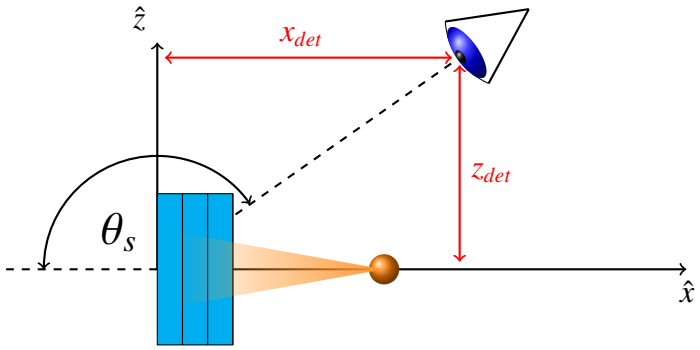

Figure B.3: SPECT3D scattering geometry example. The source (orange ball) is placed on the x-axis. The scattering angle is set by the x_{det} and z_{det} placement of the detector which always faces $(0, 0)$. The target (blue) is shown with 3 grid regions. The target is scaled for clarity.

BIBLIOGRAPHY

[1] O. Landen, S. Glenzer, M. Edwards, R. Lee, G. Collins, R. Cauble, W. Hsing, and B. Hammel, "Dense matter characterization by X-ray Thomson scattering," *J. Quant. Spectrosc. Radiat. Transf.*, vol. 71, pp. 465–478, Oct. 2001.

[2] S. H. Glenzer, G. Gregori, R. W. Lee, F. J. Rogers, S. W. Pollaine, and O. L. Landen, "Demonstration of Spectrally Resolved X-Ray Scattering in Dense Plasmas," *Phys. Rev. Lett.*, vol. 90, pp. 17–20, May 2003.

[3] J. M. Soures, R. L. McCrory, C. P. Verdon, A. Babushkin, R. E. Bahr, T. R. Boehly, R. Boni, D. K. Bradley, D. L. Brown, R. S. Craxton, J. A. Delettrez, W. R. Donaldson, R. Epstein, P. A. Jaanimagi, S. D. Jacobs, K. Kearney, R. L. Keck, J. H. Kelly, T. J. Kessler, R. L. Kremens, J. P. Knauer, S. A. Kumpan, S. A. Letzring, D. J. Lonobile, S. J. Loucks, L. D. Lund, F. J. Marshall, P. W. McKenty, D. D. Meyerhofer, S. F. B. Morse, A. Okishev, S. Papernov, G. Pien, W. Seka, R. Short, M. J. Shoup, M. Skeldon, S. Skupsky, A. W. Schmid, D. J. Smith, S. Swales, M. Wittman, and B. Yaakobi, "Direct-drive laser-fusion experiments with the OMEGA, 60-beam, >40 kJ, ultraviolet laser system," *Phys. Plasmas*, vol. 3, no. 5, p. 2108, 1996.

[4] D. Riley, R. Keenan, S. J. Topping, F. Y. Khattak, A. Mcevoy, J. J. Angulo, M. J. Lamb, C. L. S. Lewis, D. Neely, and M. Notley, "Potential for Thomson Scatter With an X-Ray Laser," *IEEE Trans. Plasma Sci.*, vol. 31, no. 5, pp. 1016–1022, 2003.

[5] A. Höll, T. Bornath, L. Cao, T. Döppner, S. Düsterer, E. Förster, C. Fortmann, S. Glenzer, G. Gregori, T. Laarmann, K.-H. Meiwes-Broer, A. Przystawik, P. Radcliffe, R. Redmer, H. Reinholz, G. Röpke, R. Thiele, J. Tiggesbäumker, S. Toleikis, N. Truong, T. Tschentscher, I. Uschmann, and U. Zastrau, "Thomson scattering from near-solid density plasmas using soft X-ray free electron lasers," *High Energy Density Phys.*, vol. 3, pp. 120–130, May 2007.

[6] M. Altarelli, "The European X-ray free-electron laser facility in Hamburg," *Nucl. Instruments Methods Phys. Res. Sect. B Beam Interact. with Mater. Atoms*, vol. 269, pp. 2845–2849, Dec. 2011.

[7] R. R. Fäustlin, T. Bornath, T. Döppner, S. Düsterer, E. Förster, C. Fortmann, S. H. Glenzer, S. Göde, G. Gregori, R. Irsig, T. Laarmann, H. J. Lee, B. Li, K.-H. Meiwes-Broer, J. Mithen, B. Nagler, A. Przystawik, H. Redlin,

R. Redmer, H. Reinholz, G. Röpke, F. Tavella, R. Thiele, J. Tiggesbäumker, S. Toleikis, I. Uschmann, S. M. Vinko, T. Whitcher, U. Zastrau, B. Ziaja, and T. Tschentscher, "Observation of Ultrafast Nonequilibrium Collective Dynamics in Warm Dense Hydrogen," *Phys. Rev. Lett.*, vol. 104, p. 125002, Mar. 2010.

[8] S. Glenzer and R. Redmer, "X-ray Thomson scattering in high energy density plasmas," *Rev. Mod. Phys.*, vol. 81, pp. 1625–1663, Dec. 2009.

[9] S. P. Regan, K. Falk, G. Gregori, P. B. Radha, S. X. Hu, T. R. Boehly, B. J. B. Crowley, S. H. Glenzer, O. L. Landen, D. O. Gericke, T. Döppner, D. D. Meyerhofer, C. D. Murphy, T. C. Sangster, and J. Vorberger, "Inelastic X-Ray Scattering from Shocked Liquid Deuterium," *Phys. Rev. Lett.*, vol. 109, p. 265003, Dec. 2012.

[10] A. L. Kritcher, P. Neumayer, J. Castor, T. Döppner, R. W. Falcone, O. L. Landen, H. J. Lee, R. W. Lee, E. C. Morse, A. Ng, S. Pollaine, D. Price, and S. H. Glenzer, "Ultrafast x-ray Thomson scattering of shock-compressed matter.," *Science*, vol. 322, pp. 69–71, Oct. 2008.

[11] C. Fortmann, H. J. Lee, T. Döppner, R. W. Falcone, A. L. Kritcher, O. L. Landen, C. Niemann, and S. H. Glenzer, "Adiabatic Index in Shock-Compressed Beryllium," *Contrib. to Plasma Phys.*, vol. 52, no. 3, pp. 186–193, 2012.

[12] T. Döppner, C. Fortmann, P. Davis, A. Kritcher, O. Landen, H. Lee, R. Redmer, S. Regan, and S. Glenzer, "X-ray Thomson scattering for measuring dense beryllium plasma collisionality," tech. rep., Lawrence Livermore National Laboratory, 2009.

[13] T. A. Shelkovenko, D. B. Sinars, S. A. Pikuz, and D. A. Hammer, "Radiographic and spectroscopic studies of X-pinch plasma implosion dynamics and x-ray burst emission characteristics," *Phys. Plasmas*, vol. 8, no. 4, p. 1305, 2001.

[14] D. L. Matthews, E. M. Campbell, N. M. Ceglio, G. Hermes, R. Kauffman, L. Koppel, R. Lee, K. Manes, V. Rupert, V. W. Slivinsky, R. Turner, and F. Ze, "Characterization of laser-produced plasma x-ray sources for use in x-ray radiography," *J. Appl. Phys.*, vol. 54, no. 8, p. 4260, 1983.

[15] A. Holl, R. Redmer, and G. Ropke, "X-ray Thomson scattering in dense plasmas," *Plasma Sci.*, pp. 8–17, 2007.

[16] G. Hu, X. Zhang, J. Zheng, A. Lei, B. Shen, Z. Xu, J. Zhang, J. Yang, G. Yang, M. Wei, J. Li, and Y. Ding, "Demonstration of X-ray Thomson Scattering on Shenguang-II Laser Facility," *Plasma Sci. Technol.*, vol. 14, pp. 864–870, Oct. 2012.

[17] S. H. Glenzer, G. Gregori, F. J. Rogers, D. H. Froula, S. W. Pollaine, R. S. Wallace, and O. L. Landen, "X-ray scattering from solid density plasmas," *Phys. Plasmas*, vol. 10, no. 6, p. 2433, 2003.

[18] D. Kraus, A. Otten, A. Frank, V. Bagnoud, A. Blažević, D. Gericke, G. Gregori, A. Ortner, G. Schaumann, D. Schumacher, J. Vorberger, F. Wagner, K. Wünsch, and M. Roth, "X-ray Thomson scattering on shocked graphite," *High Energy Density Phys.*, vol. 8, pp. 46–49, Mar. 2012.

[19] L. Ruggles, J. Porter, P. Rambo, W. Simpson, M. Vargas, G. Bennett, and I. Smith, "Measurements of 410 keV x-ray production with the Z-Beamlet laser," *Rev. Sci. Instrum.*, vol. 74, no. 3, 2003.

[20] R. D. McBride, T. A. Shelkovenko, S. A. Pikuz, D. A. Hammer, J. B. Greenly, B. R. Kusse, J. D. Douglass, P. F. Knapp, K. S. Bell, I. C. Blesener, and D. A. Chalenski, "Implosion dynamics and radiation characteristics of wire-array Z pinches on the Cornell Beam Research Accelerator," *Phys. Plasmas*, vol. 16, no. 1, p. 012706, 2009.

[21] T. H. Martin, *J. C. Martin on Pulsed Power*. Advances in Pulsed Power Technology, Springer US, 2013.

[22] J. B. Greenly, J. D. Douglas, D. A. Hammer, B. R. Kusse, S. C. Glidden, and H. D. Sanders, "A 1 MA, variable risetime pulse generator for high energy density plasma research.," *Rev. Sci. Instrum.*, vol. 79, p. 073501, July 2008.

[23] D. H. Kalantar, *A Experimental Study of the Dynamics of X-Pinch and Z-Pinch Plasmas*. PhD thesis, Cornell University, 1993.

[24] J. D. Huba, *NRL Formulary*. Washington, D.C.: Naval Research Laboratory, 2002.

[25] W. Rogowski and W. Steinhaus, "Die messung der magnetischen spannung," *Electr. Eng. (Archiv fur Elektrotechnik)*, vol. 1, no. 4, pp. 141–150, 1912.

[26] J. Jackson, *Classical Electrodynamics Third Edition*. Wiley, Aug. 1998.

[27] R. Spielman, "Diamond photoconducting detectors as high power zpinch diagnostics," *Rev. Sci. Instrum.*, vol. 66, no. 1, pp. 867–870, 1995.

[28] S. V. Lebedev, R. Aliaga-Rossel, S. N. Bland, J. P. Chittenden, A. E. Dangor, M. G. Haines, and I. H. Mitchell, "The dynamics of wire array Z-pinch implosions," *Phys. Plasmas*, vol. 6, no. 5, p. 2016, 1999.

[29] H.-K. Chung, M. Chen, W. Morgan, Y. Ralchenko, and R. Lee, "FLYCHK: Generalized population kinetics and spectral model for rapid spectroscopic analysis for all elements," *High Energy Density Phys.*, vol. 1, pp. 3–12, Dec. 2005.

[30] T. A. Shelkovenko, S. A. Pikuz, D. A. Hammer, D. J. Ampleford, S. N. Bland, S. C. Bott, J. P. Chittenden, and S. V. Lebedev, "Use of spherically bent crystals to diagnose wire array z pinches," *Rev. Sci. Instrum.*, vol. 75, no. 10, p. 3681, 2004.

[31] D. B. Sinars, S. A. Pikuz, T. A. Shelkovenko, K. M. Chandler, and D. A. Hammer, "Temporal parameters of the X-pinch x-ray source," *Rev. Sci. Instrum.*, vol. 72, no. 7, p. 2948, 2001.

[32] C. Stallings, K. Nielsen, and R. Schneider, "Multiple-wire array load for high-power pulsed generators," *Appl. Phys. Lett.*, vol. 29, no. 7, p. 404, 1976.

[33] M. G. Haines, "A review of the dense Z -pinch," *Plasma Phys. Control. Fusion*, vol. 53, p. 093001, Sept. 2011.

[34] N. R. Pereira and J. Davis, "X rays from z-pinches on relativistic electron-beam generators," *J. Appl. Phys.*, vol. 64, no. 3, p. R1, 1988.

[35] J. E. Bailey, G. A. Chandler, D. Cohen, M. E. Cuneo, M. E. Foord, R. F. Heeter, D. Jobe, P. W. Lake, J. J. MacFarlane, T. J. Nash, D. S. Nielson, R. Smelser, and J. Torres, "Radiation science using Z-pinch x rays," *Phys. Plasmas*, vol. 9, no. 5, p. 2186, 2002.

[36] P. M. Bellan, *Fundamentals of Plasma Physics*. Cambridge University Press, 2006.

[37] D. Ryutov, M. Derzon, and M. Matzen, "The physics of fast Z pinches," *Rev. Mod. Phys.*, vol. 72, no. 1, 1999.

[38] D. Sinars, S. Pikuz, T. Shelkovenko, K. Chandler, D. Hammer, and J. Apruzese, "Time-resolved spectroscopy of Al, Ti, and Mo X pinch radiation using an X-ray streak camera," *J. Quant. Spectrosc. Radiat. Transf.*, vol. 78, pp. 61–83, 2003.

[39] S. Pikuz, D. Sinars, T. Shelkovenko, K. Chandler, D. Hammer, I. Skobelev, and G. Ivanenkov, "Time-resolved X-ray spectroscopy of hot spots in an X-pinch," *J. Exp. Theor. Phys. Lett.*, vol. 76, no. 8, pp. 490–494, 2002.

[40] D. B. Sinars, S. A. Pikuz, J. D. Douglass, R. D. McBride, D. J. Ampleford, P. Knapp, K. Bell, D. Chalenksi, M. E. Cuneo, J. B. Greenly, D. A. Hammer, B. R. Kusse, A. Mingaleev, T. A. Shelkovenko, and D. F. Wenger, "Bright spots in 1 MA X pinches as a function of wire number and material," *Phys. Plasmas*, vol. 15, p. 092703, Sept. 2008.

[41] S. Lebedev, D. Ampleford, S. Bland, S. Bott, J. Chittenden, C. Jennings, M. Haines, J. Palmer, and J. Rapley, "Implosion dynamics of wire array Z-pinches: experiments at Imperial College," *Nucl. Fusion*, vol. 44, pp. S215–S220, Dec. 2004.

[42] C. Deeney, T. Nash, R. Prasad, L. Warren, K. Whitney, J. Thornhill, and M. Coulter, "Role of the implosion kinetic energy in determining the kilovolt x-ray emission from aluminum-wire-array implosions," *Phys. Rev. A*, vol. 44, no. 10, p. 6762, 1991.

[43] S. M. Zakharov, G. V. Ivanenkov, A. A. Kolomenskij, S. A. Pikuz, A. I. Samokhin, and I. Ulshmid, "Wire X-pinch in a high-current diode," *Pis'ma v Zhurnal Tekhnicheskoj Fiz.*, vol. 8, no. 17, pp. 1060–1063, 1982.

[44] T. A. Shelkovenko, S. A. Pikuz, D. A. Hammer, Y. S. Dimant, and A. R. Mingaleev, "Evolution of the structure of the dense plasma near the cross point in exploding wire X pinches," *Phys. Plasmas*, vol. 6, no. 7, 1999.

[45] T. A. Shelkovenko, S. A. Pikuz, B. M. Song, K. M. Chandler, M. D. Mitchell, D. A. Hammer, G. V. Ivanenkov, A. R. Mingaleev, and V. M. Romanova, "Electron-beam-generated x rays from X pinches," *Phys. Plasmas*, vol. 12, no. 3, p. 033102, 2005.

[46] I. Blesener, J. Greenly, S. Pikuz, T. Shelkovenko, S. Vishniakou, D. Hammer, and B. Kusse, "Axial x-ray backlighting of wire-array Z-pinches using X pinches," *Rev. Sci. Instrum.*, vol. 80, pp. 1–5, 2009.

[47] C. Hoyt, P. Knapp, S. Pikuz, T. Shelkovenko, P. Gourdian, J. Greenly, B. Kusse, and D. Hammer, "X-pinch radiography of exploding "cables"," *IEEE Trans. Plasma Sci.*, vol. 39, no. 11, pp. 2404–2405, 2011.

[48] J. D. Douglass, S. A. Pikuz, T. A. Shelkovenko, D. A. Hammer, S. N. Bland, S. C. Bott, and R. D. McBride, "Structure of the dense cores and ablation plasmas in the initiation phase of tungsten wire-array Z pinches," *Phys. Plasmas*, vol. 14, no. 1, p. 012704, 2007.

[49] S. A. Pikuz, T. A. Shelkovenko, V. M. Romanova, D. A. Hammer, A. Y. Faenov, V. A. Dyakin, and T. A. Pikuz, "High-luminosity monochromatic x-ray backlighting using an incoherent plasma source to study extremely dense plasmas (invited)," *Rev. Sci. Instrum.*, vol. 68, no. 1, p. 740, 1997.

[50] P. F. Knapp, J. B. Greenly, P. A. Gourdain, C. L. Hoyt, S. A. Pikuz, T. A. Shelkovenko, and D. A. Hammer, "Quasimonochromatic x-ray backlighting on the COrnell Beam Research Accelerator (COBRA) pulsed power generator," 2010.

[51] S. A. Pikuz, B. Song, T. Shelkovenko, K. Chandler, M. Mitchell, and D. Hammer, "X-pinch source size measurements," *Proc. SPIE*, vol. 5196, pp. 25–35, 2004.

[52] D. Sinars, L. Gregorian, D. Hammer, and Y. Maron, "Plasma imaging and spectroscopy diagnostics developed on 100-500-ka pulsed power devices," *Proceedings of the IEEE*, vol. 92, pp. 1110–1121, July 2004.

[53] P. Knapp, S. Pikuz, T. Shelkovenko, D. Hammer, and S. Hansen, "High resolution absorption spectroscopy of exploding wire plasmas using an x-pinch x-ray source and spherically bent crystal.," *Rev. Sci. Instrum.*, vol. 82, p. 063501, June 2011.

[54] T. Shelkovenko and S. Pikuz, "Multiwire $ X $-Pinches at 1-MA Current on the COBRA Pulsed-Power Generator," *IEEE Trans. Plasma Sci.*, vol. 34, no. 5, pp. 2336–2341, 2006.

[55] T. A. Shelkovenko, S. A. Pikuz, R. D. McBride, P. F. Knapp, H. Wilhelm, D. A. Hammer, and D. B. Sinars, "Nested multilayered X pinches for generators with mega-ampere current level," *Phys. Plasmas*, vol. 16, no. 5, pp. –, 2009.

[56] I. C. Blesener, J. B. Greenly, B. R. Kusse, K. S. Blesener, C. E. Seyler, and

D. A. Hammer, "Pinching of ablation streams via magnetic field curvature in wire-array Z-pinches," *Phys. Plasmas*, vol. 19, no. 2, p. 022109, 2012.

[57] T. A. Shelkovenko, S. A. Pikuz, S. A. Mishin, A. R. Mingaleev, I. N. Tilikin, P. F. Knapp, A. D. Cahill, C. L. Hoyt, and D. A. Hammer, "Hybrid X-pinches," *Plasma Phys. Reports*, vol. 38, no. 5, pp. 359–381, 2012.

[58] T. A. Shelkovenko, S. A. Pikuz, C. L. Hoyt, A. D. Cahill, and D. A. Hammer, "Study of New Configurations of Hybrid "X" Pinches," *Plasma Sci. IEEE Trans.*, vol. 42, no. 3, pp. 748–752, 2014.

[59] H.-S. Park, D. M. Chambers, H.-K. Chung, R. J. Clarke, R. Eagleton, E. Giraldez, T. Goldsack, R. Heathcote, N. Izumi, M. H. Key, J. A. King, J. A. Koch, O. L. Landen, A. Nikroo, P. K. Patel, D. F. Price, B. A. Remington, H. F. Robey, R. A. Snavely, D. A. Steinman, R. B. Stephens, C. Stoeckl, M. Storm, M. Tabak, W. Theobald, R. P. J. Town, J. E. Wickersham, and B. B. Zhang, "High-energy Kα radiography using high-intensity, short-pulse lasers," *Phys. Plasmas*, vol. 13, no. 5, p. 056309, 2006.

[60] H. J. Lee, P. Neumayer, J. Castor, T. Döppner, R. W. Falcone, C. Fortmann, B. A. Hammel, A. L. Kritcher, O. L. Landen, R. W. Lee, D. D. Meyerhofer, D. H. Munro, R. Redmer, S. P. Regan, S. Weber, and S. H. Glenzer, "X-Ray Thomson-Scattering Measurements of Density and Temperature in Shock-Compressed Beryllium," *Phys. Rev. Lett.*, vol. 102, p. 115001, Mar. 2009.

[61] R. Redmer, H. Reinholz, G. Ropke, R. Thiele, and A. Holl, "Theory of X-ray Thomson Scattering in Dense Plasmas," *IEEE Trans. Plasma Sci.*, vol. 33, no. 1, pp. 77–84, 2005.

[62] M. Urry, G. Gregori, O. Landen, A. Pak, and S. Glenzer, "X-ray probe development for collective scattering measurements in dense plasmas," *J. Quant. Spectrosc. Radiat. Transf.*, vol. 99, pp. 636–648, May 2006.

[63] B. M. Song, S. A. Pikuz, T. A. Shelkovenko, and D. A. Hammer, "Determination of the size and structure of an X-pinch x-ray source from the diffraction pattern produced by microfabricated slits.," *Appl. Opt.*, vol. 44, pp. 2349–58, Apr. 2005.

[64] B. R. Maddox, H. S. Park, B. A. Remington, N. Izumi, S. Chen, C. Chen, G. Kimminau, Z. Ali, M. J. Haugh, and Q. Ma, "High-energy x-ray backlighter spectrum measurements using calibrated image plates.," *Rev. Sci. Instrum.*, vol. 82, p. 023111, Feb. 2011.

[65] W. H. Bragg and W. L. Bragg, "The Reflection of X-rays by Crystals," *Proc. R. Soc. A Math. Phys. Eng. Sci.*, vol. 88, pp. 428–438, July 1913.

[66] S. Pikuz, V. Romanova, and T. Shelkovenko, "Use of higher-order reflection from mica crystals in x-ray spectroscopic investigations at 0.1 - 0.3 nm," *Quantum Electron.*, vol. 25, no. April 1994, pp. 16–18, 1995.

[67] J. Angel and M. Weisskopf, "Use of Highly Reflecting Crystals for Spectroscopy and Polarimetry in X-Ray Astronomy," *Astron. J.*, vol. 75, no. 3, 1969.

[68] C. Kittel, *Introduction to Solid State Physics*. Wiley, 2004.

[69] H. Legall, H. Stiel, A. Antonov, and I. Grigorieva, "A new generation of X-ray optics based on pyrolytic graphite," in *28th Int. Free Electron Laser Conf.*, no. 111, pp. 798–801, 2006.

[70] M. Popovici, A. D. Stoica, B. Chalupa, and P. Mikula, "Interpretation of bent-crystal rocking curves," *J. Appl. Crystallogr.*, vol. 21, pp. 258–265, June 1988.

[71] T. A. Pikuz, A. Y. Faenov, E. Foerster, J. Wolf, O. Wehrhan, J. Heinisch, G. Hoelzer, M. Vollbrecht, S. A. Pikuz, V. M. Romanova, and T. A. Shelkovenko, "Measurements and calculations of flat and spherically bent mica crystals' reflectivity and using them for different applications in the spectral range 1-19 ," in *SPIE X-Ray Extrem. Ultrav. Opt.*, vol. 2515, pp. 468–486, 1995.

[72] C. G. Darwin, "XXXIV. The theory of X-ray reflexion," *Philos. Mag. Ser. 6*, vol. 27, pp. 315–333, Feb. 1914.

[73] C. G. Darwin, "LXXVIII. The theory of X-ray reflexion. Part II," *Philos. Mag. Ser. 6*, vol. 27, pp. 675–690, Apr. 1914.

[74] S. Takagi, "Dynamical theory of diffraction applicable to crystals with any kind of small distortion," *Acta Crystallogr.*, vol. 15, pp. 1311–1312, Dec. 1962.

[75] B. Lai and F. Cerrina, "SHADOW: A synchrotron radiation ray tracing program," *Nucl. Instruments Methods Phys. Res. Sect. A Accel. Spectrometers, Detect. Assoc. Equip.*, vol. 246, pp. 337–341, May 1986.

[76] M. Sanchez del Rio, "Ray tracing simulations for crystal optics," *Proc. SPIE*, vol. 3448, pp. 230–245, 1998.

[77] G. Hölzer, O. Wehrhan, E. Förster, and Q. Iwwv, "Characterization of Flat and Bent Crystals for X-ray Spectroscopy and Imaging," *Cryst. Res. Technol.*, vol. 33, no. 4, pp. 555–567, 1998.

[78] J. Als-Nielsen and D. McMorrow, *Elements of Modern X-ray Physics*. Wiley, 2011.

[79] E. Hecht, *Optics*. Reading, Mass: Addison-Wesley Pub. Co, 1987.

[80] M. Sanchez del Rio, M. Gambaccini, G. Pareschi, and A. Taibi, "Focusing properties of mosaic crystals," *Proc. SPIE*, pp. 1–10, 1998.

[81] A. Pak, G. Gregori, J. Knight, K. Campbell, D. Price, B. Hammel, O. L. Landen, and S. H. Glenzer, "X-ray line measurements with high efficiency Bragg crystals," *Rev. Sci. Instrum.*, vol. 75, no. 10, p. 3747, 2004.

[82] E. J. Gamboa, D. S. Montgomery, I. M. Hall, and R. P. Drake, "Imaging X-ray crystal spectrometer for laser-produced plasmas," *J. Instrum.*, vol. 6, pp. P04004–P04004, Apr. 2011.

[83] N. Chankow, S. Punnachaiya, and S. Wonglee, "Neutron radiography using neutron imaging plate.," *Appl. Radiat. Isot.*, vol. 68, pp. 662–4, Jan. 2010.

[84] H. Kobayashi, M. Satoh, M. Etoh, K. Ogura, and H. Yanagie, "Performance comparison of neutron and X-ray sensitive photo-stimulated imaging plates," *Appl. Radiat. Isot.*, vol. 61, pp. 573–578, Oct. 2004.

[85] A. Mancić, J. Fuchs, P. Antici, S. A. Gaillard, and P. Audebert, "Absolute calibration of photostimulable image plate detectors used as (0.5-20 MeV) high-energy proton detectors.," *Rev. Sci. Instrum.*, vol. 79, p. 073301, July 2008.

[86] N. Izumi, R. Snavely, G. Gregori, J. A. Koch, H.-S. Park, and B. A. Remington, "Application of imaging plates to x-ray imaging and spectroscopy in laser plasma experiments (invited)," *Rev. Sci. Instrum.*, vol. 77, no. 10, p. 10E325, 2006.

[87] G. Fiksel, F. J. Marshall, C. Mileham, and C. Stoeckl, "Note: spatial resolution of Fuji BAS-TR and BAS-SR imaging plates.," *Rev. Sci. Instrum.*, vol. 83, p. 086103, Aug. 2012.

[88] H. Ohuchi-Yoshida and Y. Kondo, "Complete erasing of ghost images on computed radiography plates and role of deeply trapped electrons," *Nucl. Instruments Methods Phys. Res. Sect. A Accel. Spectrometers, Detect. Assoc. Equip.*, vol. 659, pp. 247–251, Dec. 2011.

[89] A. L. Meadowcroft, C. D. Bentley, and E. N. Stott, "Evaluation of the sensitivity and fading characteristics of an image plate system for x-ray diagnostics.," *Rev. Sci. Instrum.*, vol. 79, p. 113102, Nov. 2008.

[90] M. J. Haugh, J. Lee, E. Romano, and M. Schneider, "Calibrating image plate sensitivity in the 700 to 5000 eV spectral energy range," in *SPIE Opt. Eng. + Appl.* (P. M. Bell and G. P. Grim, eds.), International Society for Optics and Photonics, Sept. 2013.

[91] B. L. Henke, J. Y. Uejio, G. F. Stone, C. H. Dittmore, and F. G. Fujiwara, "High-energy x-ray response of photographic films: models and measurement," *J. Opt. Soc. Am. B*, vol. 3, p. 1540, Nov. 1986.

[92] K. M. Chandler, S. A. Pikuz, T. A. Shelkovenko, M. D. Mitchell, D. A. Hammer, and J. P. Knauer, "Cross calibration of new x-ray films against direct exposure film from 1 to 8keV using the X-pinch x-ray source," *Rev. Sci. Instrum.*, vol. 76, no. 11, p. 113111, 2005.

[93] M. D. Abramoff, P. Magalhaes, and S. Ram, "Image Processing with ImageJ," *Biophotonics International*, vol. 11, no. 7, pp. 36–42, 2004.

[94] C. Tuttle, "The Relation between Diffuse and Specular Density," *SMPTE Motion Imaging J.*, vol. 20, pp. 228–235, Mar. 1933.

[95] I. Golovkin, J. J. MacFarlane, P. Woodruff, I. Hall, G. Gregori, J. Bailey, E. Harding, T. Ao, and S. Glenzer, "Simulation of X-ray scattering diagnostics in multi-dimensional plasma," *High Energy Density Phys.*, vol. 9, pp. 510–515, Sept. 2013.

[96] D. Griffiths, *Introduction to Electrodynamics (3rd Edition)*. Benjamin Cummings, 1998.

[97] J. Strutt, "LVIII. On the scattering of light by small particles," *London, Edinburgh, Dublin Philos. Mag. J. Sci.*, vol. 41, no. 275, pp. 447–454, 1871.

[98] J. J. Thomson, "XL. Cathode Rays," *London, Edinburgh, Dublin Philos. Mag. J. Sci.*, vol. 44, no. 269, pp. 293–316, 1897.

[99] A. H. Compton, "The Spectrum of Scattered X-Rays," *Phys. Rev.*, vol. 22, pp. 409–413, Nov. 1923.

[100] D. Froula, J. Ross, L. Divol, and A. MacKinnon, "Thomson scattering techniques in laser produced plasmas," *High Temp.*, 2006.

[101] L. De Broglie, "Waves and quanta," *Nature*, vol. 112, no. 2815, p. 540, 1923.

[102] J. Sheffield, D. Froula, S. H. Glenzer, and N. C. Luhmann Jr, *Plasma scattering of electromagnetic radiation: theory and measurement techniques*. Academic press, 2010.

[103] G. Gregori, S. H. Glenzer, F. J. Rogers, S. M. Pollaine, O. L. Landen, C. Blancard, G. Faussurier, P. Renaudin, S. Kuhlbrodt, and R. Redmer, "Electronic structure measurements of dense plasmas," *Phys. Plasmas*, vol. 11, no. 5, p. 2754, 2004.

[104] J. Chihara, "Interaction of photons with plasmas and liquid metals - photoabsorption and scattering," *J. Phys. Condens. Matter*, vol. 12, pp. 231–247, Jan. 2000.

[105] J. Vorberger, K. Wünsch, and D. Gericke, "Ab initio simulations for X-ray Thomson scattering," Tech. Rep. Annual Report, Centre for Fusion, Space and Astrophysics, Department of Physics, University of Warwick, Coventry, U.K., 2009.

[106] B. A. Mattern and G. T. Seidler, "Theoretical treatments of the bound-free contribution and experimental best practice in X-ray Thomson scattering from warm dense matter," *Phys. Plasmas*, vol. 20, no. 2, p. 022706, 2013.

[107] W. M. Haynes, *Handbook of Chemistry and Physics*. CRC Press, 95 ed., 2014.

[108] B. Crowley, "Continuum lowering A new perspective," *High Energy Density Phys.*, vol. 13, pp. 84–102, Dec. 2014.

[109] J. Stewart and K. Pyatt, "Lowering of ionization potentials in plasmas," *Astrophys. J.*, vol. 144, 1966.

[110] G. Ecker and W. Kroll, "Lowering of the Ionization Energy for a Plasma in Thermodynamic Equilibrium," *Phys. Fluids*, vol. 6, no. 1, p. 62, 1963.

[111] D. S. Sivia, *Elementary Scattering Theory: For X-ray and Neutron Users*. OUP Oxford, 2011.

[112] A. Kramida, Y. Ralchenko, and J. Reader, "NIST Atomic Spectra Database," 2014.

[113] P. R. Wallace, "The Band Theory of Graphite," *Phys. Rev.*, vol. 71, pp. 622–634, May 1947.

[114] I. C. Blesener, *Initiation, Ablation, Precursor Formation, and Instability Analysis of Thin Foil Liner Z-pinches*. PhD thesis, Cornell University, 2012.

[115] S. Ichimaru, *Statistical Plasma Physics*. 2nd ed., 1992.

[116] P.-A. Gourdain, R. Concepcion, M. Evans, J. Greenly, D. Hammer, C. Hoyt, E. Kroupp, B. Kusse, Y. Maron, A. Novick, S. Pikuz, N. Qi, G. Rondeau, E. Rosenberg, P. Schrafel, C. Seyler, and T. Shelkovenko, "Initial magnetic field compression studies using gas-puff Z -pinches and thin liners on COBRA," *Nucl. Fusion*, vol. 53, p. 083006, Aug. 2013.

[117] M. S. Murillo, "Strongly coupled plasma physics and high energy-density matter," *Phys. Plasmas*, vol. 11, no. 5, p. 2964, 2004.

[118] M. Koenig, A. Benuzzi-Mounaix, A. Ravasio, T. Vinci, N. Ozaki, S. Lepape, D. Batani, G. Huser, T. Hall, D. Hicks, A. MacKinnon, P. Patel, H. S. Park, T. Boehly, M. Borghesi, S. Kar, and L. Romagnani, "Progress in the study of warm dense matter," *Plasma Phys. Control. Fusion*, vol. 47, pp. B441–B449, Dec. 2005.